ACTIVE ANTENNA ARRAYS FOR POWER COMBINING AND COMMUNICATIONS

by

MICHAEL ALAN FORMAN

B.S., University of Colorado, 1995

M.S., University of Colorado, 1998

A thesis submitted to the

Faculty of the Graduate School of the

University of Colorado in partial fulfillment

of the requirements for the degree of

Doctor of Philosophy

Department of Electrical and Computer Engineering

2001

This thesis for the Doctor of Philosophy degree by

Michael Alan Forman

has been approved for the

Department of

Electrical and Computer Engineering

by

Zoya Popović

K. C. Gupta

Date _____

Forman, Michael Alan (Ph.D., Electrical Engineering)

Active Antenna Arrays for Power Combining and Communications

Thesis directed by Professor Zoya Popović

Traditional systems with large numbers of solid-state devices suffer from a power-combining network loss, which grows geometrically with the number of amplifiers. A fundamental goal of spatial power combining is the use of free space as a low-loss, power-combining medium to increase the power-combining efficiency of the system.

An active-antenna array is an array of unit cells, each with an amplifying solid-state device and radiating element. Radiation from all unit cells combine coherently in free space with losses that are less than a traditional feed network for a large number of elements.

The regular array of identical unit cells of an active-antenna amplifier lends itself to traditional monolithic uniplanar fabrication. Potential applications for active-antenna arrays include analog front ends for guided munitions, collision-avoidance systems, and communication links.

This thesis presents results on two active-antenna array projects. The first project presents two low-cost *Ka*-band power amplifier arrays fabricated on aluminum nitride. The second presents a *K*-band lensing full-duplex transmit-receive array.

The two *Ka*-band amplifiers of identical RF design are compared. The

focus of the discussion are thermal constraints on the selection of substrates and the effect on antenna design, efficiency, array layout, and bias-line configuration. Results for the *Ka*-band arrays are 89 W EIRP and 316 mW of output power for the first array and 145 W EIRP and 513 mW of output power at 31 GHz for the second.

The *K*-band array is the demonstration of a lensing active-antenna array used for full-duplex transmit-receive operation. This array employs several design enhancements over the previous array, such as increased antenna isolation, simplified fabrication requirements, and a more efficient feed. The focus of the research is on the development of full-duplex transmit-receive operation, the use of design techniques to reduce complexity, and the integration of a lens feed to reduce feed loss. The array transmits and receives at 19 and 21 GHz. Orthogonal antenna polarization and bandpass circuitry provide a simulated isolation of 50 dB at 19 GHz and 42 dB at 21 GHz between transmit and receive channels. The measured gains of the active array are 3 dB and 8.2 dB above passive for transmit and receive modes respectively.

Dedication

everything of price

so doth require my travail

anthem doth commence

allie anna and vicki

bright pomp ascends jubilant

Personal Acknowledgments

I would like to recognize the people, organizations, and circumstances that have contributed to my commencement from humble beginnings. Firstly, I would like to recognize three critical elements whose absence would have precluded my success in college:

- Money. Thanks to the United States Department of Education for providing federal student aid in the form of interest-free loans, grants, and scholarships. Without the government's support the opportunity to attend college would be an unrealized wish.

- Discipline and shelter. Thanks to my father and Michelle for taking me into their home and providing me with the foundation on which I built my scholastic career.

- Tenacity and discontent. I thank chance, which gave to me by means of nature and nurture, my dogged tenacity to stick it out in the most unpleasant of environments and my restless discontentment, which has provided the impetus to continuously improve myself and my station.

I would like to give heart-felt thanks to my girlfriend, Victoria Beckman, for her contributions to my success in graduate school. Vicki, a model of professionalism, has provided me with limitless support in a difficult environment. Her insightful advice helped me transcend personal limitations and in the end take the first steps in transforming myself into a better person. Her selfless investment in my success has earned my life-long respect, friendship, and loyalty.

When I made the difficult decision to remain in Colorado for graduate school it was to be with my family. I thank my father, Craig, my stepmother, Michelle, my brother, Joe, and my two sisters, Allie and Anna, for being positive influences in my life. I could not imagine life without any of them.

I would also like to recognize the exceptional friends and teachers who gave guidance and support at critical moments in my life. I thank them for providing a safe environment in which to learn. I acknowledge the following people:

- Mr. Natale, my first physics teacher, for providing a unique experience which launched my career in the sciences. I thank him for his patience with me as I solved problems from the overhead during lecture reclined in my chair with my arms folded.

- My English teacher, Mrs. Roe, for offering words of kindness in an otherwise empty yearbook. Your support, even after my tragic recitation of Shakespeare, was heroic.

- My friend Heather with whom I took Calculus III. It was she who finally convinced me to stop holding myself back and that I could do anything I set my mind on.

- Ernest Porps, my painting teacher, for taking the frame from his teaching award so that I could enter my sumi ink drawing in the art show. I also thank him for his encouragement while I attempted a Georgia O'Keefe reproduction that redefined chiaroscuro.

- Professor Tim Phillips, my German professor, for his meticulous and very successful method of teaching language. In addition to language, more than anything, he taught me how to be a teacher. It is also important to note that my passion, the study of linguistics and languages (German, French, Japanese, and recently Italian), is a result of his investments.

It is my desire to be to another person what they have been to me.

Professional Acknowledgments

I thank my advisor who allowed me the freedom to pursue my own interests, provided me with the resources necessary to complete my research, and supported me during critical stages in my education. I thank her for allowing me to study German language abroad in Kassel; sending me to present at the 1999 European Microwave Conference in Munich; and allowing me to attend both French and Japanese language classes.

I would like to thank the past and present members of the group for providing technical support in my research and classwork. I give thanks to:

- Scott Bundy, for providing interesting seminars over the years.
- Tom Mader, for showing me how to make a class-A amplifier and including my name on a paper while I was still an undergraduate.
- Jon Schoenberg, for taking time to answer my naïve questions and providing me with tasks, even while he was occupied with his thesis.
- Wayne Shiroma, for teaching me everything I know about grid oscillators. My first project, an 8-GHz voltage-controlled grid oscillator, was

the result of his tutelage.

- Jon Dixon, for teaching me how to calibrate to a free-space through and providing me with an abundance of LaTeX and Unix support.

- Milica Marković, for her flower pot and ceramic dog which I still have.

- Japp Bregmann, for the many discussions on a wide variety of topics.

- Rob Brown, for showing by example how to perform meticulous lab work.

- Stein Hollung, for finishing with an exceptional final project. His successful final endeavor was one of my primary motivations for the scope of my final project.

- Eric Bryerton, who showed me how shed time-consuming lab rituals and get results from projects quickly.

- Slavko Djukić, for showing me that there is happiness on the other side.

- Shawn Stone, for helping me maintain the Unix workstations. Shawn also made significant improvements to the group's `Makefile` and LaTeX code used to create our papers and this thesis.

- Jan Peeters Weem, for invaluable help with Matlab.

- Joe Tustin, for showing courage in the face of adversity. I also really enjoyed the semester that the group spent playing hockey with Joe as

the team captain. It was one of the highlights of graduate school.

- Jim Vian, for technical advice on the design of my lensing array.
- Manoja Weiss, for discussions which contributed to my personal growth.
- Joe Hagerty, for providing discussions on grammar, linguistics, writing, and 3D graphics.
- Darko Popović, for insight on lens design, measurement, and calibration.
- Stephania Romisch, for showing that it is possible to complete a tremendous amount of work in a short amount time and still remain a kind person.
- Branislav Notaroš, for allowing me to port Gem to Unix.
- Paul Smith, for bringing China to me.
- Jason Breitbarth, for knowing more entering the program than most of us who are exiting, and not rubbing it in.
- Srdjan Pajić, for his kind nature and commitment to making the lab a better place to work.
- Rachael Tearle, for facilitating communications between me and my advisor.

- Helen Frey, for providing a plethora of invaluable services, most of which revolved around my favorite elements of graduate school: computer components, reimbursements, and travel.

I would like to give special recognition to Todd Marshall, with whom I worked for several years on the *Ka*-band active-antenna array. Todd's background in physics and meticulous attention to detail contributed greatly not only to the project but also to my personal development. Todd also possesses a strong moral compass and work ethic for which I have great respect.

Thanks to Richard Waters, Ivan Perez, Professor Van Zeghbroeck, and Professor May for their help in the development of the photolithographic process used to fabricate the arrays.

I would also like to recognize the contributions of Sean Ortiz, Amir Mortazawi, John Hubert, Lee Mirth, and John Whitaker for their contributions to the *Ka*-band amplifier project: Sean Ortiz and Amir Mortazawi provided the hard-horn antennas used for near-field measurements; John Hubert and Lee Mirth of Lockheed Martin Orlando provided us with an invaluable behind-the-scenes look at industrial-quality research; and John Whitaker characterized the near-fields of the arrays with the electro-optic probe station.

Contents

Tables

Figures

Chapter 1

Introduction and Background

1.1 Solid-State Power Combining

Traditional millimeter-wave amplification is performed by tube-based amplifiers such as the klystron and traveling-wave tube (TWT). Capable of high gain and output powers, these amplifiers are widely used in radar and communications applications. However, millimeter-wave watt-level tube-based amplifiers are expensive, heavy, subject to catastrophic failure, and suffer from long lead times. For example, commercially available watt-level *Ka*-band TWT amplifiers may cost as much as $3,000 per watt and have lead times of many months (Table 1.1).

Solid-state devices have emerged as an alternative to tube-based amplifiers at microwave and millimeter-wave frequencies due to their reduced size and cost. Initially seen in millimeter-wave power modules (MMPM) as driver

Table 1.1: Comparison of TWT amplifier costs.

Manufacturer	Model	Frequency	P_{out}	Cost	Delivery
Litton	M 761-04	15-17 GHz	50 W	$32,500	7 months
Litton	M 762-00	18-40 GHz	10-20 W	$50,000	9 months
Litton	M 762-01	34-36 GHz	20 W	$70,000	9 months
Litton	M 773-00	43.5-44.5 GHz	40 W	$85,000	unknown

stages to conventional TWTs, solid-state power combiners are increasingly seen as a viable replacement for both tube-based amplifiers and MMPMs.

1.1.1 Corporate Power Combining

Individual millimeter-wave solid-state devices produce watt-level power. To obtain output powers on the order of a MMPM or TWT, many solid-state devices must be combined in parallel by means of a power combining network. A comparison between output power between tube-based and solid-state amplifiers is shown in Figure 1.1. Solid-state devices exhibit an initial $1/f$ frequency dependence due to efficiency limitations followed by a $1/f^2$ dependence imposed by impedance matching considerations [2].

The combining structure shown in Figure 1.2 is comprised of individual amplifiers in a guiding medium joined by two-way adders. This method of power combining is known as corporate power combining and is capable of reaching moderate power levels at microwave and millimeter-wave frequencies. In the case of a parallel corporate power combiner, the total number of devices is $N = 2^K$, where K is the number of stages. The total com-

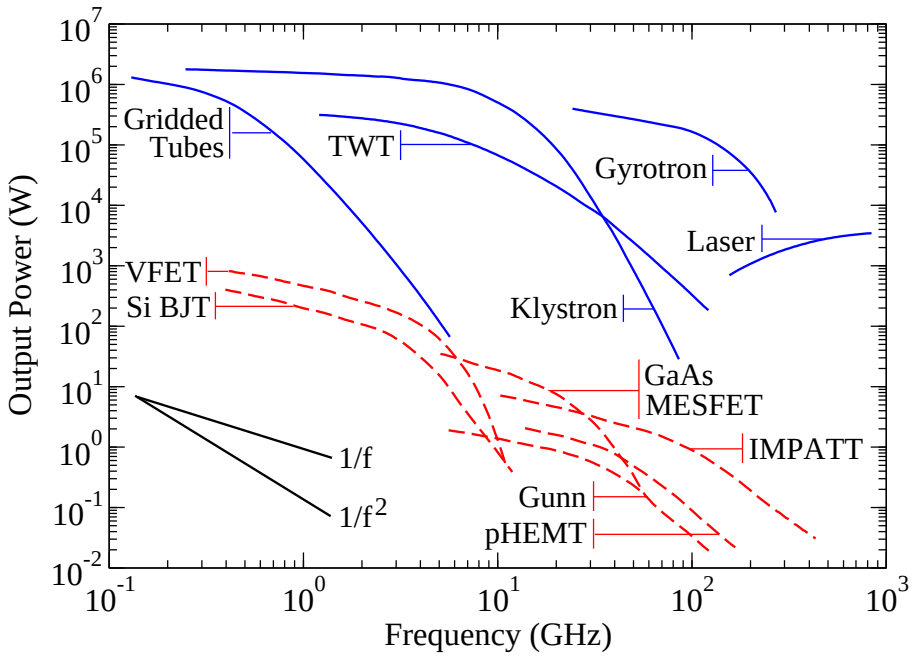

Figure 1.1: Output power as a function of frequency for various amplifiers and sources [1].

bined output power is $P_{out} = 2^K P_0 L^K$, where P_0 is the output power of a single device and L is the insertion loss of each stage. The ratio of the total output power to the sum of the individual output powers, or the combining efficiency, of such a network is

$$\eta_c = \frac{P_{out}}{KP_0} = \frac{2^K P_0 L^K}{2^K P_0} = L^K = L^{\log_2(N+1)} \tag{1.1}$$

The geometric drop in power-combining efficiency with each new stage places an upper limit on the output power. Because insertion loss of guid-

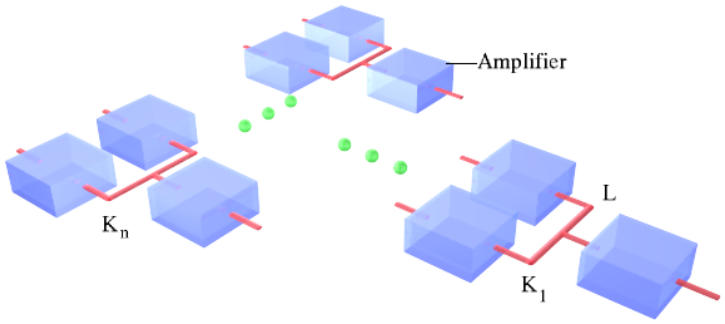

Figure 1.2: Parallel corporate power-combining network.

ing structures grows approximately with the $\sqrt{f}$ [3], the problem is further complicated at higher frequencies. Figure 1.4 shows the results of a path loss analysis of a corporate combining network, using Wilkinson combiners for monolithic microwave integrated circuit (MMIC) amplifiers at 10 GHz, 32 GHz, and 94 GHz [4]. The low power-combining efficiency, which limits the maximum output power of a corporate combiner, is the primary motivation for the development of spatial power combiners.

1.1.2 Spatial Power Combining

Spatial power combining provides enhanced combining efficiency by coherently adding the device outputs to beams or modes in free space rather than through transmission lines in corporate combining structures. In principle, because the combining medium is low loss (air), the power-combining efficiency is high. This eliminates the size limitation and frequency dependence

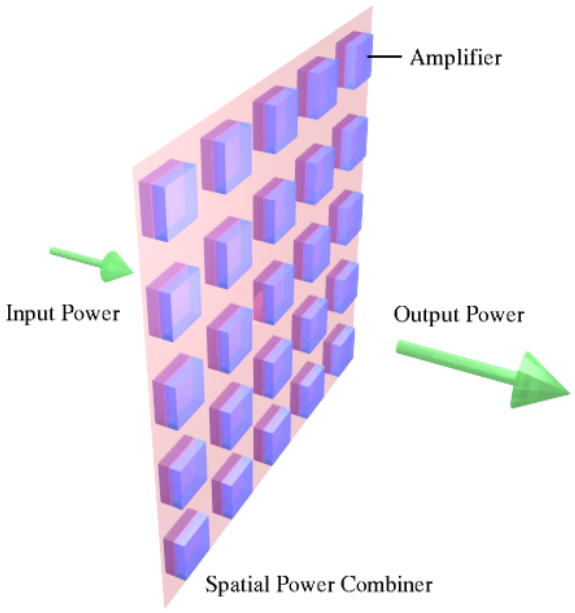

Figure 1.3: A tile-based spatial power combiner.

of corporate power combiners and allows for the possibility of truly high-power, solid-state amplifiers with the ability to compete with tube-based amplifiers.

A spatial power combiner is shown in Figure 1.3. Experimental results place the combining efficiency of spatial power combiners between 70% and 90% shown as straight lines in Figure 1.4. From the figure, it can be seen that for a small number of amplifier elements, corporate power combiners have higher power-combining efficiency, but as the number of amplifiers increase, spatial power combiners provide relatively higher efficiency. The figure also illustrates the effect of frequency on the stage loss for the corporate power

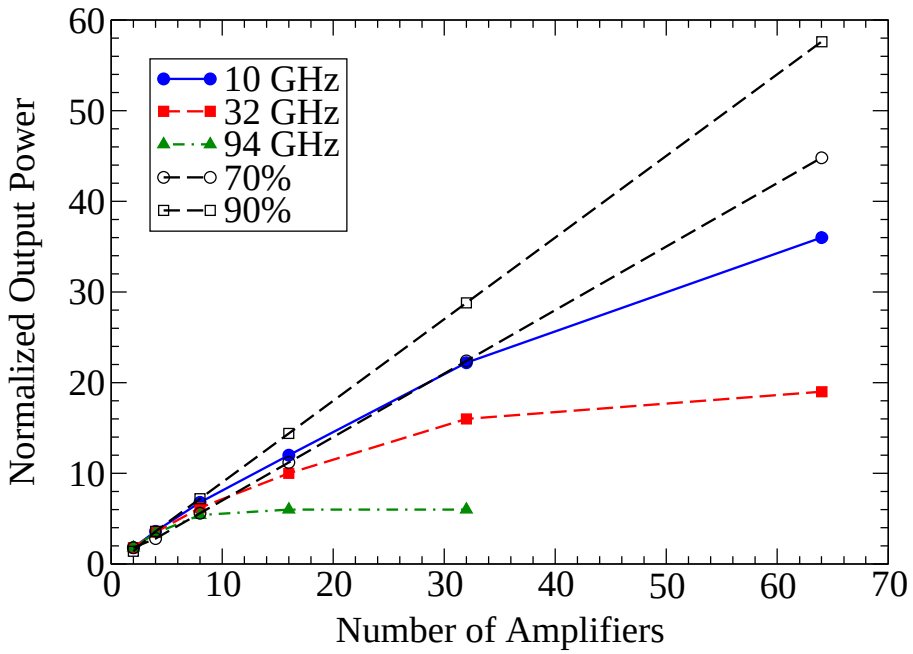

Figure 1.4: Feed efficiency versus the number of stages and stage insertion loss for quasi-optical and Wilkinson power combining networks.

combiner. As frequency increases, due to higher losses in the guiding medium, corporate power combining drops in efficiency.

It would be incorrect to separate corporate and spatial power combining architectures. In fact, there exist hybrid power combiners which employ corporate combining on the input and spatial combining at the output. For example, the Jet Propulsion Laboratory 32-GHz Tray Approach Array produces 1.6 W at 32 GHz [5] and the Motorola 35-GHz Mono-pulse Radar

Array produces 25 W at 35 GHz with 70% PCE [6]. A tray-based spatially-fed/spatially-combined combiner which employs a corporate power combiner in each tray, has been fabricated by Lockheed Martin in a 60GHz Phased Array [7]; by Sanders in a combiner which produces 35 W at 61 GHz [8]; and by Delisle *et al.* in a circuit-spatially combined array at 45 GHz [9].

An early demonstration of the potential for antenna-based spatial power combiners was conducted by Staiman *et al.* [10], who constructed a 100-element amplifier array at 410 MHz in 1968. In that work 1-W 7-dB-gain bipolar transistors provided amplification between a pair of electrically short monopole antennas. The array delivered 100 W of power with a gain of 4.75 dB.

1.2 Spatial Power-Combining Architectures

Active-antenna arrays for spatial power combining systems have been demonstrated in two topologies, known as *tile* and *tray*. The tile approach places the circuitry into unit cells which are fed parallel to the array surface normal (Figure 1.5(a)). In the tray approach active devices are placed between end-fire antennas and are fed perpendicular to the substrate normal (Figure 1.5(b)).

Tile-based spatial power combiners come in two different types: *grid array* or *active-antenna array*. The grid array, introduced by Rutledge *et al.*, is an active frequency-selective surface (FSS) [11] loaded with active devices

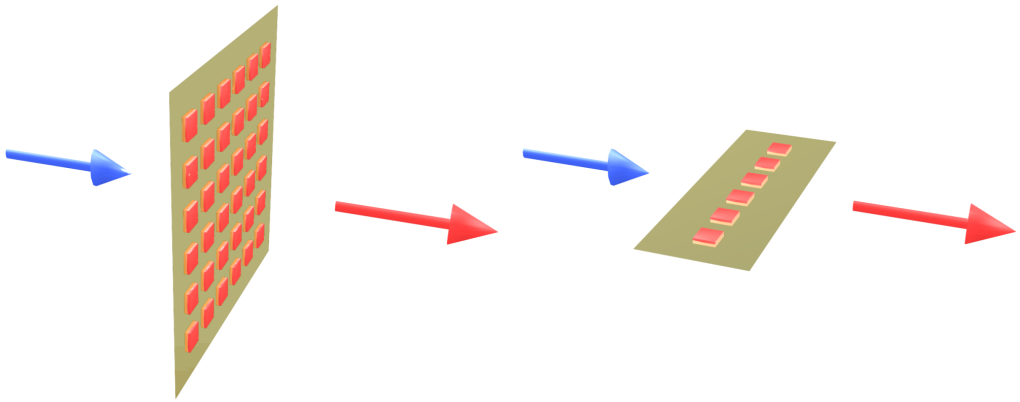

(a) (b)

Figure 1.5: Tile (a) and tray (b) topologies.

[12]. The period of the unit cell is small in comparison to a wavelength. Alternatively, the active-array approach is an extension of classical antenna array systems, which employs independent unit cells with conventional planar antennas integrated with active circuitry. Unit-cell size is on the order of a half-wavelength.

The tray approach places active devices between two end-fire antennas such as linearly-tapered slots or vivaldi antennas. The trays are stacked to provided a two-dimensional array which also has the benefit of providing high isolation between active devices. An individual tray employs back-side metalization for thermal management.

Although the field of spatial power combining is too young for the determination of a superior topology, some generalizations can be made. The tray-based grid architecture has the greatest sensitivity to the design and

fabrication of the FSS and active devices, but provides the highest power density and lends itself easily to monolithic fabrication. The active-antenna and tray-based arrays can accommodate the larger commercial MMIC chips, taking advantage of their inherent higher isolation and stability. Because the length of a tray-based array does not affect the size of the unit cell, a tray can accommodate arbitrarily large circuitry.

1.3 Spatial Power-Combining Feeds

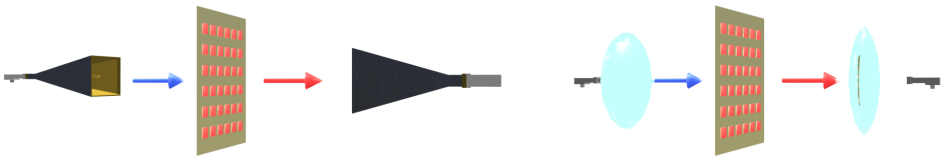

(a) (b)

Figure 1.6: An array in a free-space (a) and a gaussian-beam (b) feed.

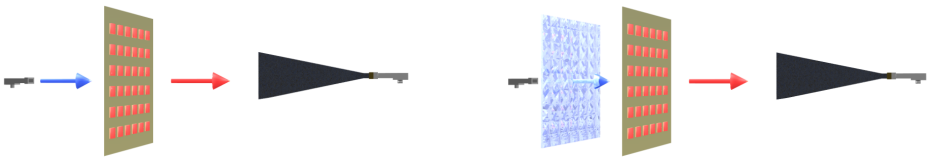

(a) (b)

Figure 1.7: Lens (a) and holographic (b) feeds.

Spatial power combiners utilize feeds which attempt to confine the input

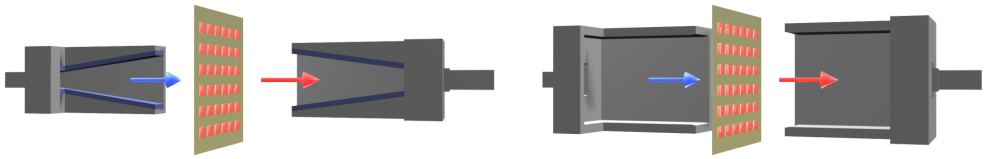

(a) (b)

Figure 1.8: Dielectric-loaded horns (hard horns) (a) and over-moded waveguide (b) feeds (shown in cross-section).

and output power by means of guiding structures or optics. The exception is the far-field free-space feed, in which a horn in the far field illuminates the array with a plane wave of uniform magnitude and phase (Figure 1.6(a)). While useful for array characterization because of its simplicity, free-space and spill-over losses make it impractical for use as a feed for a spatial power combiner. Feed systems which utilize optics to guide the input and output beams include gaussian feeds (Figure 1.6(b)), which use focusing dielectric lenses; holographic feeds made from milled dielectrics (Figure 1.7(b)); and integrated planar lens feeds (Figure 1.7(a)) which by means of delay lines permit a near-field feed. Waveguide-based feeds include dielectric loaded horns (hard horns) (Figure 1.8(a)); and over-moded waveguide feeds (Figure 1.8(b)). All feeds attempt to provide an incident field with uniform magnitude and phase at the face of the array to increase the power combining efficiency.

Planar lens feeds lend themselves to applications which require direct radiation into free space. Gaussian-beam and waveguide-fed amplifier ar-

rays could provide direct compatibility with TWT vacuum tubes, as well as cascading easily with other optical or waveguide components.

1.4 Functionality of Active Arrays

Renewed interest in spatial power combining has been recently motivated by the improvements in output power of solid-state devices at higher frequencies. The first solid-state spatial power combiner is the active grid array [12]. Since the first demonstration, several grid amplifiers followed with more elements and higher output power [13]. Active-antenna arrays kept pace, yielding several successful designs such as a nine-HEMT spatial amplifier [14] and a 37-GHz monolithic array [15]. As the work progressed, the applications of spatial power combiners diversified to include high power [16, 17], high efficiency [18, 19], low noise [20], high gain [21], and broad bandwidth [22, 23]. In these research efforts, the common motivation for spatial power combining is to obtain watt-level power from solid-state amplifiers at millimeter-wave frequencies while maintaining high power combining efficiency.

Because of their similarity to traditional active arrays, active-antenna arrays have grown in functionality for specific applications. Various additional functionalities include beam-switching arrays [24], transceivers [25], diplexing arrays [26], quasi-optical isolators [27], local-area network and communications transmitters [28, 29], as well as transmit-receive front-ends for communications [30, 31, 32, 33].

1.5 Organization of the Thesis

This thesis presents the design, fabrication, and measurement of two different active-antenna amplifier implementations. The first topography is a spatially-fed/spatially-combined (plane-wave/plane-wave) active-antenna array (tile-based) amplifier, the second is a spatially-fed/spatially-combined (lens-fed/plane-wave) full-duplex transmit/receive active-antenna amplifier array (tile-based).

The motivation for using spatial power combining in place of corporate power combiners, as well as early work in the field, has been presented in Chapter 1.

Chapter 2 describes motivation, previous work, and figures of merit for the *Ka*-band active-antenna amplifier array. Design constraints and methods are shown in Chapter 3 with measurement of the *Ka*-band amplifier given in Chapter 4.

Early work on lens active-antenna amplifier arrays as well as an overview of constrained lens theory is presented in Chapter 5. In Chapter 6, the design and fabrication of the *K*-band full-duplex transmit-receive active-antenna amplifier array is presented. Experimental results are presented in Chapter 7.

Finally, Chapter 8 provides a summary of the projects and provides suggestions for future work on full-duplex transmit-receive active-antenna array front-ends.

Chapter 2

Ka-Band Active-Antenna Array Background

2.1 Motivation

The primary goal of the following *Ka*-band active-antenna amplifier array work is to take advantage of the high combining efficiency [1] and graceful degradation [34] of active-antenna arrays, in order to obtain watt-level power at *Ka*-band using low-cost commercial MMICs. A *Ka*-band tile-based active-antenna amplifier array has been constructed in collaboration with Lockheed Martin in Orlando to study the feasibility of light-weight watt-level spatial power combiners for munition guidance systems.

Military and commercial interest in *Ka*-band frequencies is motivated by low atmospheric propagation loss in the frequency range surrounding 30 GHz

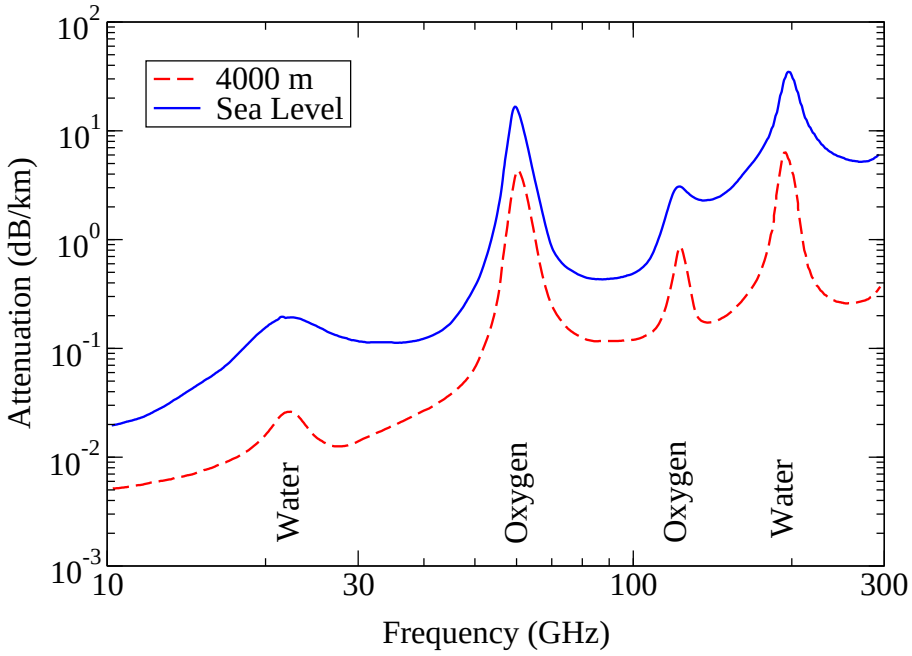

Figure 2.1: Microwave signal attenuation in air as a function of frequency.

(Figure 2.1). The lower loss is beneficial for communication and radar applications which require free-space transmission. Moreover, antennas designed at *Ka*-band are of reduced size and mass relative to antennas designed at lower frequencies with comparable gain.

Several researchers have demonstrated *Ka*-band quasi-optical amplifier arrays: in [35], MMIC amplifiers were combined using patch antennas to provide 4 W of output power and 16 dB of large-signal gain, and in recent work increased the results to 25 W [36]; in [37] and [38], monolithic grid

amplifiers, using HBTs and pHEMTs respectively, showed gain up to 60 GHz; in [39], 1 W of power was obtained in an array mounted in a waveguide. These systems are extremely expensive employing one-of-a-kind experimental solid-state devices fabricated and assembled by a large company. In contrast, the arrays presented in the following work utilize off-the-shelf commercial MMICs to demonstrate low-cost watt-level power.

In addition to expanding the number of *Ka*-band spatial power combiners, this work seeks to drive fundamental research in new directions by studying the repeatability of array performance; thermal properties of the substrate; effect of device biasing; and sensitivity to fabrication tolerances. The studies are performed on two experimental *Ka*-band arrays, referred to as Array A and Array B, of nearly identical RF architectures. The arrays differ only in the implementation of the biasing network and substrate-metal thickness.

2.2 Figures of Merit

This work adheres to the published figures of merit for the quantitative analysis of spatial power combiners [40]. As a primer for the design and characterization of the arrays in the following chapters, the concepts of aperture efficiency, effective radiated power, array gain, and power combining efficiency are discussed.

2.2.1 Aperture Efficiency and System Gain

Aperture efficiency is the ratio of the effective area of a spatial power combiner to the physical area [41].

$$\eta_a = \frac{A_{\text{eff}}}{A_{\text{phys}}} \tag{2.1}$$

For spatial power combiners, specifically tile-based, it is paramount to maximize the absorption of available incident power on the face of the array by maximizing the aperture efficiency. The effective area of a spatial power combiner is proportional to the directive gain

$$A_{\text{eff}} = \frac{\lambda^2}{4\pi} G \tag{2.2}$$

which is related to directivity by

$$G = \eta_r D \tag{2.3}$$

where η_r is the system efficiency which includes substrate losses, ohmic losses, and polarization and impedance mismatches. The maximum bore-sight directivity of a tile-based spatial power combiner can be calculated by dividing the solid angle of a unit sphere ($4\pi\,\text{sr}$) by the product of the normalized antenna and array factor over space

$$D = \frac{4\pi}{\oiint_S |F(\theta,\phi)|^2 |A(\theta,\phi)|^2 d\Omega} \tag{2.4}$$

where $F(\theta,\phi)$ and $A(\theta,\phi)$ are the normalized element and array factor respectively.

For an array with N elements of arbitrary magnitude, phase, and placement, the array factor is given by [42]

$$A(\theta, \phi) = \sum_{n=1}^{N} I_n e^{j(kd_n \sin\theta \sin\phi + \beta_n)} \tag{2.5}$$

The directivity of a spatial power combiner is most strongly influenced by the array factor, as planar antennas typically have low gain. However, antennas may strongly influence aperture efficiency. For instance, omnidirectional radiators will halve aperture efficiency. If omnidirectional radiators are used in an active-antenna arrays, one solution is the use of a reflector or polarizer to enforce the unidirectional radiation of the array.

As an illustration of the concepts developed above, the aperture of an array of Hertzian dipoles as a function of antenna (or unit-cell) spacing is calculated [1]. The element pattern for a dipole in free space is given as

$$F(\theta, \phi) = \sqrt{1 - \sin^2\theta \sin^2\phi} \tag{2.6}$$

and the element pattern for a dipole a distance h above an infinite ground plane is given by

$$F(\theta, \phi) = \sin(k_0 h \cos\theta)\sqrt{1 - \sin^2\theta \sin^2\phi} \tag{2.7}$$

The aperture efficiency is calculated and shown in Figure 2.2 with the aperture efficiencies for uniformly excited aperture of the same physical size as the array. An ideal uniformly-excited aperture will achieve 100% aperture efficiency only if it is constrained to radiate into half-space. Because of

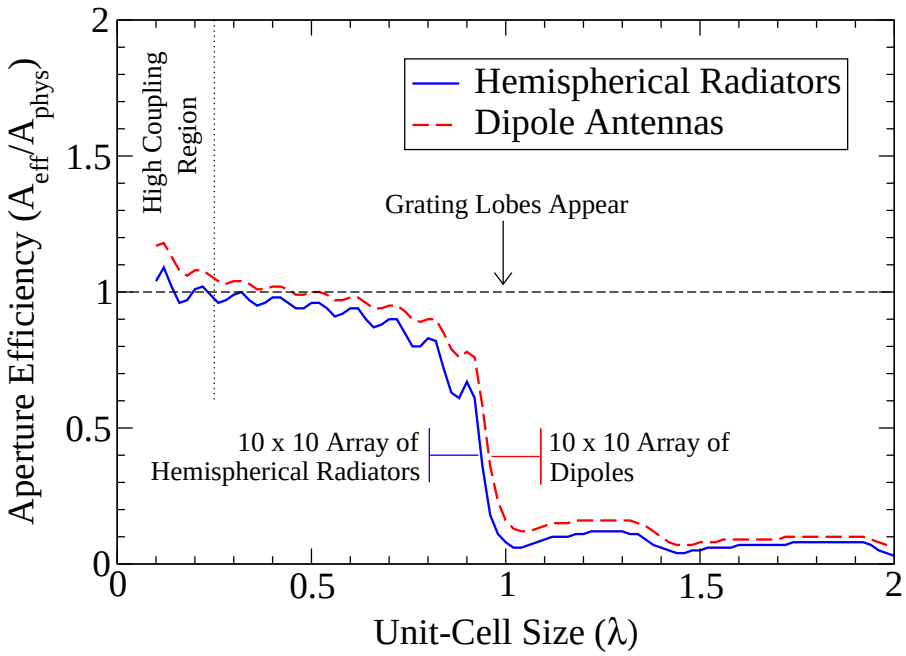

Figure 2.2: Aperture efficiency as a function of unit-cell spacing for a 10×10 array of hemispherical radiators and a 10×10 array of dipoles above a ground plane. Accuracy of the simulations drops for unit cells less than 0.25λ square due to high inter-element coupling.

realistic antenna size and inter-element coupling, aperture efficiencies for spacings below 0.1λ are omitted. Depending on antenna type and array geometry, values for spacings less than 0.25λ may be inaccurate.

Several conclusions can be drawn from the analysis of the graph. Aperture efficiency is relatively constant between 0.3λ and 0.9λ. Aperture efficiency drops for element spacings above 1.0λ, which coincides with the onset of

grating lobes. This imposes a 1.0λ limit on the spacing of unit cells, and requires the addition of reflective surfaces or polarizers for antennas in tile-type spatial power combiners which radiate both above and below the array surface. Note that the aperture efficiency is higher for an array of dipole antennas than an array of hemispherical radiators. The improvement in the aperture efficiency is due to the effect of the antenna pattern on the overall array pattern. The antenna pattern reduces the size of the side lobes and grating lobes at angles away from boresight thus increasing array gain and aperture efficiency.

2.2.2 Effective Isotropic Radiated Power

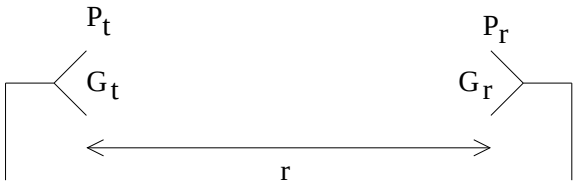

Figure 2.3: Diagram of a standard two-horn link used as a reference for understanding the Friis transmission formula.

The Friis transmission formula is used extensively throughout this work as a means to calculate radiated powers, antenna gains, and calibration normalizations. In its basic form, it relates power received to power transmitted as a function of path loss and antenna gains [41].

$$P_r = P_t G_t G_r \left(\frac{\lambda}{4\pi r}\right)^2 \tag{2.8}$$

where G_t and G_r are the gains of the transmitting and receiving antennas and $(\lambda/4\pi r)^2$ is the free-space path loss over a distance r due to spherical wave propagation as seen in Figure 2.3.

The Friis transmission formula allows the experimental determination of two important figures of merit: output power and equivalent isotropic radiated power (EIRP). The EIRP is the product of the transmitted output power, P_t, and the transmitting antenna gain, G_t, (Equation 2.9). It is a useful measure in the calculation of link budgets if only for convenience – a single number can characterize a transmitter. The EIRP may be a preferable measure over output power (Equation 2.10) in cases where the transmitting gain, G_t, is difficult to determine as in the case of grid oscillators [43].

$$\text{EIRP} = P_t G_t = \frac{P_r}{G_r} \left(\frac{4\pi r}{\lambda} \right)^2 \tag{2.9}$$

$$P_t = \frac{P_r}{G_r G_t} \left(\frac{4\pi r}{\lambda} \right)^2 \tag{2.10}$$

2.2.3 System Calibration

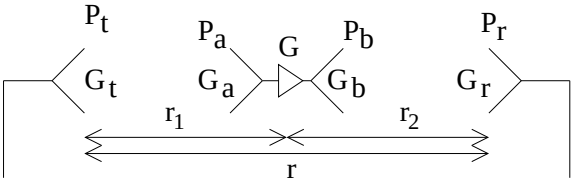

Figure 2.4: Two-horn link with repeater used in the discussion of repeater bias.

Measurement calibration for small-signal gain measurements is performed by measuring the through response of two horns in the far field and normalizing subsequent measurements to that value. By applying the Friis transmission formula in Equation 2.8 to the calibration setup in Figure 2.3. It is apparent that the addition of a repeater (device under test) in the setup (Figure 2.4) fundamentally changes the transfer of power through the system. Solving the combination of linear equations describing the new system yields a modified equation for the new link budget. The first part of the link is represented as

$$P_{a1} = P_t G_t G_{a1} \left(\frac{\lambda}{4\pi r_1} \right)^2 \tag{2.11}$$

and the second part as

$$P_{r1} = P_{b1} G_{b1} G_r \left(\frac{\lambda}{4\pi r_2} \right)^2 \tag{2.12}$$

where the gain of the repeater is represented by

$$P_{b1} = G_1 P_{a1} \tag{2.13}$$

where G_1 is the horn-to-horn gain (or loss) of the repeater, The relationship between the lengths is given by

$$r = r_1 + r_2 \tag{2.14}$$

This yields the desired equation

$$P_{r1} = P_t G_t G_r G_{a1} G_{b1} G_1 \left(\frac{\lambda}{4\pi} \right)^4 \left(\frac{1}{r_1 r_2} \right)^2 \tag{2.15}$$

The ratio of the received power with a device under test, P_{r1}, to the received power without a device under test, P_{r0}, is given by

$$\frac{P_{r1}}{P_{r0}} = G_{a1} G_{b1} G_1 \left(\frac{\lambda}{4\pi}\right)^2 \left(\frac{r_1 + r_2}{r_1 r_2}\right)^2 \tag{2.16}$$

The insertion of a lossless repeater into a link can lead to a decrease in transfered power. This effect is most pronounced in measurements where the device under test has low directivity. This drop in transmitted power upon insertion of a lossless repeater ($G_1 = 1$) is referred to as *repeater bias*. The effects on the *Ka*-band array measurements are minimal and mentioned briefly in Chapter 4.1.2 on page 64.

2.2.4 Repeater Bias in Power Amplifiers

An important figure of merit for a power amplifier is insertion loss. This is typically measured by placing the device under test into a closed system such as an over-moded waveguide or in a gaussian-beam feed. The gain of the array is measured with respect to a through calibration taken with the array absent. The system gain of the array is a ratio of the power received with the array present divided by the power received with the array absent as a function of frequency,

$$\frac{P_{r2}}{P_{r0}} = G_2 \tag{2.17}$$

The system gain solves exactly for the array gain.

When characterizing arrays in an *open system*, such as an active-antenna array with a free-space feed, the measurement is more complicated. As devel-

oped in Chapter 2.2.3 on page 20, the device under test is a repeater within a link. The system gain is given by

$$\aleph = \frac{P_{r1}}{P_{r0}} = G_{a1} G_{b1} G_1 \left(\frac{\lambda}{4\pi}\right)^2 \left(\frac{r_1 + r_2}{r_1 r_2}\right)^2 \tag{2.18}$$

System gain measurements made with a free-space feed are a function of the array gains, the wavelength, and the spacing of the radiators. Depending on the system configuration, it's possible to have system gains which vary between the two measurement systems significantly.

For example, consider a free-space measurement system with an active-antenna array (presented in Chapter 4.1.2 on page 64) as the device under test with the following parameters:

$$f_0 = 31\,\mathrm{GHz} \tag{2.19}$$

$$\lambda = 9.677\,\mathrm{mm} \tag{2.20}$$

$$A_{phys} = (7\,\mathrm{cm})^2 = 0.005\,\mathrm{m}^2 \tag{2.21}$$

$$G_{a1} = G_{b1} = 24.5\,\mathrm{dB} \tag{2.22}$$

$$r_1 = 101\,\mathrm{cm} \tag{2.23}$$

$$r_2 = 64\,\mathrm{cm} \tag{2.24}$$

A measurement performed in a confined system on an lossless passive array will return a system gain equivalent to the aperture efficiency of the

array.

$$\eta_a = \frac{A_{\text{eff}}}{A_{\text{phys}}} \tag{2.25}$$

$$= \frac{G}{4\pi}\frac{\lambda^2}{A_{\text{phys}}} \tag{2.26}$$

$$= 0.42 \tag{2.27}$$

$$= -3.7\,\text{dB} \tag{2.28}$$

A measurement performed for the same passive array in a system with free-space feeds placed in the far field of the array, will return the loss due to the aperture efficiency plus the additional repeater bias of

$$\aleph = \frac{P_{r1}}{P_{r0}} = G_{a1}G_{b1}G_1\left(\frac{\lambda}{4\pi}\right)^2\left(\frac{r_1+r_2}{r_1 r_2}\right)^2 \tag{2.29}$$

$$= 0.308 \tag{2.30}$$

$$= -5.1\,\text{dB} \tag{2.31}$$

The expected difference between the two measured system gains is 5.1 dB. In fact, experimental verification of this very measurement has been performed in a free-space system by myself and a gaussian-beam system by Todd Marshall in collaboration with Blythe Deckman at Caltech. The measured difference in gain between the two systems is 5 dB in favor of the gaussian-beam system [44] as predicted.

Unfortunately the plots for a gaussian-feed system and free-space-feed system are often shown side by side with no renormalization of the plot. A more accurate comparison between systems would be to correct the measurement by the repeater bias.

2.2.5 Power Combining Efficiency

Power combining efficiency, originally introduced in Chapter 1.1.1 on page 2, is the ratio of the total integrated far-field output power to the sum of the transmitted amplifier powers.

$$\eta_c = \frac{\oiint_S P_d dS}{\sum_{n=1}^{N} P_n} \approx \frac{P_t}{NP_0} \tag{2.32}$$

In practice the received power, P_t, as calculated from the Friis transmission formula, is used as an approximation of the total radiated power. Typical spatial power combiners achieve power combining efficiencies in the range of 70% to 90%.

Chapter 3

Ka-Band Active-Antenna Array Design and Fabrication

3.1 Design

A schematic of the *Ka*-band spatial power combiner is shown if Figure 3.1. A compendium of hierarchies and elements is presented to provide insight into the design and function of the system. It must be noted, that although the following information is presented in a logical flow across hierarchies, the design is, in fact, an iterative process involving some or all of the levels at different stages in the design. The following chapter discusses the selection and design of the following elements: device and substrate selection, intra-unit-cell element design, unit-cell layout, array configuration, and external system design.

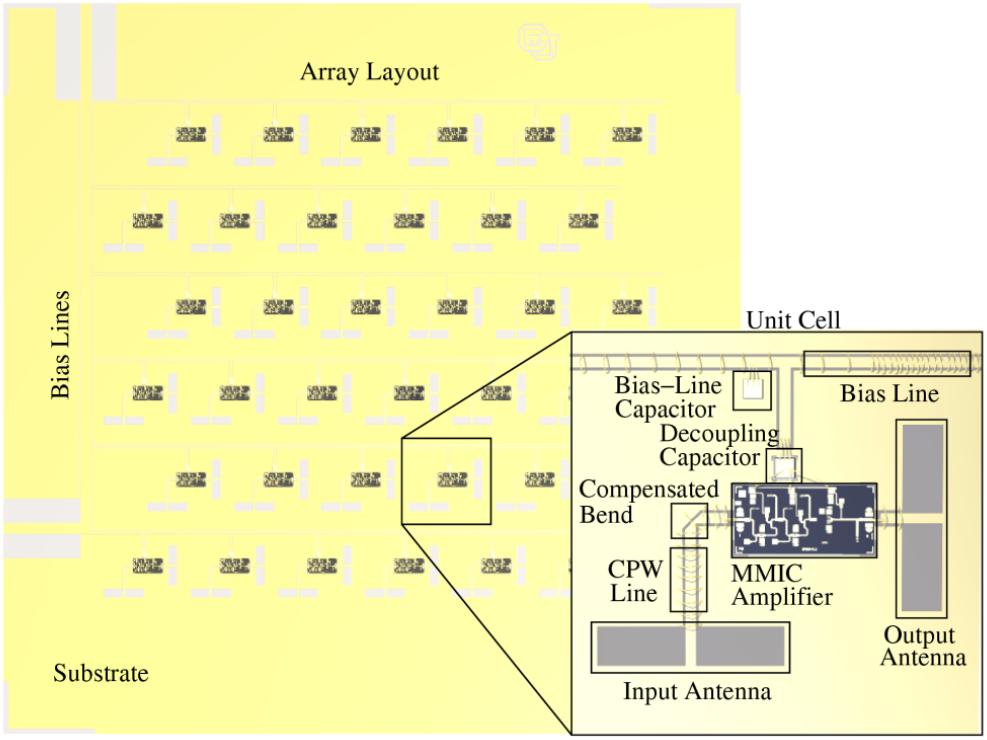

Figure 3.1: Design hierarchy of the *Ka*-band spatial power combiner.

3.1.1 Active and Passive Components

Although the active device is more appropriately classified as an intra-unit-cell element, its role as a thermal source necessitates its discussion before that of the substrate. Because the array will be used in a closed system without the ability to lose heat through radiation or convection, the heat must be conducted through the thin substrate from center to edge.

An *Alpha* AA028P3-00 MMIC driver amplifier was chosen for the active-antenna array. The selection of the device was a compromise between size,

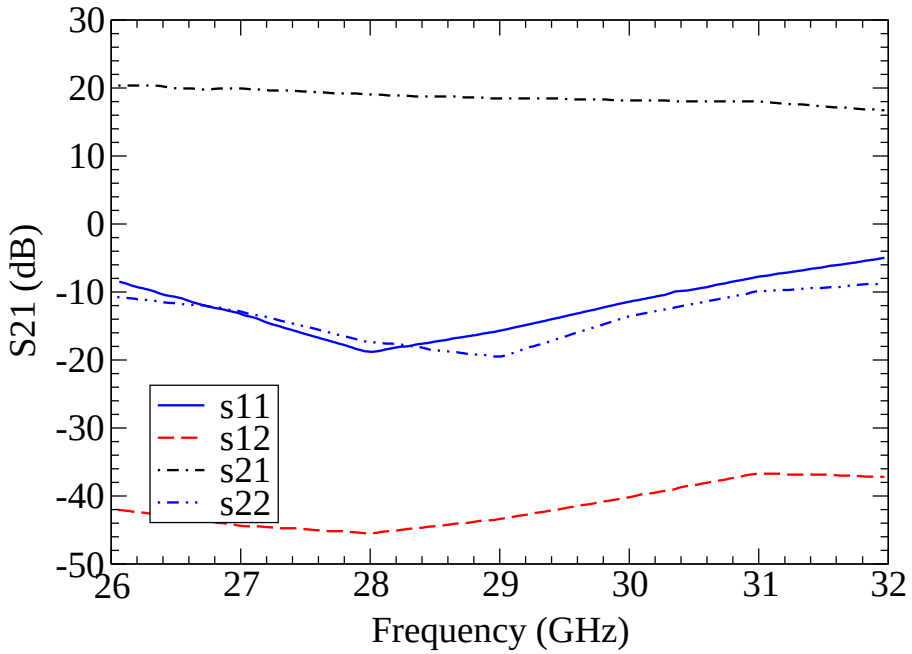

Figure 3.2: S-parameters of the Alpha AA028P3-00 MMIC.

voltage characteristics, and cost per watt. The active device, fabricated with 0.25 μm Ti/Pt/Au gates on 100 μm gallium arsenide (GaAs). The reported s-parameters are shown in Figure 3.2. A single device provides 19 dB of small-signal gain at the design frequency of 31 GHz. At the 1-dB compression point, the three-stage amplifier generates 15 dBm (31 mW) at 6 V with a current draw of 150 mA (3.5% efficient). This creates 900 mW of thermal power for a single device or 33 W of thermal power for a 36-element active-antenna array at maximum current draw.

Decoupling chip capacitors are placed between the bias and the MMIC. The capacitors are *ATC* Microcap chip capacitors measuring 457 μm square with an approximate height of 250 μm (depending on the value of capacitance). The capacitance values of 47 and 100 pF are used as recommended by the documentation.

3.1.2 Substrate

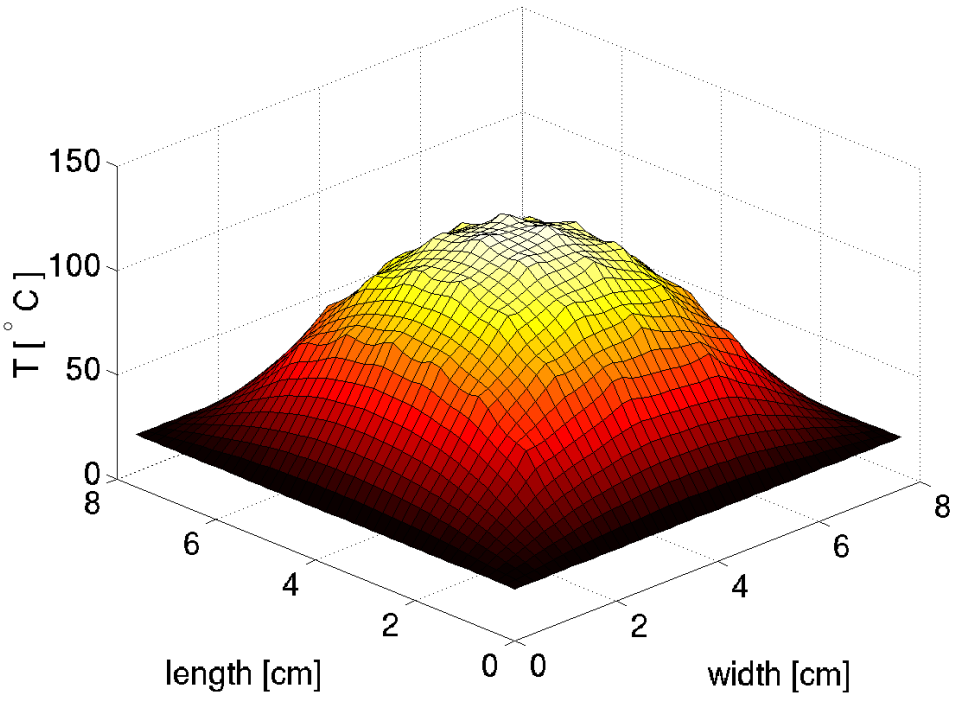

Figure 3.3: Theoretical surface temperature of the AlN substrate with edge cooling and 36 1-W thermal sources [44].

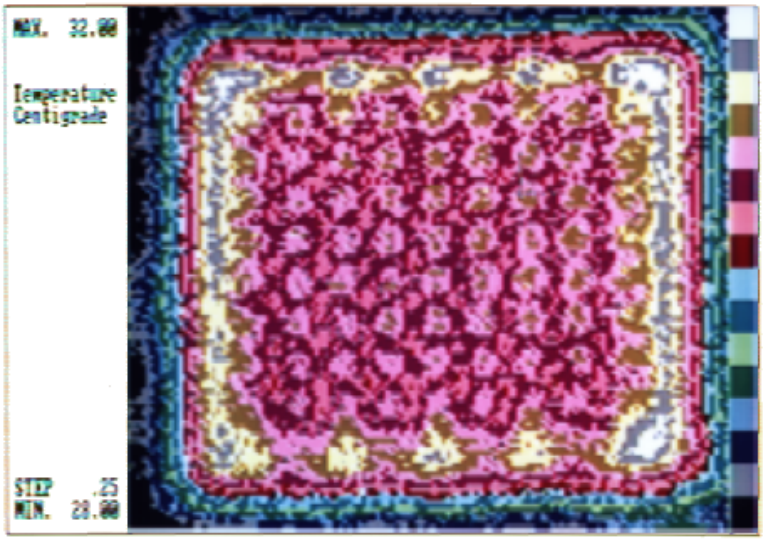

Figure 3.4: Measured surface temperature of the diamond substrate with water edge cooling [45].

The choice of substrates is constrained by the recommended 125°C maximum operating temperature of the MMIC. Thermal gradients across a substrate due to active devices are approximated with an analytical model of heat conduction [44]. The model assumes a uniform heat flux under each MMIC and a uniform temperature of 25°C along the edge of the substrate.

Various substrate types and dimensions have been simulated with the analytical model in an effort to find a compromise between maximum steady-state temperature, cost, and availability. Substrate sizes are selected to be 7.62 cm by 7.62 cm by h, where h varies between 254 μm to 406 μm, depending on availability of the substrate. In the model the array has 36 unit cells spaced 9 mm apart, each with a thermal source in the center representing a MMIC

Table 3.1: Theoretical maximum substrate temperature assuming center-to-edge conduction only [44].

Substrate	h (μm)	k (W/mK)	P_h (W)	ΔT (°C)
Diamond	406	2000.0	33	5
AlN	254	170.0	33	99
TMM 6	381	0.7	33	14975

amplifier operating at maximum power. Producing 33 W of thermal power, the 36 heat sources bring the substrates to a steady-state temperature which is a function of thickness and thermal conductivity. The maximum expected temperatures based on the conduction model for diamond, aluminum nitride (AlN), and *Rogers* TMM 6 substrates are presented in Table 3.1 and shown for AlN in steady-state in Figure 3.3. The small peaks in the temperature distribution are the MMIC thermal sources. The accuracy of the model was verified by thermographs taken of a diamond substrate by the Lockheed Martin Electronics and Missiles Group in Orlando Florida in Figure 3.4 [45]. The edges of the diamond substrate are held at a constant 28°C by circulating water. The steady-state center temperature was 32°C, giving a edge-to-center gradient of 4°C.

Results show that the diamond substrate has the lowest maximum steady-state temperature, followed by AlN with a T_{max} close to 125°. The maximum temperature calculated for the TMM 6 substrate is a non-physical solution as the model omits energy flux in the form of convection and radiation. Taking these other forms of heat escape into consideration decreases the maximum

steady-state temperature, making these numbers useful as an absolute albeit unrealistic maximum. Although Lockheed Martin pursued an active-antenna array on a diamond substrate, the cost and availability place it out of reach for most practical applications. Likewise, the relatively low thermal conductivity of the TMM substrate excludes it from use as a substrate for a power amplifier which relies on center-to-edge conductive cooling.

Because the maximum thermal gradient of the AlN substrate is 100°C, and AlN is readily available and relatively inexpensive, it is the best candidate for an active-array substrate. The AlN substrate is 7.62 cm by 7.62 cm by 254 μm thick with a relative permittivity of 8.6 and a thermal conductivity of 170 W/mK.

3.1.3 Element Design

Transmission Lines

The transmission lines are traditional coplanar waveguide (CPW). Coplanar waveguide enables uniplanar fabrication eliminating the need for vias to ground for active devices. Coplanar waveguide also provides a natural, balanced feed to broad-band slot antennas – a design requirement. The maximum dimension of the CPW, $2s_{\text{cpw}} + w_{\text{cpw}}$, is limited on the upper end by the relative antenna and MMIC dimensions, and on the lower end by the minimum feature size of the fabrication technology. The dimensions of a CPW are found by solving a transcendental equation based on an analytical

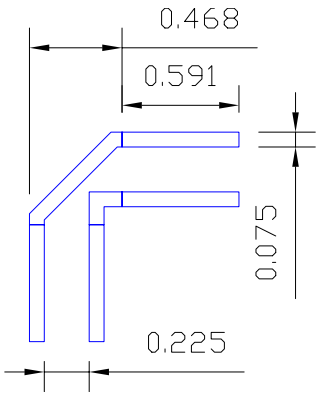

Figure 3.5: Diagram of the CPW 90-degree compensated bend. The area outside the lines is metal. Units are in millimeters.

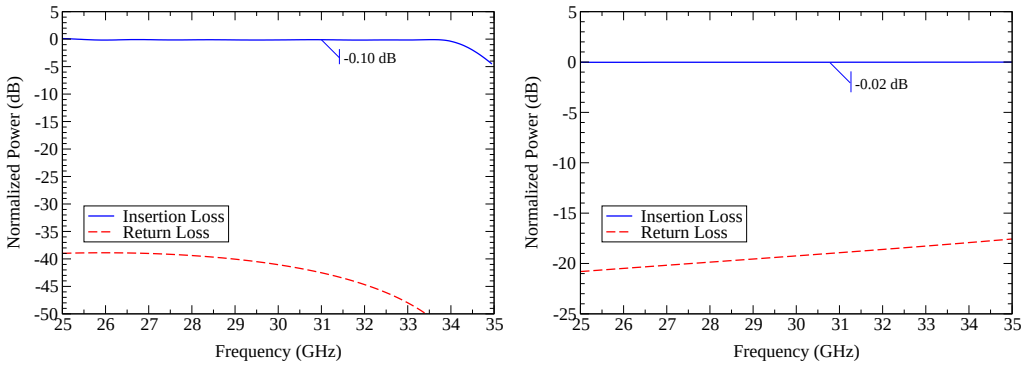

(a) (b)

Figure 3.6: Simulation showing the reflection and transmission coefficient of the CPW line (a) and 90-degree compensated bend (b).

model [46]. After some iteration between the various components of the unit cell, the dimensions of the 50Ω CPW converged upon $w_{cpw} = 225\,\text{um}$ and $s_{cpw} = 75\,\text{um}$.

A 90-degree bend is required to feed two identical antennas of orthogonal

polarization (Figure 3.5). In order to lower reflection and loss introduced by a standard bend, a 90-degree compensated bend is utilized [47]. The simulated bend provides lower reflection and loss relative to a standard 90-degree bend with a return and insertion loss below -17 dB and -0.2 dB over the range of interest (Figure 3.6).

Antennas

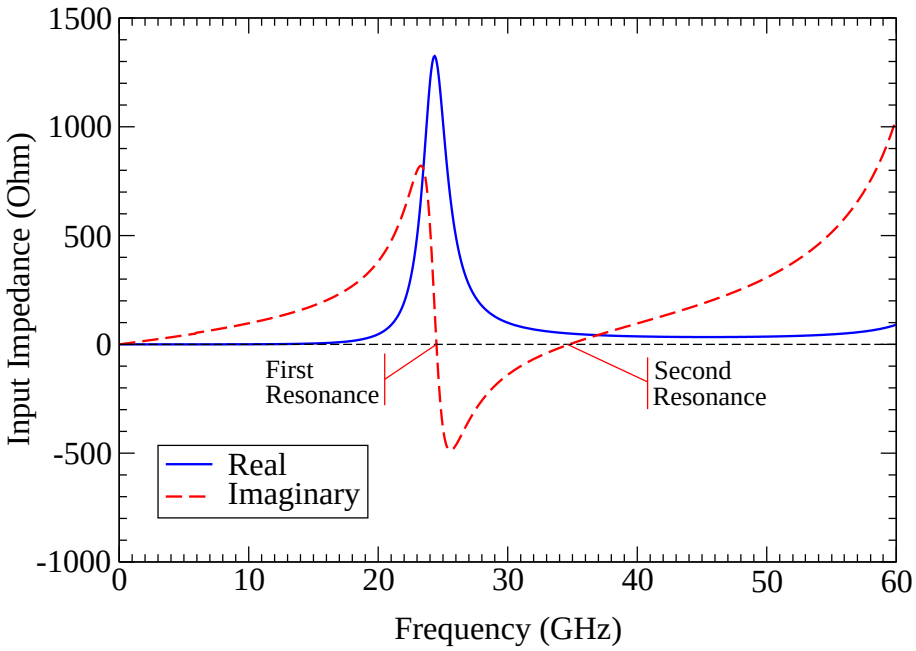

Figure 3.7: Slot antenna real and imaginary input impedance as a function of frequency. Resonances exist at the imaginary zero-crossings. Bandwidth is inversely proportional to the slope at the zero crossing.

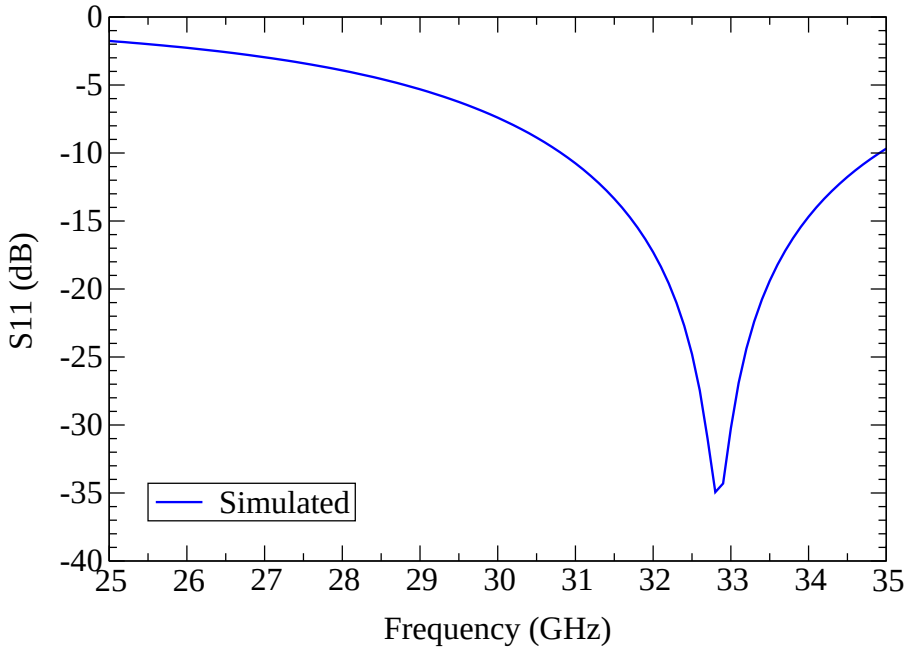

Figure 3.8: Simulated frequency response of a slot antenna on AlN.

A second-resonance slot antenna is chosen as the radiator, in order to maximize the system bandwidth while maintaining uniplanar fabrication. The larger bandwidth of a second-resonance slot antenna can be illustrated by plotting the real and imaginary input impedance of a slot as a function of frequency. As seen in Figure 3.7, the shallow slope of the second zero crossing of the imaginary input impedance is indicative of a broad-band radiator. The impedance is calculated with *WireZeus*, a method-of-moments (MOM) code that uses entire-domain basis functions to numerically calculate the antenna

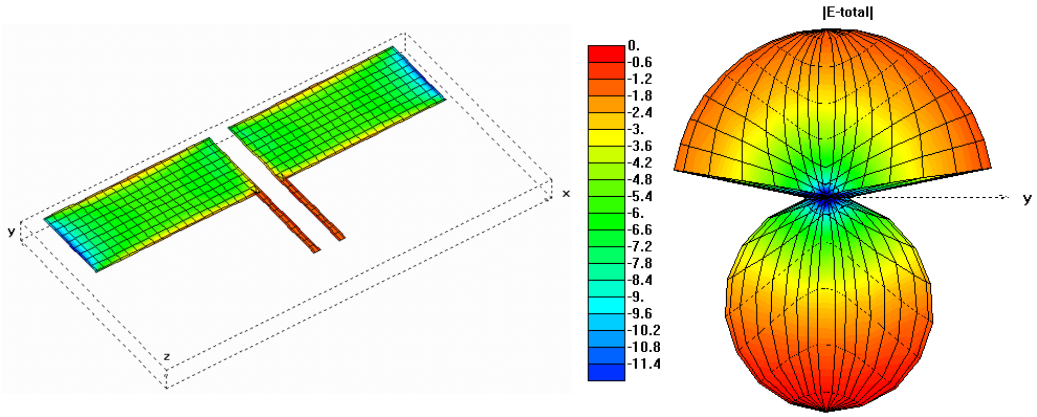

(a) (b)

Figure 3.9: Simulated magnetic current density (a) and far-field pattern (b) of a CPW-fed second-resonance slot antenna fabricated on AlN.

currents [48].

Additional simulations with *Momentum* [49] and *IE3D* [50] have verified the broad-band performance (Figure 3.8), as well as solved for the currents (Figure 3.9(a)) and the far-field radiation pattern (Figure 3.9(b)). The designed antenna is 4.15 mm by 0.9 mm, has a resonance of -18.4 dB at 32.7 GHz with a 12.5% 2:1-VSWR bandwidth. The simulated radiation efficiency of a slot antenna is 70% (-1.52 dB), attributed to substrate losses and radiation into substrate modes.

Note that the radiation pattern in Figure 3.9(b) indicates radiation on both sides of the substrate plane (although the preference by 2.5 dB is in the direction through the substrate). To improve power combining efficiency, polarizers are required in the system to enforce unidirectional radiation.

3.1.4 Bias Lines

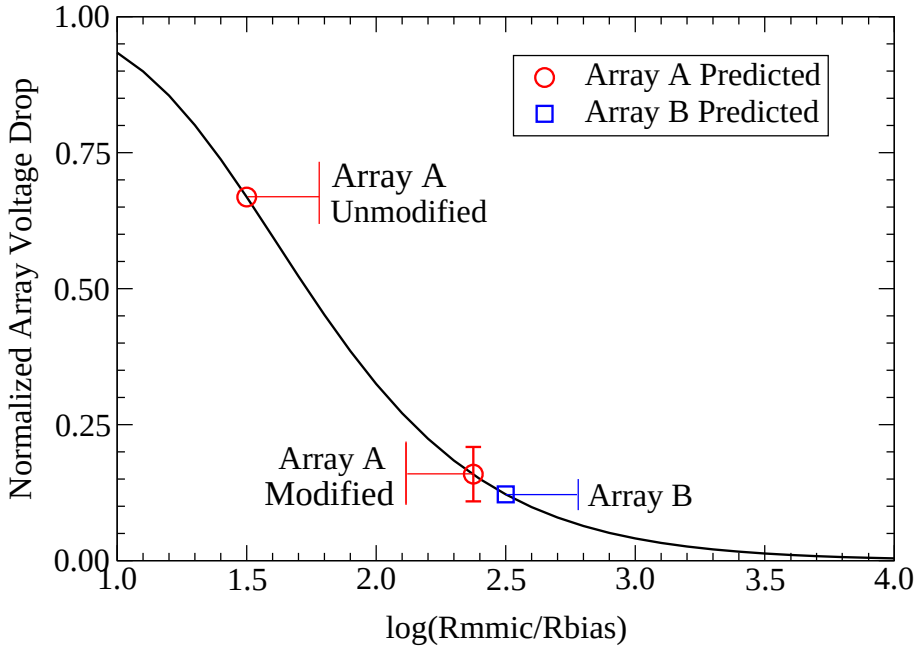

Figure 3.10: Theoretical maximum voltage drop across the array as a function of the ratio of bias-line resistance to MMIC resistance.

For simplicity, bias lines are chosen to be of the same dimension as the CPW and are oriented perpendicular to the output antennas to reduce coupling from the output antenna. The extent of the preliminary design includes the calculation of the resistivity of a line the length of a unit cell to determine its contribution to the generation of heat. With the resistivity of the line on the order of a fraction of an ohm, the contribution is negligible.

During the course of preliminary measurements it was found that there exists a voltage variation across the face of the array as a result of parallel voltage dividers between the unit-cell bias lines and the MMICs. Although this analysis took place in the middle of the project, it is presented below in the design section for continuity.

The schematic in Figure 3.14 on page 43 shows the bias line configuration, in which a single vertical bias line feeds multiple horizontal lines in parallel, which in turn feed a row of MMICs in parallel. This parallel-parallel DC distribution network leads to minute but accumulating voltage drops across the arrays.

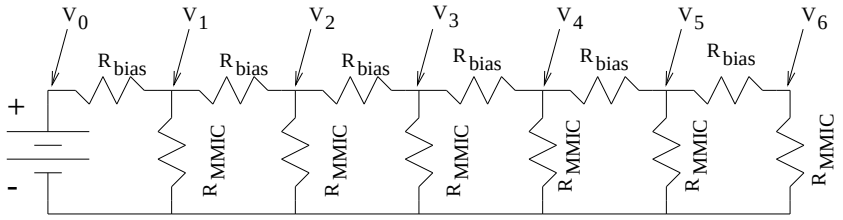

Figure 3.11: Voltage-divider network which models the bias lines of the arrays.

For an array which distributes bias along a line to devices in parallel, a voltage variation will occur even for relatively low values of line resistance. It is possible to model the biasing network as a resistive ladder network consisting of series, R_{bias}, and shunt, R_{MMIC}, resistors (Figure 3.11). The variables, R_{bias} and R_{MMIC}, represent the resistance of the unit-cell bias line and the resistance of the internal MMIC biasing circuitry, respectively. The

bias voltage along a row at the $(k+1)$ unit cell is given by:

$$V_{k+1} = \frac{R_{N-k-1}}{R_{\text{bias}} + R_{N-k-1}} V_k \quad \text{, where} \tag{3.1}$$

$$R_j = \left[\frac{1}{R_{\text{MMIC}}} + \frac{1}{R_{\text{bias}} + R_{j-1}} \right]^{-1}. \tag{3.2}$$

For the *Ka*-band active-antenna array, the number of unit cells in a row is $N = 6$, $j = 1$ to $N - 1$, and $k = 0$ to $N - 1$. The supply voltage, V_0, is at $k = 0$ and $R_0 \equiv R_{\text{MMIC}}$. Equations 3.1 and 3.2, expressed as a function of the ratio $R_{\text{MMIC}}/R_{\text{bias}}$, reveal that the bias voltage variation over an array may be substantial. As can be seen from the graph in Figure 3.10, the device impedance must be at least a 1000 times greater than that of the bias line to prevent a voltage drop across the array.

As stated previously in Chapter 2.1 on page 13, the arrays are of identical RF architectures differing only in the implementation of the biasing network and substrate metalization thickness. Provided by different vendors, the substrate for Array A is clad in $4\,\mu$m of gold, whereas the substrate for Array B is covered in $4.3\,\mu$m of copper cladded in an additional $2\,\mu$m of gold. This difference in metal thickness and conductivity has a direct effect on the resistance of the bias lines, and hence the voltage drop across the arrays due to the parallel-parallel bias network. The points in Figure 3.10 labeled *Array A Unmodified* and *Array B Unmodified* represent the normalized bias drops expected from each array as a result of the bias-line resistance.

An attempt to reduce the voltage drop on Array A has been made by the addition of a supplemental bias line over the original line. The supplemental

bias line is comprised of conductive copper tape on insulating adhesive mylar and connected by silver epoxy to a vertical bus bar (Figure 3.23 on page 54). Due to resistive connections from the vertical bus bar to the horizontal supplemental bias lines, measured voltage variations from row to row still exist (Figure 4.17 on page 73) which is represented by the error bar on the *Array A Modified* point in Figure 3.10 on page 37. This variation in bias uniformity is the underlying cause for the variation in RF performance between the two arrays.

3.1.5 Element Coupling

After converging on designs for the elements of the unit cell, the level of mutual coupling is determined through simulation and measurement before placement into a unit cell. Based on the results in Chapter 1.1.2 on page 4, which derived the dependence of aperture efficiency on unit-cell size, an attempt is made to minimize this dimension. The goal is to perform coupling simulations among intra-unit-cell elements to judge how closely elements can be placed while avoiding affecting their performance.

HP Momentum simulations are performed to study coupling between slot antennas and bias lines to determine the minimum size of the unit cell. Coupling is shown as a function of distance normalized to a wavelength on the elements shown in Figure 3.12. The results of the simulation are shown in Figure 3.13. The circles correspond to the separation distances used in the final array design. A $0.9\lambda_0$ unit cell is selected as a trade-off between coupling

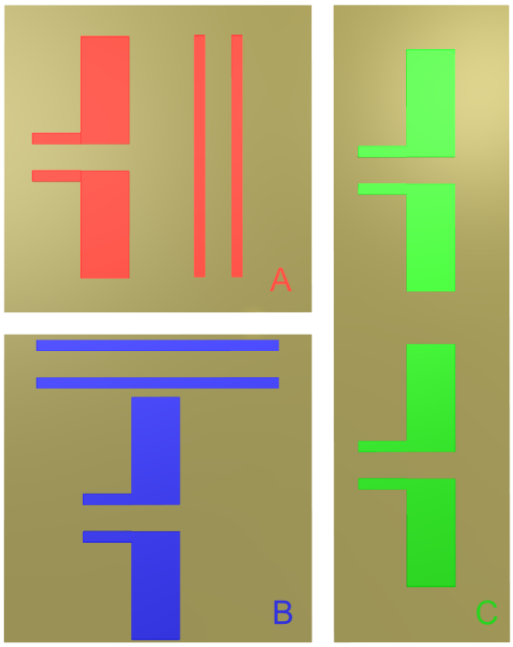

Figure 3.12: Three layouts used to simulate coupling among antennas and lines within a unit cell. The center objects represent slot antennas, transmission lines, and bias lines etched into a plane of surrounding metal. Layout A corresponds to parallel antenna-to-line coupling, layout B measures perpendicular antenna-to-line coupling, and layout C corresponds to antenna-to-antenna coupling.

and aperture efficiency.

3.1.6 Unit-Cell

The unit-cell size is selected to be 0.9λ square, as a compromise between aperture efficiency and the risk of oscillations due to coupling. The unit cell is shown in Figure 3.14. The input slot antenna receives power from an incident vertically-polarized plane wave. The received power is coupled onto

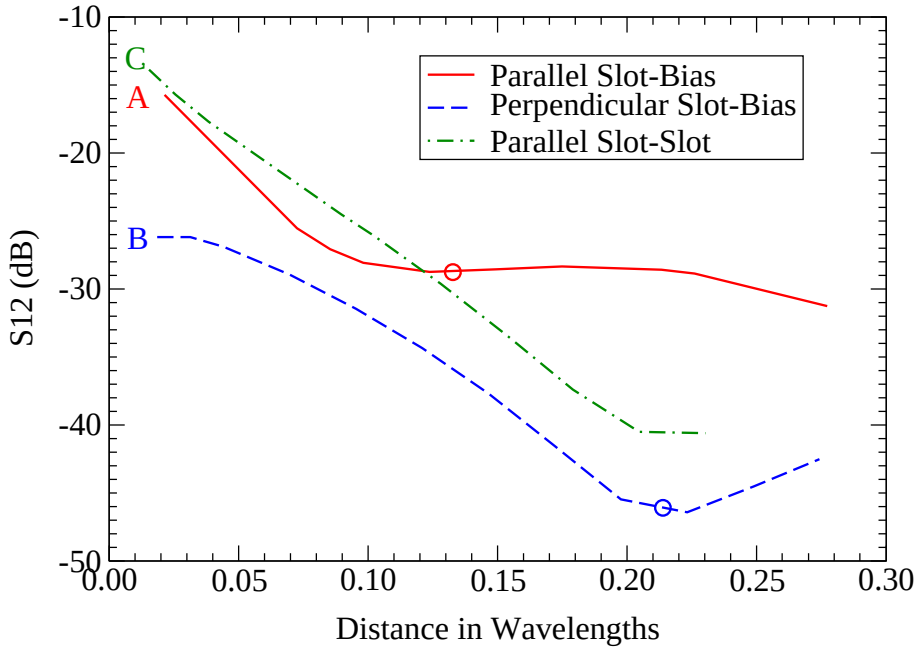

Figure 3.13: Simulated coupling between slot antennas and CPW lines as a function of distance for various orientations.

the 50-Ω CPW transmission line and is amplified by a commercial MMIC. The amplified power is re-radiated in the orthogonal polarization by the output slot antenna. Unit-cell isolation and stability is provided by orthogonal polarization of the input and output antennas.

Aperture efficiency as a function of unit-cell size for a 6×6 triangular array of slot antennas radiating unidirectionally is shown in Figure 3.15. For the chosen unit-cell size of 0.9λ the simulated aperture efficiency excluding

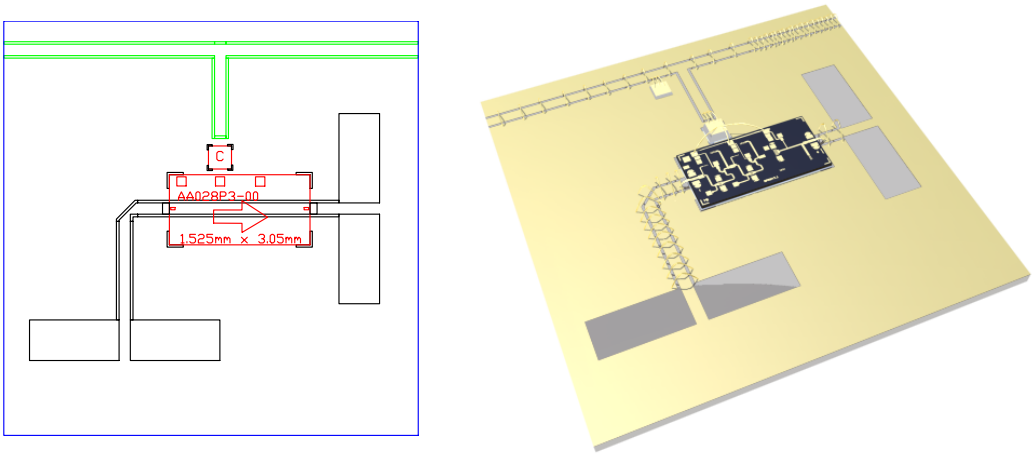

(a) (b)

Figure 3.14: Dimensions of the unit cell are chosen as a trade off between unit-cell size and coupling level. The schematic (a) shows the t-shaped bias line on top, the capacitor and MMIC in the center, and the two slot antennas connected by CPW. A rendered version of the schematic (b) clearly shows the slot and metal regions. The unit cell is 0.9λ square (9 mm).

polarization loss is 0.73.

3.1.7 Array Layout

The array is laid out in a fashion which utilizes the interaction between the array factor and the antenna pattern to minimize sidelobes. A 6×6 array of 0.9λ-unit-cell hemispherical radiators shown in Figure 3.16(a) produces the far-field pattern shown in Figure 3.16(b). Shifting the unit cells by half a unit cell (0.45λ), a common method of reducing sidelobes in arrays, the array in Figure 3.17(a) generates the far-field pattern in Figure 3.17(b). Note that the

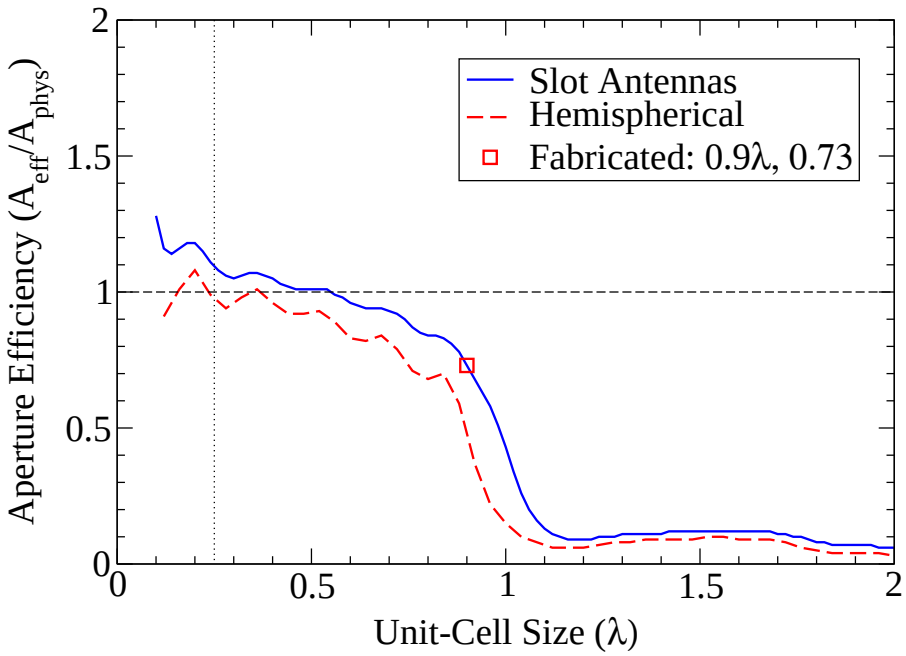

Figure 3.15: Aperture efficiency versus unit-cell size for a 6×6 triangular array of slot antennas radiating hemispherically.

x-plane sidelobe level has been reduced by the triangular lattice. The final step involves the multiplication of the triangular lattice in Figure 3.17 with the output slot pattern (shown radiating hemispherically) in Figure 3.18. The output slot is placed into the triangular lattice such that the null in the slot antenna's pattern coincides with the remaining side lobes in the triangular lattice.

The final array layout and pattern is presented in Figure 3.19. The differ-

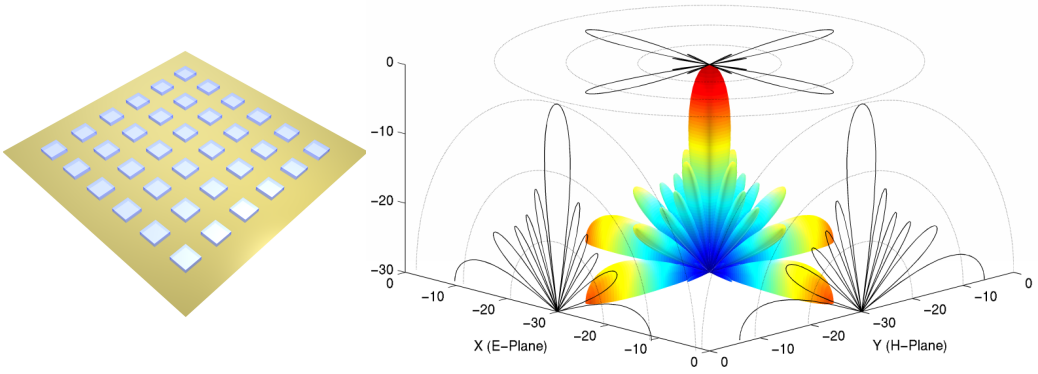

(a) (b)

Figure 3.16: Hemispherical radiators in a square lattice (a) and their resulting simulated far-field array factor (b).

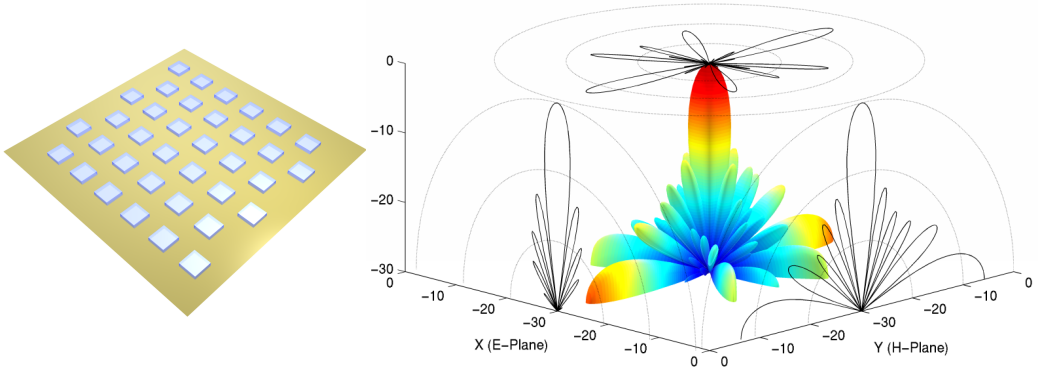

(a) (b)

Figure 3.17: Hemispherical radiators in a triangular lattice (a) and their resulting simulated far-field array factor (b).

ence between a square lattice and a triangular lattice with correctly oriented slot antennas is a drop in side-lobe level from -7 dB to -14 dB, a 7 dB im-

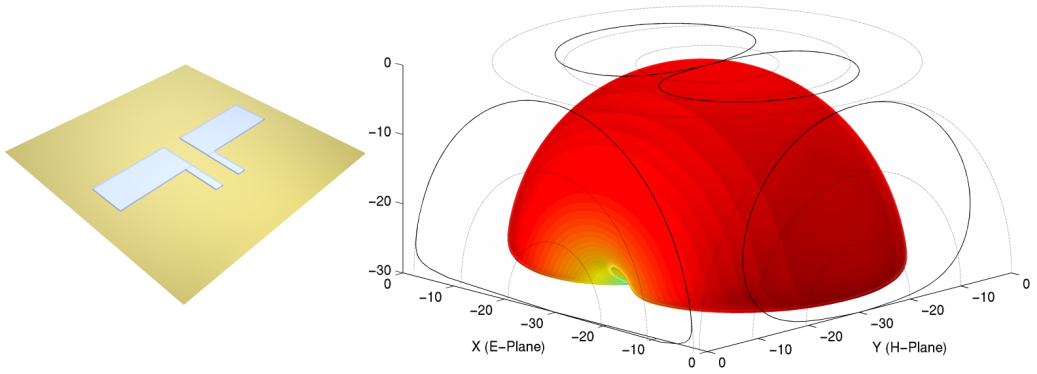

(a) (b)

Figure 3.18: Slot antenna (a) and the numerical approximation of the simulated far-field radiation pattern (b).

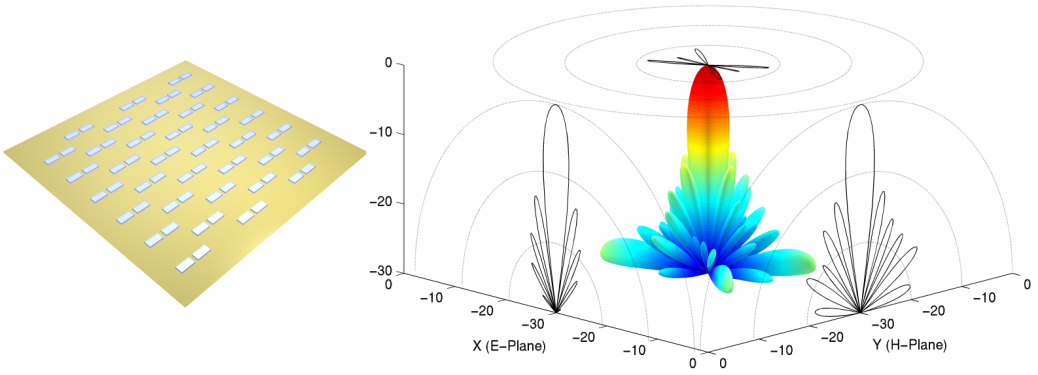

(a) (b)

Figure 3.19: Slot antennas in a triangular lattice (a) and their resulting simulated far-field radiation pattern (b).

provement. Note that this benefit applies only to radiation from the output antenna.

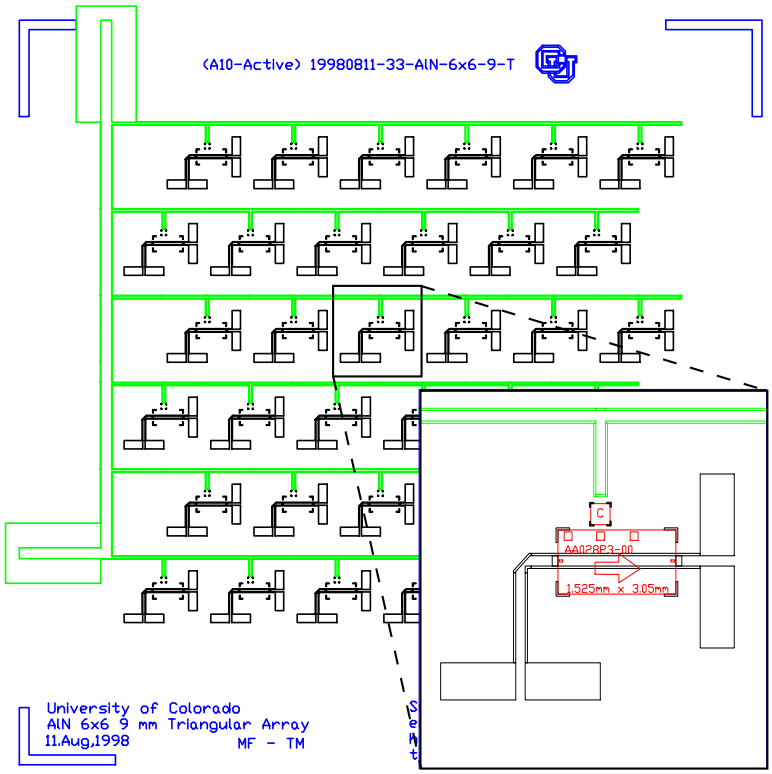

Figure 3.20: Schematic of array layout with unit cell enlarged.

The final array is shown in Figure 3.20. The array has 36 9-mm 0.9λ unit cells arranged in a 6×6 triangular lattice. In each unit cell, the input slot antenna receives power from an incident vertically-polarized plane wave. The received power is coupled onto the 50-Ω CPW transmission line and is amplified by a commercial low-cost MMIC driver amplifier. The amplified power is re-radiated in the horizontal polarization by the output slot antennas and is the coherent combination of all element outputs. Isolation and stability are provided by the orthogonally polarized input and output antennas.

3.2 Fabrication

3.2.1 Photolithography and Chemical Processing

The small dimensions and the fragility of the chosen substrate exclude the use of mechanical milling as a means of fabrication. The smallest slot dimension, the CPW gap, measures 75 μm in width.

To simplify fabrication, commercially-available metalized AlN substrates are obtained. A process using positive photoresist offers higher yields and quicker turn-around relative to a process which uses negative photoresist. The positive resist can be stripped using acetone (ACE) and isopropyl alcohol (IPA), whereas stripping negative resist requires a noxious proprietary chemical. Quick removal of the positive photoresist is beneficial if a flaw in the photoresist is discovered after the development step.

The fabrication process used to create planar microwave circuitry in a solid-state clean room has improved over time. In the beginning a yield of one circuit in five (20%) was typical. Current yields are around 90% with a single substrate in a batch of ten showing a defect. The process is included as an aide to those who wish to use similar fabrication techniques in the future.

Mask Preparation

A mask is created in AutoCAD [51] according to the dimensions converged upon in the simulation phase. To compensate for overetch during the final chemical-etching phase, slots are reduced in dimension by an empirically

chosen 20 μm. After the procurement of the mylar mask, it is cropped to a size which fits the alignment holder and cleaned with acetone and IPA. The remaining steps take place concurrently in a clean room. The clean-room processing time is approximately five hours for the parallel processing of two substrates with four hours consumed by photolithography and one hour by chemical processing.

Photoresist and Alignment

Standard spin techniques on square substrates is possible with the aid of an oversize vacuum chuck. Hoechst AZ4210 positive photoresist is spun on the substrate at 3000 rpm for 30 s. The photoresist is pre-baked at 90° for 20 min. Inspection after pre-bake should reveal uniform photoresist over the majority of the substrate, with a noticeable thickening at the corners. If the corners of the substrate require patterning, it is necessary to increase exposure time at the corners to compensate for the increased photoresist thickness.

After the application and pre-bake of the photoresist the substrate and mask are aligned and secured in an alignment holder. Because substrate is non-standard, the use of a mask aligner is not possible. This necessitates the use of a custom alignment holder, which is fabricated from a Delrin base and glass sheet secured by six vinyl screws. The holder is specially designed for accommodating the AlN substrate and is used in conjunction with a standard ultraviolet (UV) light source.

Exposure and Etching

Exposure is performed with a UV light source for a duration of 60 to 120 seconds depending on the photoresist thickness (a function of spin-on rate) and the light-source intensity. It has been found through trial and error that errors at this stage are almost invariably caused by underexposure. If the development fails, retry the procedure with a longer exposure. If the thicker photoresist in the corners contain a pattern, it is wise to cover the center after the standard exposure time to expose the corners while preventing overexposure in the center.

For copper, etching is performed with a 5% solution of sodium persulfate at 60°C for 10 to 20 minutes depending on the amount of agitation in the solution. Sodium persulfate is preferable to ferric chloride as an etchant as sodium persulfate is transparent allowing the etching process to be carefully monitored. Defects in the photoresist can be repaired before etching with a water-proof ink. Conversely, acetone may be used to remove unwanted photoresist.

In order to achieve accuracies on the order of $\pm 10\,\mu$m, the substrate must be removed from the etchant at the moment the last unwanted copper vanishes. It is often the case that portions of the substrate will etch before others leading to feature variations across the face of the substrate. Uniformity of etching across the substrate limits the smallest feature that this technology can provides. After etching, the photoresist is easily removed with alternate

applications of acetone (ACE), trichloroethane (TCA), and isopropyl alcohol (IPA).

Post Processing

Post processing in the form of additional etching or the deposition of additional metal layers may be required. For example, the substrate used for Array A has a 4 μm layer of gold affixed to the AlN by means of a titanium-tungsten (TiW) alloy carrier. The TiW carrier is removed with a 50% solution of hydrogen peroxide (H_2O_2). The substrate used for Array B has a 4.3 μm layer of copper. An additional 2 μm layer of gold has been added after etching by electroplating.

Quality of Fabrication

To gauge the quality of fabrication, several substrates are photographed and measured under a microscope. The rounded features seen in Figure 3.21 have a radius equal to the overetch. The overetch with respect to the mask features for the AlN arrays is between 26 and 32 μm. The rounded corners are very small relative to a wavelength and have little effect on the electrical performance of the circuits.

Given that the masks are designed to compensate for 20 μm of over-etch, the net overetch is between 6 and 12 μm. Nonuniform etching due to variations in metal thickness and etchant flow rate can be seen in (Figure 3.22(a)) and create a $\pm 2.5\,\mu$m meander in the lines. Under high magnification rough-

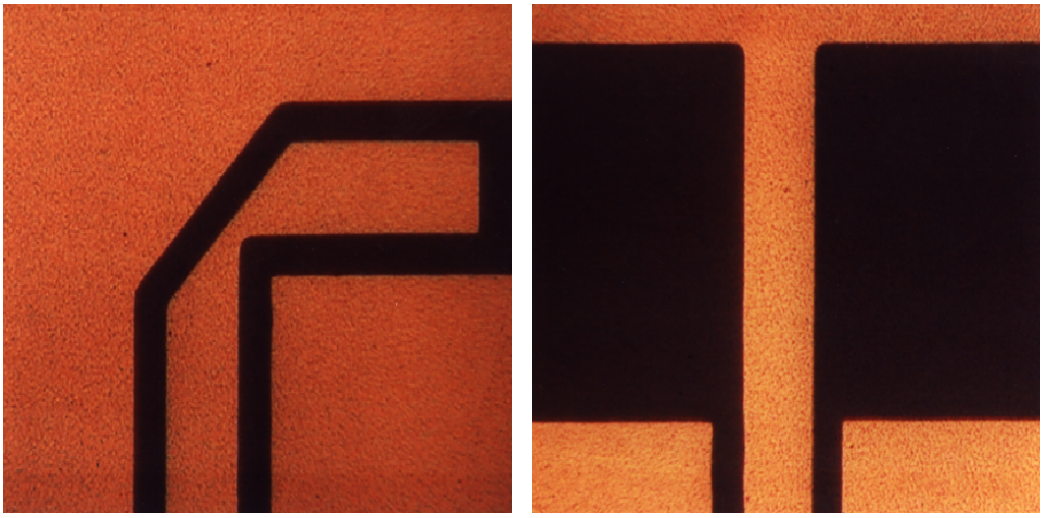

(a) (b)

Figure 3.21: Microscope photographs show the effects of over-etching on antenna (a) and CPW bend corners (b). The photographs are approximately 1.4 mm square.

ness due to the gold structure results in features $\pm 0.625\,\mu$m in size which contribute to line loss (Figure 3.22(b)).

The over-etch and meander yield a calculated transmission line impedance of $53 \pm 0.15\,\Omega$. Approximate calculations indicate that the trapezoidal edges created as a natural byproduct of etching and the rough gold edges increase guide loss by approximately a factor of two. Multiplying the simulated line loss by that factor gives a loss of $\alpha_c = 0.06$ dB for the length of line in a unit cell.

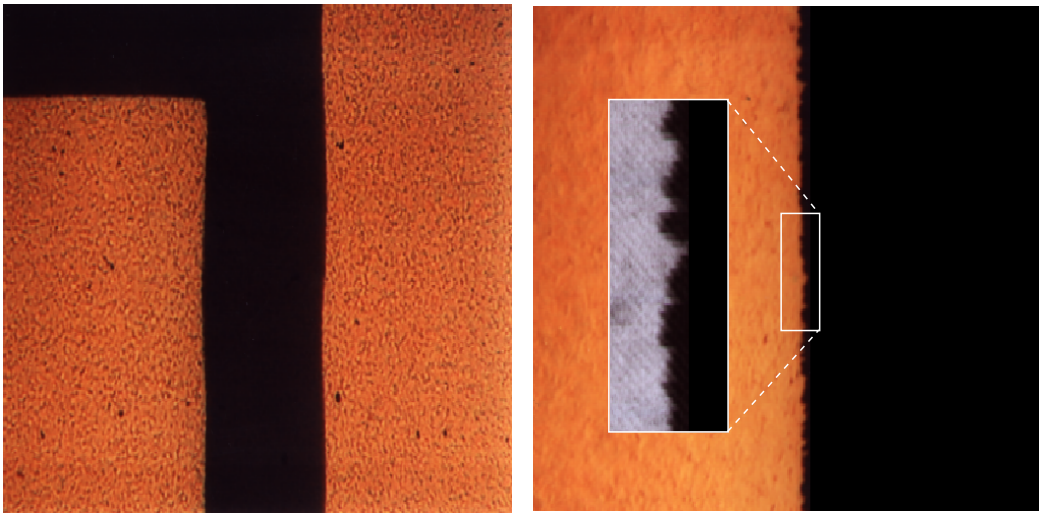

(a) (b)

Figure 3.22: Meandering (a) and roughness (b) of the CPW edges contribute to transmission line loss. The photographs represent areas of 300 μm square (a) and 60 μm square (b).

3.2.2 Device Attachment and Wire Bonding

Upon completion of chemical processing, the substrate is ready for the final stage of fabrication – affixing the devices and wirebonding. These processes are inherently intertwined requiring alternating phases of attaching and wirebonding followed by integrity testing. Depending on the number of bonds, this phase can take anywhere from two weeks in the case of Array A to a month for Array B. The extensive fabrication time is due to the relatively delicate microscope work required during the bonding, the epoxy cure time, and the complex task of wirebonding. It is the goal of future projects to eliminate time-consuming serial fabrication in favor of efficient parallel fabrication.

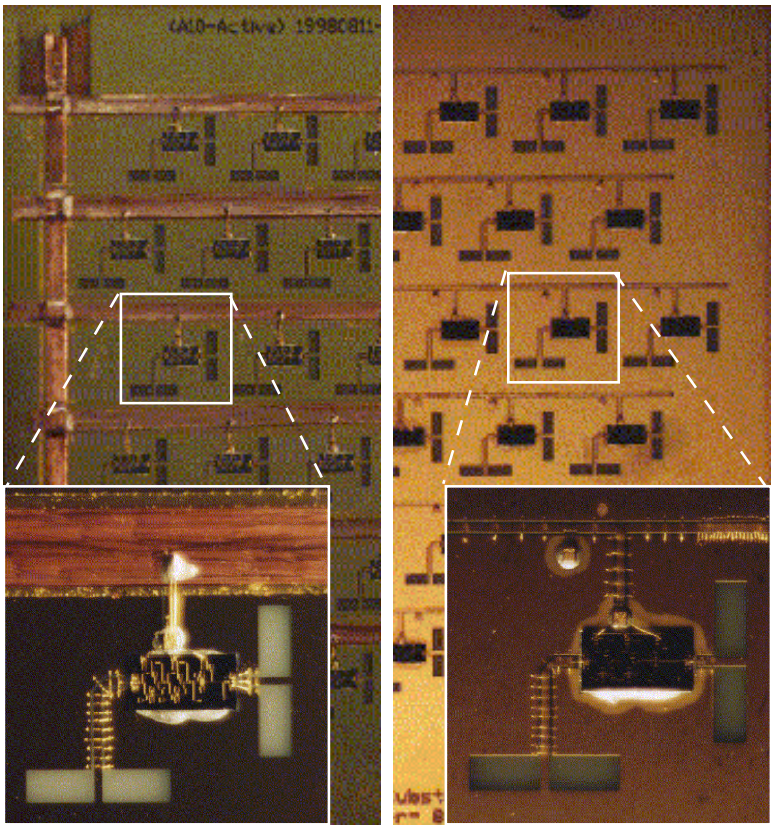

Figure 3.23: Composite photograph of Array A and B shown with unit cells enlarged. Note the supplemental bias lines on Array A and the additional air bridges on Array B. The arrays are 76 mm square with 36 9-mm unit cells arranged in a triangular lattice.

The MMICs and capacitors are attached under a microscope with *Epoxy Technology* H20E conductive silver epoxy. Both arrays have 36 MMIC amplifiers whose DC impedance is checked before bonding and after curing. Array A has 40 chip capacitors which are all 47 pF. Array B has 160 chip capacitors comprised of equal amounts of 47 pF and 100 pF values.

A *Marpet Enterprises* 1204W wirebond machine is used to create the RF and DC connections as well as the transmission-line airbridges. Standard 25.4-μm-diameter gold bond wire is used, which, according to quasi-static approximations, has an inductance per unit length of approximately 1 nH/mm. Array A and Array B have 1200 and 2200 wirebonds respectively. The majority of the additional wirebonds on Array B are used on the bias lines as a shield to enhance stability. A composite photograph of the completed active-antenna arrays is shown in Figure 3.23. It highlights the different bias lines and metalizations.

Chapter 4

Ka-Band Active-Antenna Array Measurement and Analysis

4.1 Amplifier Array Measurements

In this work small-signal gain, resonant-mode gain, and saturated output power are presented on two experimental *Ka*-band active-antenna arrays (referred to as Array A and Array B) of identical RF architectures. The arrays differ only in the implementation of the biasing network and substrate metalization thickness. Section 4.1.1 presents measurements of the intra-unit-cell elements such as lines, bends, antennas, and antennas in an array environment. Small-signal gain results are presented for far-field standard-horns,

near-field hard-horn, and resonant-mode measurements in Section 4.1.2. Saturated power measurements are discussed in Section 4.1.3 followed by pattern measurements of the passive and active arrays in Section 4.1.5. Section 4.1.4 contains thermal measurements. These measurements adhere to the standards discussed in Chapter 2.2 on page 15.

4.1.1 Elements of the Array

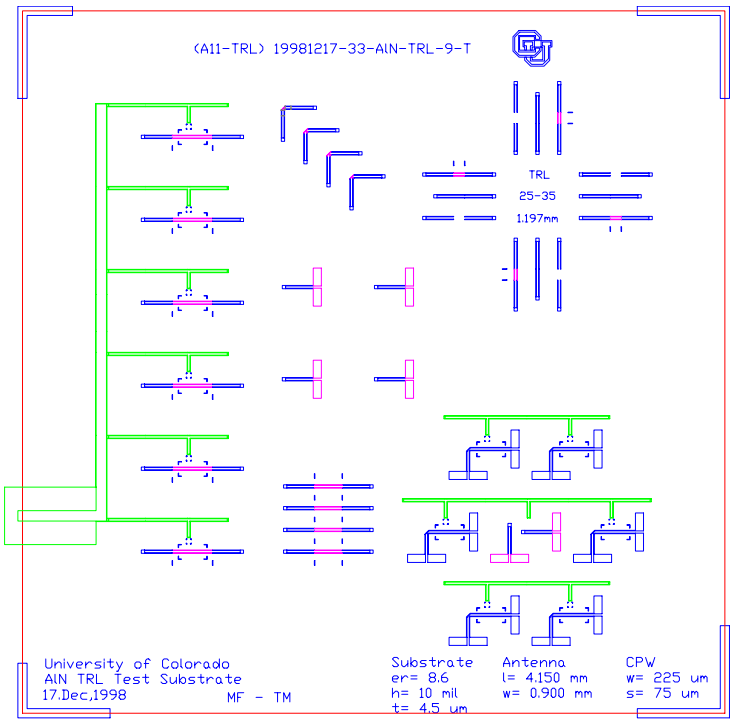

Figure 4.1: Schematic of an AlN test substrate fabricated to measure individual MMICs, bends, lines, antennas, and a small 7-element subarray.

To gauge the accuracy of the simulations, various individual array com-

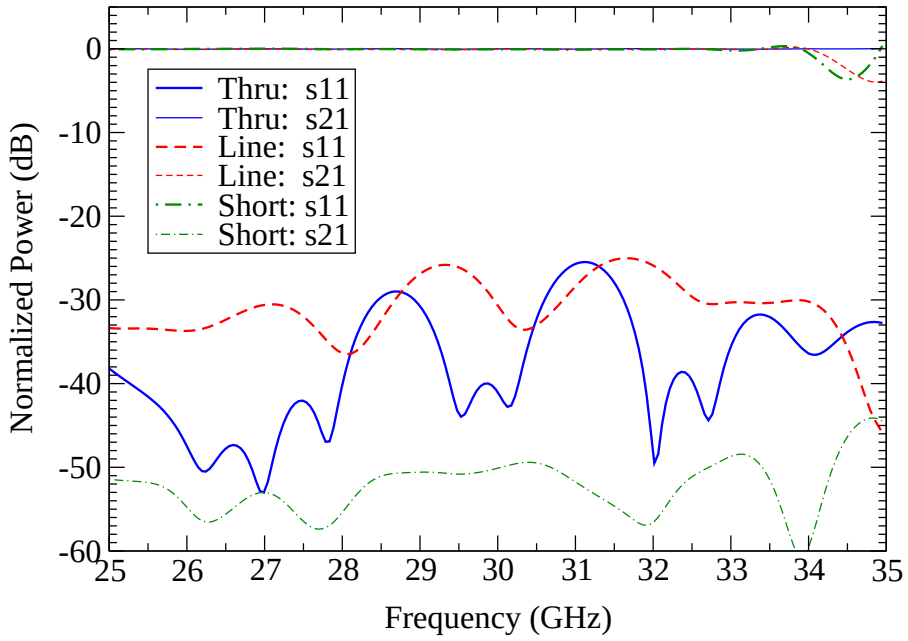

Figure 4.2: Measured s-parameters of the CPW TRL calibration set.

ponents are fabricated on a separate AlN substrate for characterization (Figure 4.7). A *Cascade Microtech* analytical probe station 9000 with two *Cascade Microtech* ACP50 ground-signal-ground (GSG) CPW probes with 250-μm pitch are used to measure the circuits. Calibration is performed with a transmit-reflect-line (TRL) calibration set fabricated on the same AlN substrate. The measurements of the standards are shown in Figure 4.2. Note that above 33 GHz the accuracy of calibration declines. The components measured are the *Alpha* MMIC, the CPW line and the 90-degree compen-

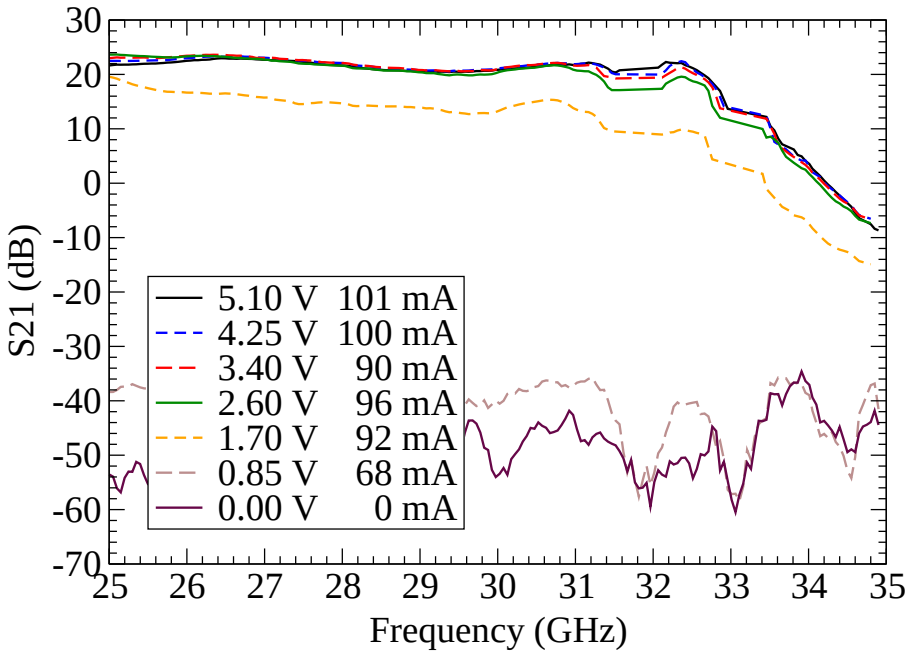

Figure 4.3: Measured gain of the Alpha AA028P3-00 MMIC in approximately 1-V increments.

sated bend, the slot antenna, and the input and output slot antennas in a 7-element array environment.

The measured gain of a single MMIC is shown in Figure 4.3. The gain characteristics agree within 2 dB with the manufacturer's specifications in Figure 3.2 on page 28 (and extends the measurement range from 26–32 GHz to 25–35 GHz).

The transmission line measurements place the return loss and insertion

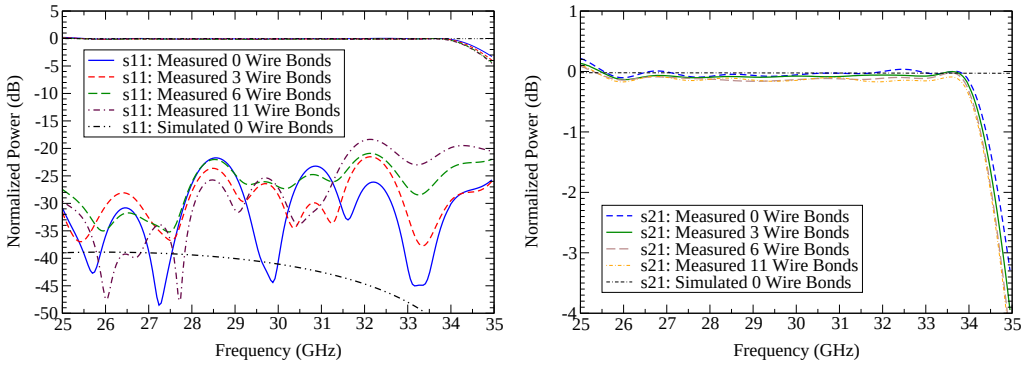

(a) (b)

Figure 4.4: Simulated and measured reflection and transmission coefficient of a 3-mm CPW line showing both parameters (a) and a close up of the insertion loss (b).

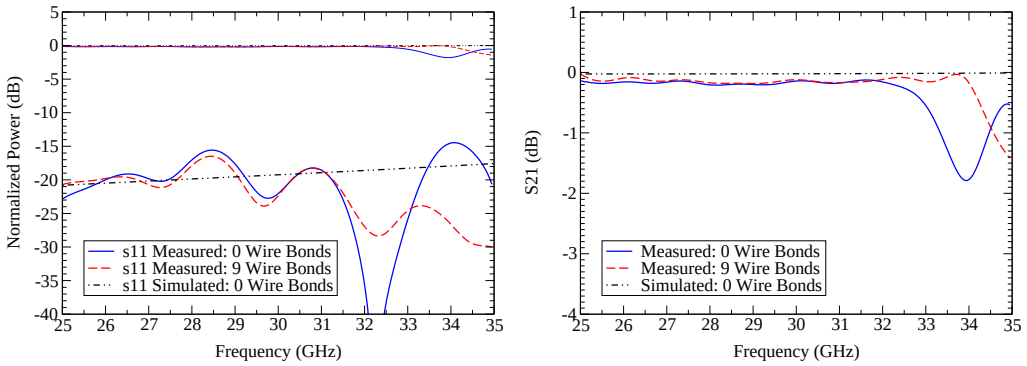

(a) (b)

Figure 4.5: Simulated and measured reflection and transmission coefficient of a 90-degree compensated CPW bend showing both parameters (a) and a close up of the insertion loss (b).

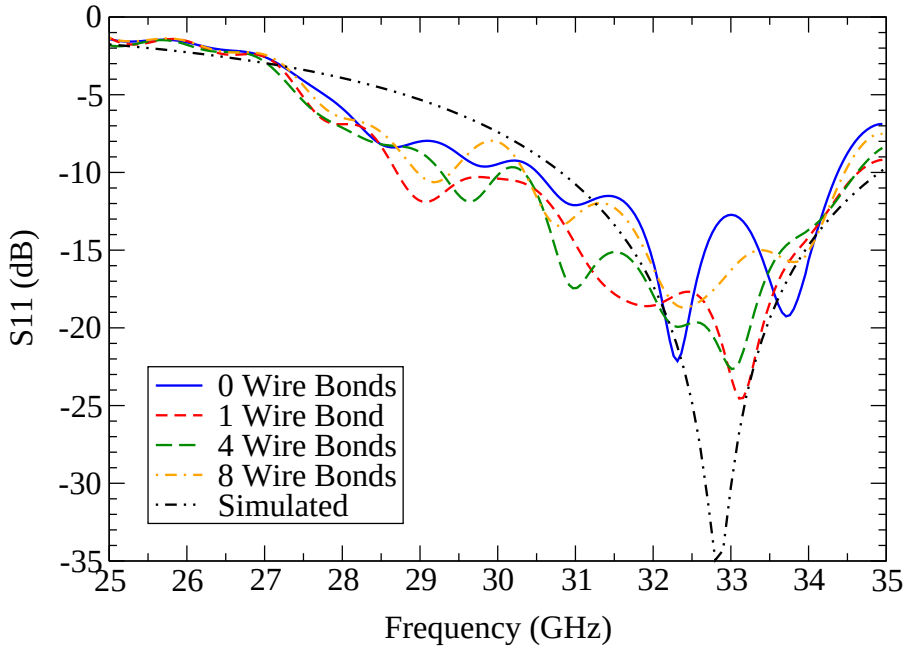

Figure 4.6: Simulated and measured reflection coefficient of a slot antenna on AlN.

loss for the 6-wire-bond line below -20 dB and -0.15 dB. (Figure 4.4). Increasing the number of wirebonds increases the insertion loss up from -0.10 dB for 0 wirebonds to -0.18 dB for 11 wirebonds. The line length is 3 mm, which equates to a loss of -0.05 dB/mm. Simulations agree within the accuracy of the calibration which is shown in Figure 4.2.

The 90-degree compensated bend performs similarly with a return loss and insertion loss below -15 dB and -0.21 dB (Figure 4.5). The addition of 9

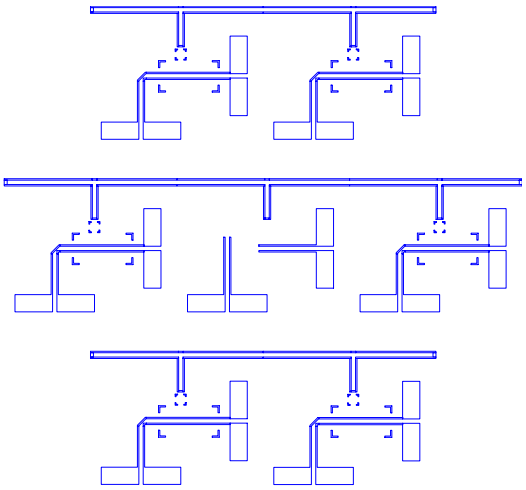

Figure 4.7: Subarray schematic.

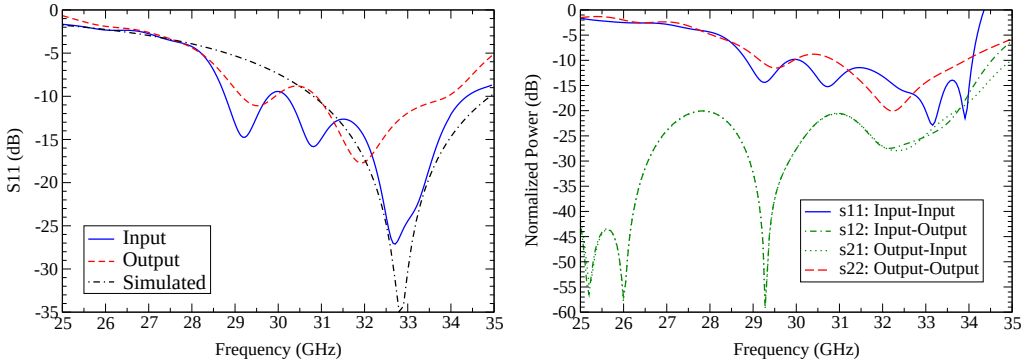

(a) (b)

Figure 4.8: Simulated and measured reflection coefficient of the input and output slot antenna in a seven-element subarray (a); measured coupling between the input and output antenna inside the seven-element subarray (b).

wire bonds to the compensated bend reduces the insertion loss by approximately 0.06 dB over the bandwidth.

The measured resonance of the slot antenna is 32.6 GHz, which is shifted 150 MHz (0.5%) from the simulated value of 32.75 GHz (Figure 4.6). The slot antenna has a measured and simulated bandwidth of 3.7 GHz (11%) and 4.3 GHz (13%), respectively. The antenna simulation includes an increase in antenna and CPW dimensions resulting from overetching in the AlN test-substrate fabrication process. The wire bonds have little effect on measurements with high reflection (from 25 to 30 GHz). The greater variation for measurements with low return loss is attributed to calibration error and reflections from the probe-circuit interface.

In an attempt to study the antenna in an array configuration, a small 7-element subarray is fabricated on the AlN test circuit. The subarray consists of a central unit cell surrounded by six normal unit cells (Figure 4.7). The central unit cell is designed such that the input and output antenna may be individually probed. The input and output antennas, located on the left and right respectively, are characterized independently using different channels on the network analyzer (Figure 4.8(a)). It is believed that the differences in the frequency response are due to variations in the calibration between the two channels. Simulations predict no change in frequency for the two antennas.

The coupling from the input and output antenna in the unit cell is measured by simultaneously probing both the input and output antenna. Because of the proximity of the probe points to each other, as well as to the radiating structures, such a measurement is approximate. As seen in Figure 4.8(b)

the resonances of the antennas with respect to Figure 4.8(a) have shifted as result of probes. Even with limited accuracy, measurements evince the coupling between input and output antennas is at or below -20 dB, which is close to the simulated value of -25 dB.

4.1.2 Small-Signal Gain

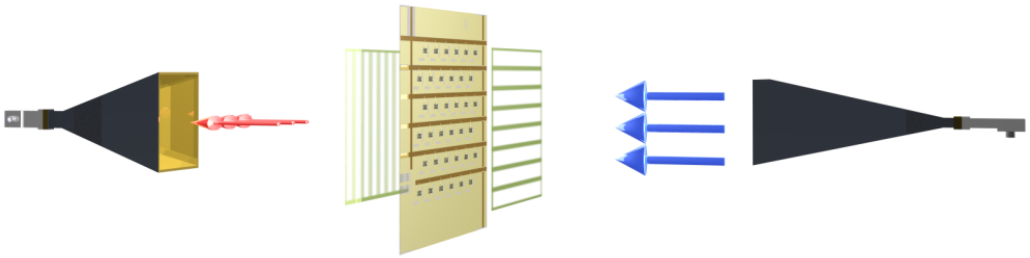

Figure 4.9: Gain measurement setup for the active antenna array. Polarization on the input is vertical and horizontal on the output.

The characterization of the arrays is performed with three measurements: a small-signal far-field gain measurement with standard horns, a small-signal near-field gain measurement with hard horns, and a large-signal far-field power measurement with standard horns.

For the small-signal far-field measurement, two 21.5-dB cross-polarized standard horn antennas are placed $60\lambda_0$ from either side of the array (Figure 4.9). Measurements are performed with an HP 8510C vector network analyzer calibrated to a free-space through. In theory, tuned polarizers should increase the gain of the array 6 dB by enforcing unidirectional radiation of

Table 4.1: Measurement setup for standard-horn, hard-horn, and resonant-mode small-signal gain measurements.

Measurement	Horn-to-Array r_1 (cm)	Array-to-Horn r_2 (cm)	Repeater Bias B_r (dB)
Small Signal (Standard)	62.5 cm	65.5 cm	-3.3 dB
Small Signal (Hard Horn)	6.6 cm	5.9 cm	–
Saturation	101.0 cm	64.0 cm	-5.1 dB
Pattern	101.0 cm	64.0 cm	-5.1 dB

Table 4.2: Standard-horn, hard-horn, and resonant-mode small-signal gain measurements.

(a) Standard-horn small-signal gain measurements.

Array	Freq (GHz)	Gain (dB)	BW (GHz)	On/Off Ratio (dB)	G_a (dB)
A	31.02	2.1	0.34	34	10
B	31.40	6.5	0.50	38	14

(b) Hard-horn small-signal gain measurements.

Array	Freq (GHz)	Gain (dB)	BW (GHz)	On/Off Ratio (dB)	G_a (dB)
A	30.32	2.0	0.22	25	10
B	31.30	4.7	0.70	35	12

(c) Resonant-mode gain measurements.

Array	Freq (GHz)	Gain (dB)	BW (GHz)	On/Off Ratio (dB)	G_a (dB)
A	31.52	10.7	0.48	44	25
B	31.47	11.8	0.26	40	25

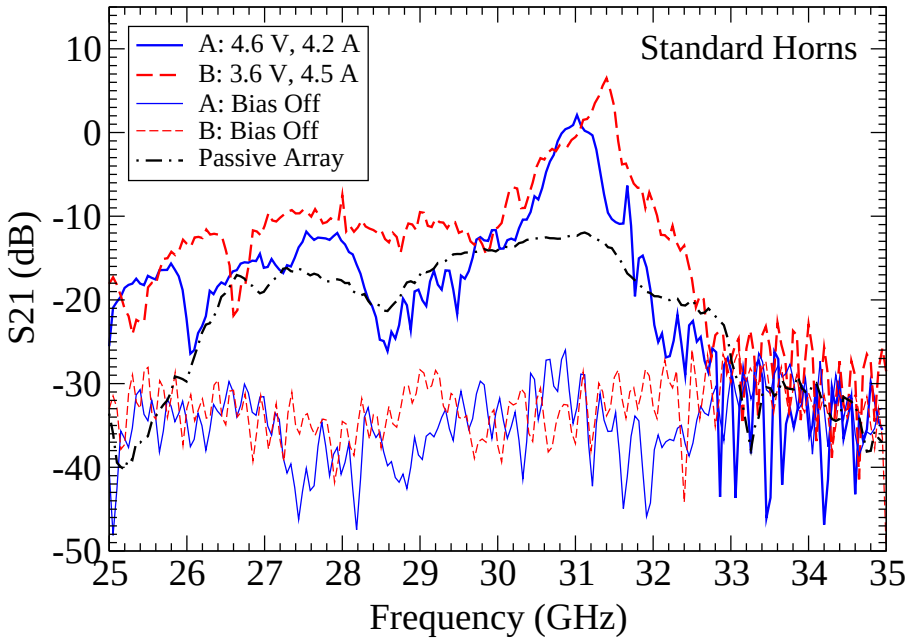

Figure 4.10: Small-signal frequency response of the arrays fed in the far-field by standard-gain pyramidal horn antennas.

the slot antennas. Measurements place the actual increase in gain at 4.7 dB [44], the shortfall attributed to a 1.3-dB polarizer loss. The polarizers are fabricated from standard computer ribbon cable. The lower conductivity of the wires as well as the plastic cladding is is believed to be the source of the polarizer loss.

Figure 4.10 shows the measured gain of the passive and active arrays with respect to a through calibration. Measurements are summarized in

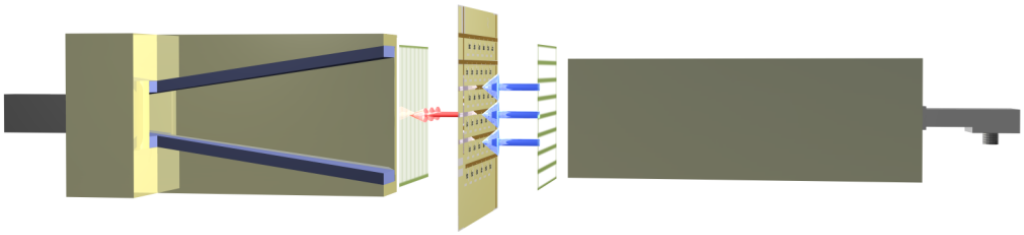

Figure 4.11: Gain measurement setup for the active-antenna array with the hard-horn antennas. The receiving hard horn is shown in cross section with the loading dielectric highlighted.

Table 4.2(a). The average gain contributed by the MMIC amplifiers is 10 dB. The repeater bias, included in Table 4.1, is not used to renormalize any of the tables or figures. All gains are with respect to a free-space through calibration.

Near-field small-signal gain measurements are performed in a similar fashion using two cross-polarized hard-horn antennas $6\lambda_0$ from the array. The hard-horn antennas are an alternative to a free-space feed and are loaded internally with dielectric to provide a uniform field distribution in the near field with simulated amplitude and phase variations of only ± 1 dB and 80° over 98% of the horn aperture[52]. The small-signal hard-horn gain measurements are shown in Figure 4.12(b) and summarized in Table 4.2(b).

The term *resonant mode* is used here to describe a second, stable high-gain mode of the amplifier. This mode is characterized by a narrow-band peak in gain, which occurs repeatably when the arrays are tuned with polarizers to select for maximum gain at 31.5 GHz. The mode is further enhanced

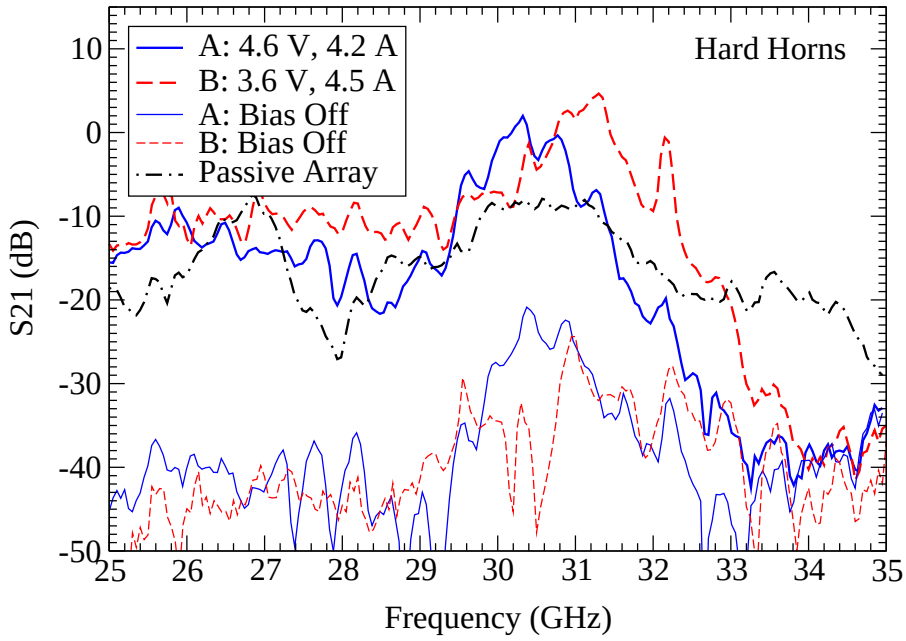

Figure 4.12: Small signal frequency response of the arrays fed in the near-field with the hard-horn antennas.

Figure 4.13: Gain measurement setup shown from above for the active-antenna array operating in resonant mode.

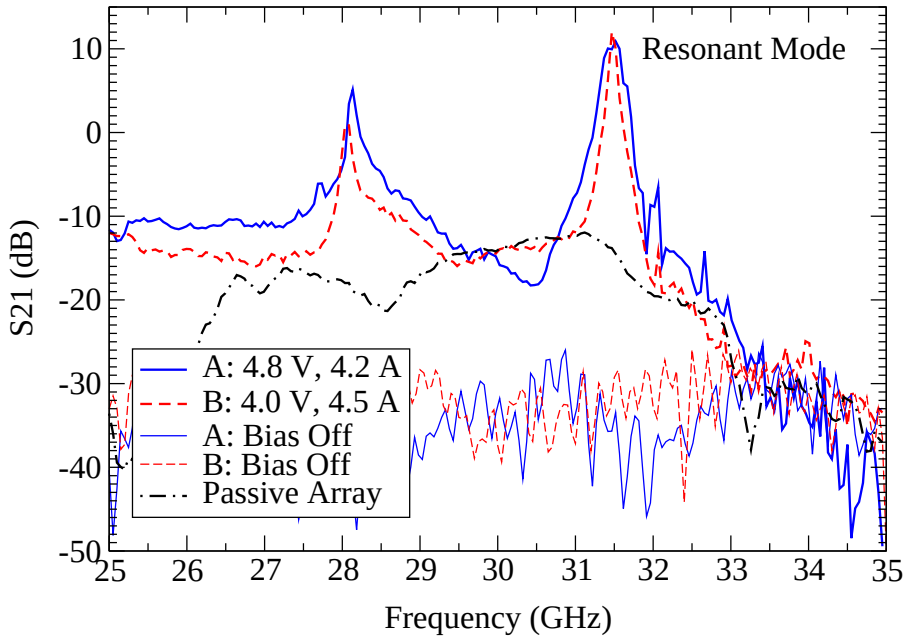

Figure 4.14: Small signal frequency response of the arrays fed in the far-field tuned for resonant-mode.

by rotating the arrays 15° off-center with respect to the optical axis. The measured gain of the amplifiers operating in resonant-mode under small-signal excitation is shown in Figure 4.14, and summarized in Table 4.2(c). The resonant mode occurs repeatably between arrays and is believed to be due to coupling from the input and output antennas by means of substrate modes enhanced by the rotation of the array.

Table 4.3: Measured saturated response with standard horns.

Array	Freq (GHz)	EIRP (dBm)	EIRP (W)	P_t (dBm)	P_t (mW)
Array A	30.40	49.5	89	25.0	316
Array B	31.15	51.6	145	27.1	513

4.1.3 Saturated Power and Gain

Far-field large-signal power measurements are performed with standard horns placed $25\lambda_0$ from the array. In place of the network analyzer, an HP83640A synthesized sweeper driving a *Litton* M-762-00 MMPM is used to provide the power required to saturate the arrays. The estimated power incident on the array is 27.7 dBm. An HP437B power meter with a high frequency power sensor (HP8487A) is used to measure the output power.

Calculation of the transmitted array power, P_t, assumes an array gain of 24.5 dB. This value is obtained by applying the Krauss approximation [53] to the measured large-signal far-field patterns shown in Figure 4.16 on page 72, and agrees closely with the gain calculated from the array's physical area [54]. The gain saturation of Arrays A and B is 7.9 dB and 7.5 dB respectively. The EIRP and output powers estimated from measured radiation patterns are summarized in Table 4.3. Measurement accuracies are $\pm$ 1 dB.

4.1.4 Thermal

Both arrays are designed to withstand the steady-state thermal gradient caused by conductive cooling through the substrate. In practice, however,

the arrays are cooled by means of either natural or forced convection over the surface. With the arrays mounted vertically and under small-signal excitation, natural heat convection leads to measured steady-state temperatures of 69° C and 62° C for Array A and B, respectively. Forced-convective cooling, using two fans with a flow of $1\,m^3$/minute, drops the maximum steady-state temperatures for Array A and B to 39° C and 38° C. Although natural convection is sufficient to keep the MMICs below their maximum operating temperature in small-signal operation, forced convection minimizes variation in temperature with respect to bias point. This, in turn, minimizes the temperature-dependent gain and phase variations of the MMIC amplifiers and increases combining efficiency.

4.1.5 Far-Field Patterns

Pattern measurements are performed using far-field standard-horn antennas $60\lambda_0$ from the array. Measurements are performed with polarizers under large-signal excitation. The theoretical and measured E- and H-plane patterns for the passive array are shown in Figure 4.15. Active arrays are shown in Figure 4.16. Theoretical array patterns are calculated by multiplying the array factor by the pattern of the slot antenna. The slot antenna pattern is modeled as a cosine-squared toroid pinched to zero at the substrate.

Although one would expect large side-lobes with a $0.9\lambda_0$ unit cell, side lobes in both planes are minimized. The array's triangular lattice minimizes the side lobes in the E-plane. In the H-plane, side lobes are eliminated by

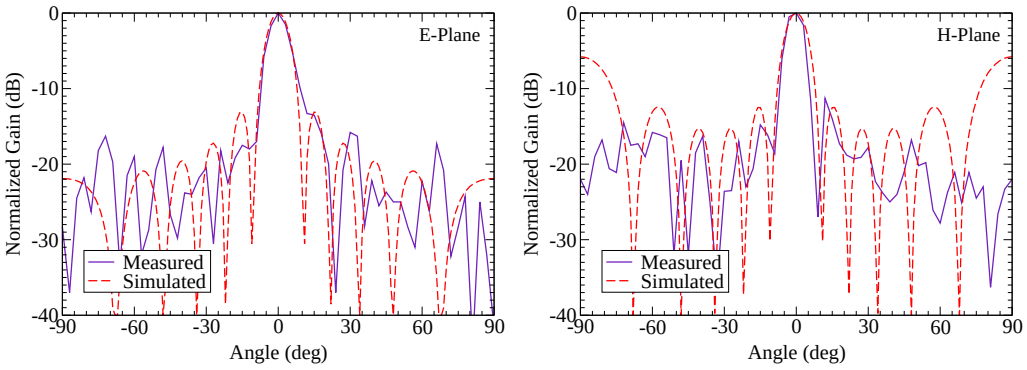

(a) (b)

Figure 4.15: Pattern measurement of the passive array in the E-plane (a) and H-plane (b).

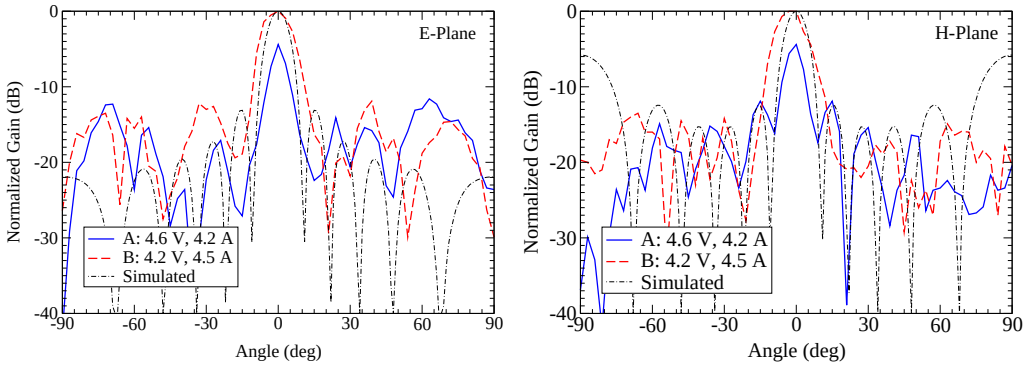

(a) (b)

Figure 4.16: Pattern measurement of Array A and B in the E-plane (a) and H-plane (b).

the radiation pattern of the slot antenna. It is believed that the difference between theoretical and active patterns is the result of variations in the

magnitude and phase at the output of individual MMICs due to fabrication and bias variations.

4.1.6 Bias Variations

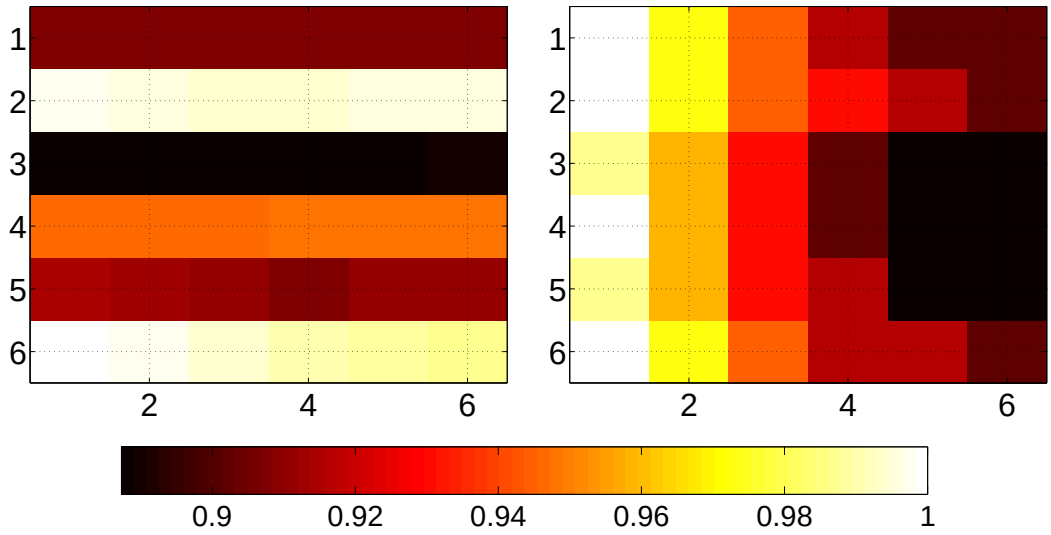

Figure 4.17: Bias levels of the array measured at the MMIC after modifications to the bias line network.

Voltage variations are measured across the bias network without RF input. Figure 4.17 shows the normalized measured voltage deviation along the bias network at each MMIC due to the bias ladder network. Voltage variations for Array B match the expected values within 5% relative error based on Equations (3.1) and (3.2). Array A's vertical voltage uniformity differs from theory due to resistive bus-bar connections (see Figure 3.11 on page 38).

4.1.7 EO Measurements

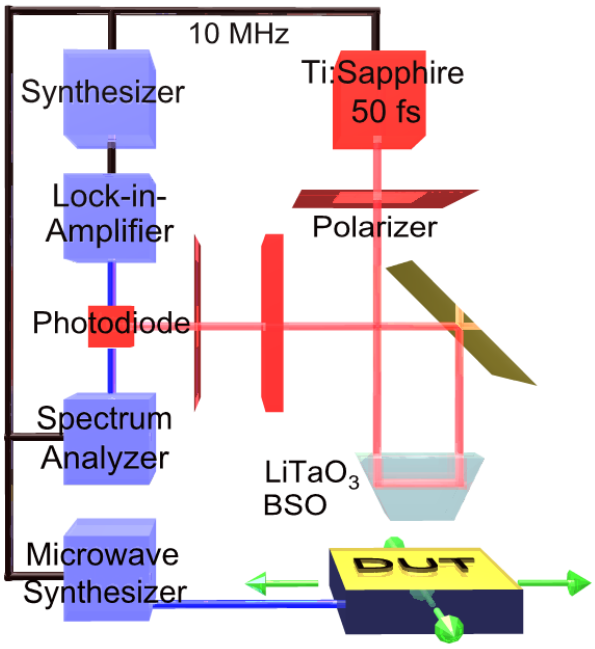

Figure 4.18: Block diagram of the electro-optical measurement setup.

An electro-optic (EO) near-field mapping technique, developed and implemented at the University of Michigan, is used to characterize the evanescent fields of the arrays. Near-field mapping of the arrays is performed at the Center for Ultrafast Optical Science and Radiation Laboratory at the University of Michigan by Todd Marshall (from the University of Colorado) and Kyoung Yang (from the University of Michigan) under the supervision of Professor John Whitaker. This technique simultaneously measures the magnitude and phase of the fields by scanning a non-intrusive electro-optic crystal over the

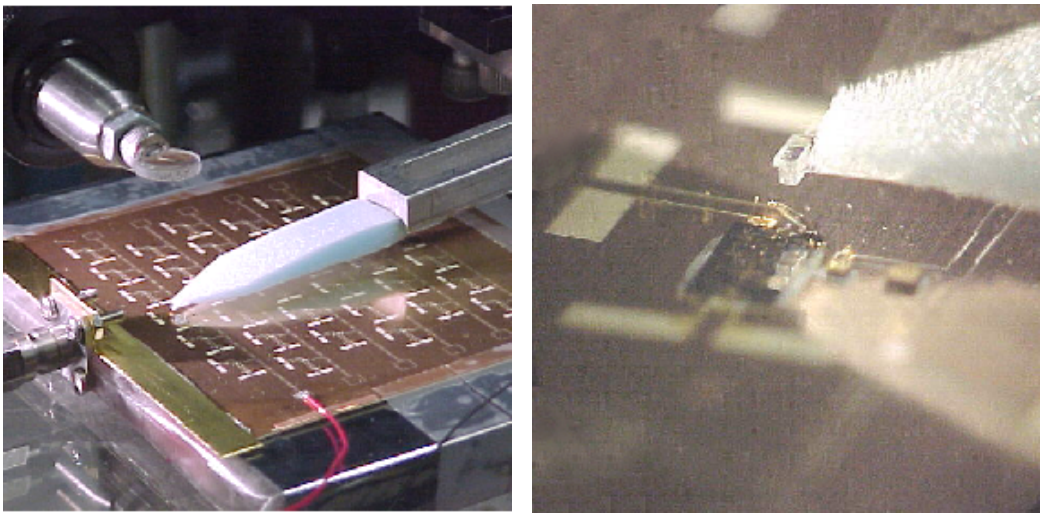

(a) (b)

Figure 4.19: Photograph showing the array and crystal during the measurement of an antenna far away (a) and close up (b).

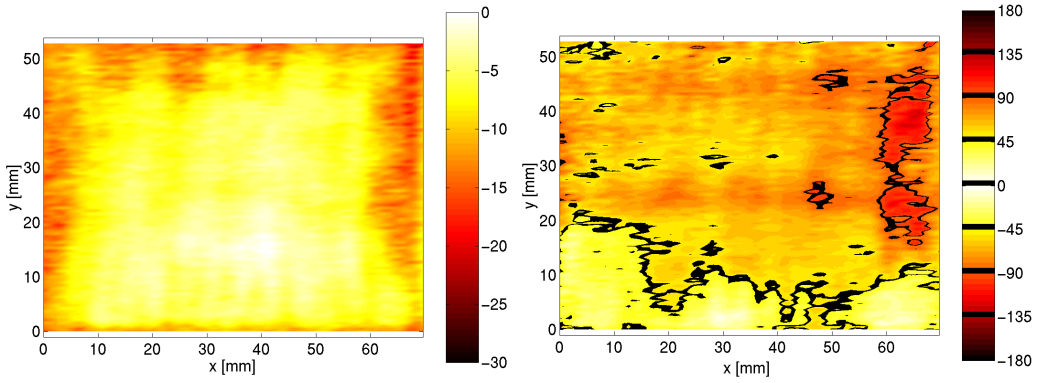

(a) (b)

Figure 4.20: Electro-optic measurement of the magnitude (a) and phase (b) of the electric field above the hard-horn antenna.

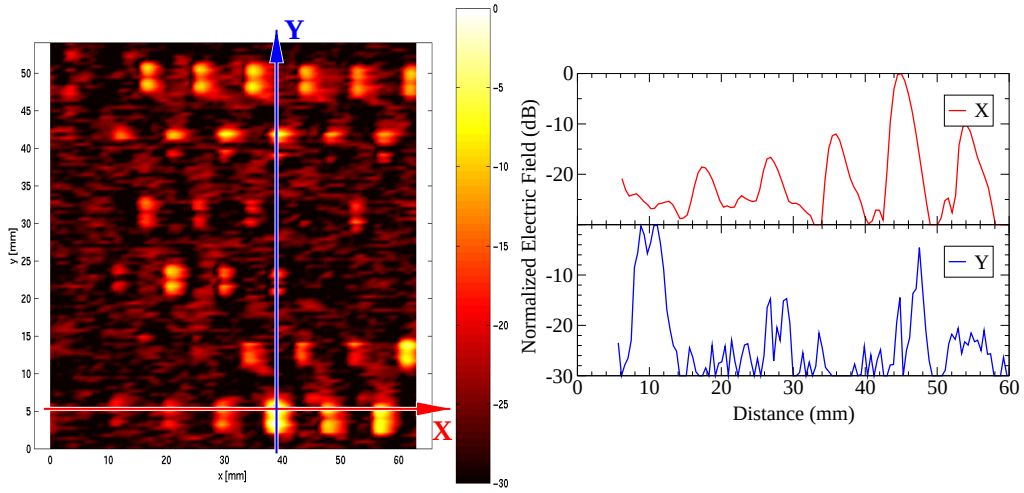

(a) (b)

Figure 4.21: Electro-optic measurements of the magnitude of the electric field above the surface of Array A. Data is shown as a full surface map (a) with two highlighted slices (b).

array [55].

The system measures the electric field by monitoring the change in polarization of laser light passing through a lithium titanate ($LiTaO_3$) crystal over the device under test. The lithium titanate crystal is suspended by a foam arm above the array to minimize the perturbation of the electric fields. A block diagram of the test setup is shown in Figure 4.18. An array and unit cell under test is shown in Figure 4.19.

During EO measurements the active-antenna arrays are fed in the near field with the same hard-horn antennas used to characterize the arrays in Section 4.1.2 on page 64. EO measurements of the hard-horn antennas to

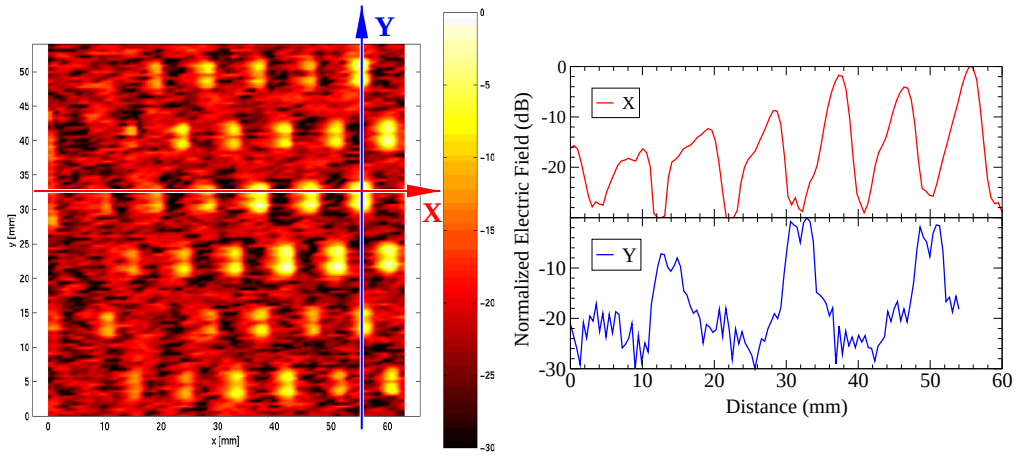

(a) (b)

Figure 4.22: Electro-optic measurements of the magnitude of the electric field above the surface of Array B. Data is shown as a full surface map (a) with two highlighted slices (b).

determine their affect on the array are shown in Figure 4.20. Analysis reveals a $\pm 10\,\mathrm{dB}$ variation in magnitude and a $\pm 90°$ variation in phase over the surface of the hard horn. It is believed that the reduction in system gain between the free-space and hard-horn measurements is due to the variation in amplitude and phase over the surface of the hard horns.

The measured near-field of Array A and Array B under hard-horn excitation are shown in Figure 4.21 and Figure 4.22. The probe is copolarized with the output antennas. In both measurements a slice through the data across the lines labeled **X** and **Y** is plotted in an adjacent graph. There is a variation in amplitude of up to $10\,\mathrm{dB}$ between elements which is believed

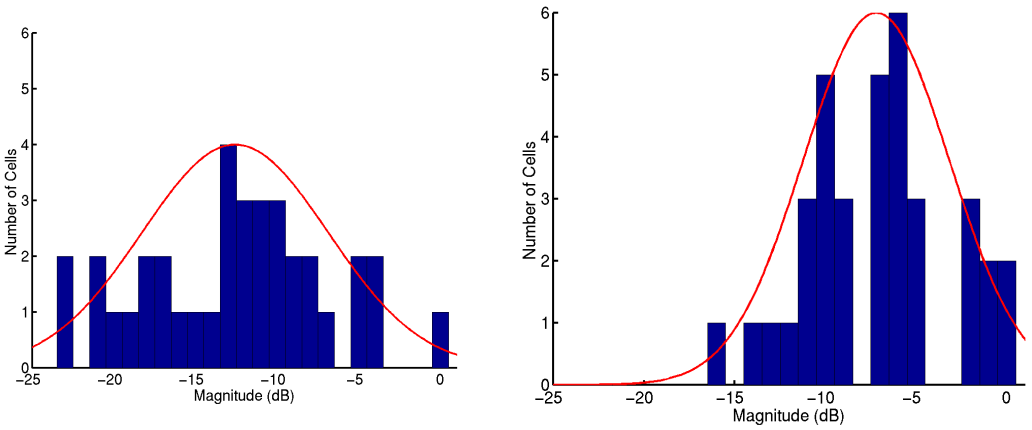

(a) (b)

Figure 4.23: Distribution of electric-field magnitudes for Array A (a) and Array B (b).

to be due to a combination of the hard-horn feed and variations in the bias levels across the face of the array.

A statistical analysis of the amplitudes measured by electro-optic sampling are shown in Figure 4.23 and summarized in Table 4.4. Array A shows greater amplitude variability than Array B as a result of voltage variations introduced by the supplemental bias lines. The variations in bias between the arrays manifests itself in the electro-optic measurements as a greater electric-field magnitude variability, in small signal measurements as reduced gain, in power measurements as lower power, and in pattern measurements as higher sidelobes.

Table 4.4: Statistical analysis of EO measurements.

Variable	Array A (dB)	Array B (dB)
Minimum Value	-23.2	-15.9
Average Value	-12.6	-7.2
Std. Dev.	5.7	4.0
Cut Off	-15.4	-9.2
Number On	28/36 (77%)	32/36 (89%)

4.2 Conclusions

The objective of the preceding travail is to design, fabricate, and characterize a low-cost watt-level *Ka*-band spatial power combiner. The maximum output power for the *Ka*-band arrays is 89 W EIRP and 316 mW of output power for Array A and 145 W EIRP and 513 mW of output power for Array B. Given that an array has 36 31-mW MMICs, the maximum output power with ideal operation is approximately 1 W. With the inclusion of 1.3 dB of polarization loss and an estimated 70% power-combining efficiency, the measured powers are as expected. The goal of generating watt-level power at 31 GHz with commercial MMICs using a spatial power combiner has been achieved. The secondary goals of thermal management and the development of a chemical process to fabricate millimeter-wave circuitry have also been achieved.

Chapter 5

K-Band Transmit-Receive Array Background

5.1 Motivation

Active-antenna array technology combines printed antennas and active devices with the goal of improving performance, increasing functionality, and reducing size relative to alternative architectures. Such arrays show potential for use in millimeter-wave commercial applications such as wireless local-area networks, electronic identification systems, and vehicle collision-avoidance radar.

This work builds upon a large body of research in transmit-only quasi-optical arrays [1]; utilizes a lens feed to improve feed efficiency and eliminates the bulk of a gaussian or waveguide feed [30, 21, 56]; and improves upon

the results of previous half- and full-duplex quasi-optical transmit-receive arrays [31, 32, 34, 33]. In [31], the transmit and receive channels are at the same frequency with isolation provided using orthogonal antenna polarization (25 dB), but due to the saturation of the input amplifier by the output, simultaneous transmission and reception is not possible. The fundamental goal of this work is to achieve full-duplex operation by using two different frequencies with multiple levels of isolation between the transmit and receive channels.

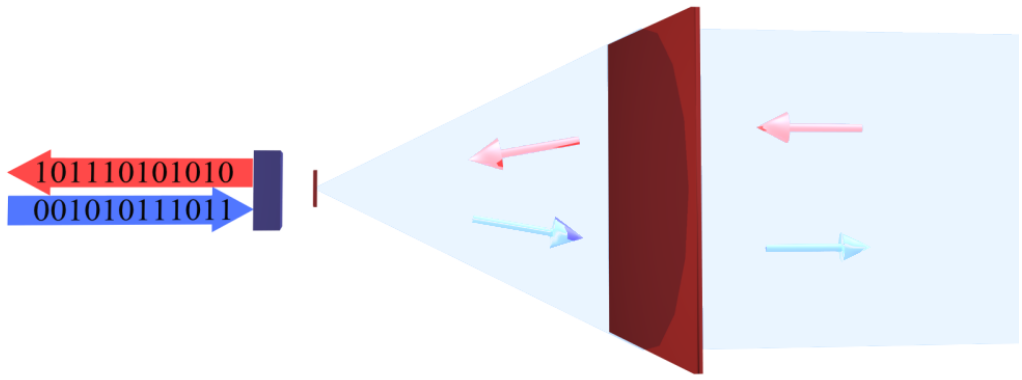

Figure 5.1: Block diagram illustrating the placement of the microwave front end in the proposed communication system.

The primary application for this full-duplex transmit-receive active-antenna array is its use as a front end to a communications system (Figure 5.1). Fed in the near-field at the focal point, the array is designed to radiate directly into space. Reciprocally, incoming signals are received from free space, amplified, and focused onto a receiver at the focal point. The purpose of using

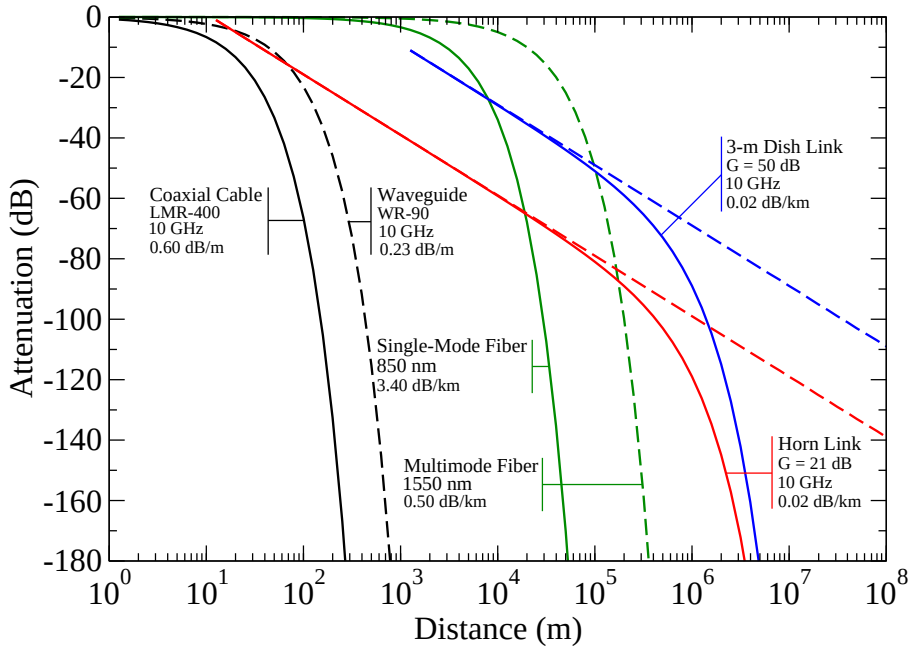

Figure 5.2: Signal attenuation due to guide or free-space loss as a function of distance. This data is calculated using $P(r) = P_0 e^{-2\alpha r}$ for guided loss and $P(r) = P_0 AG/(4\pi r^2)$ for free space loss.

free-space as a transmission medium over other confined guiding media is the low propagation loss over large distances. In Figure 5.2 it can be seen that a standard-gain horn link offers lower loss than a coaxial cable or rectangular waveguide at distances greater than a few hundred meters. The plot does not take into account atmospheric attenuation or multipath effects.

Full-duplex transmissions are used in cellular telephony, at the 890-920-MHz band and the 1.8-2.0-GHz band. Up- and down-link frequencies are

typically separated in frequency by at least 10%. Deep-space communication applications at *X*-band (7.2-GHz uplink, 8.4-GHz downlink) require that channel isolations be greater than 110 dB [57].

5.2 Figures of Merit

In addition to the figures of merit developed in Chapter 2.2 on page 15, some additional concepts are introduced to aid in the analysis of the new array. The concepts of feed efficiency as well as the introduction of lens-calibration issues are discussed below.

5.2.1 Feed Efficiency of Array Antennas

The full-duplex transmit-receive active-antenna array presented here is implemented with an integrated one-degree-of-freedom true-time-delay lens. The purpose of utilizing an integrated lens with a near-field feed is to optically control the power flow in an effort to improve feed efficiency while avoiding the complexity and weight of a gaussian-beam or waveguide feed.

The feed-loss mechanisms in a system with an integrated lens feed are similar to those of an array fed in the far field. Losses are due to the antennas and transmission lines, aperture efficiencies less than 100%, and illumination losses. In Chapter 2.2.4 on page 22, it has been demonstrated that illumination losses on the input and output can be calibrated out when characterizing the gain contributed by the active array. This also applies to a system with

a lens feed, however illumination losses on the feed side are considered to be part of the system loss and care must be taken not to arbitrarily remove them.

The illumination losses are due to spill over and nonuniform illumination. There is typically an inverse relationship between these two losses. As an illustration, in a far-field feed there is uniform phase and amplitude distributions across the face of the array at the expense of a large $1/r^2$ propagation (spill-over) loss. However, in a near-field focal-point feed of a lensing array the spill-over loss is reduced at the expense of uniform illumination. For every lens-fed array there exists a point where the product of the spill-over loss and nonuniform-illumination loss, $\eta_s\eta_i$, is at a minimum [58]. This point depends on the array geometry and the feed-horn gain.

5.2.2 Repeater Bias in a Lensing Array

As with systems utilizing free-space feeds, calibrating systems with lens feeds can be problematic. The argument for the exclusion of the repeater bias from measurements calibrated with a free-space through hinges on the concept that the setup of a measurement system and variation thereof should not affect the measurement results.

Due to a dependence of the measured gain on horn placement in the lens-array measurement system, the same argument applies. A modified correction can be defined for the lensing system which removes bias introduced by the geometry of the measurement system; applies the correction in

a manner that matches the intended deployment; and does not remove the spill-over or nonuniform-illumination loss. This is executed by a combination of a repeater-bias correction and an intended-deployment normalization. The only caveat is that the Friis transmission formula is applied to the near-field feed, making the calculation approximate.

The intended-deployment normalization is implemented by modifying the original repeater-bias equation by taking the limit of the equation as the far-field horn distance approaches infinity. Because the array is a front end for a communication system, the far-field horn may be a significant distance from the front end – up to several orders of magnitude farther than the distance used for calibration and characterization.

As discussed in Chapter 2.2.4 on page 22, the repeater bias, which is included in the ratio of the received powers in a link with and without a repeater, is given by

$$\aleph = \frac{P_{r1}}{P_{r0}} \approx G_{a1} G_{b1} G_1 \left(\frac{\lambda}{4\pi}\right)^2 \left(\frac{r_1 + r_2}{r_1 r_2}\right)^2 \tag{5.1}$$

The intended-deployment normalization is added to this correction by taking the limit as r_2 goes to infinity:

$$\lim_{r_2 \to \infty} \aleph \;\approx\; G_{a1} G_{b1} G_1 \left(\frac{\lambda}{4\pi}\right)^2 \left(\frac{1}{r_1}\right)^2 \tag{5.2}$$

Because the ratio of distances in Equation 5.1 converges for large values of r_2 with respect to r_1, the use of infinity as a reference distance provides good agreement with values obtained using real-word implementations.

Application of Equation 5.2 on the system parameters provided in Chapter 7 yield a combined repeater-bias and intended-deployment normalization of 6.5 dB. Thus with the current calibration and measurement setup, the measured gain of the array will be depressed 6.5 dB relative to the described normalization standard. By removing this factor, the sum of the feed losses and aperture efficiencies can be determined. The output array gain can then be used with the calculated losses to accurately build a link budget for a communication system. As in Chapter 4, in an effort to accurately relate data, the normalization is not included in the plots or tables, but rather stated here in the text.

Chapter 6

K-Band Transmit-Receive Array Design and Fabrication

6.1 Design

The primary goal of the *K*-band transmit-receive array is to demonstrate stable full-duplex operation with high channel isolation. There also exists a set of secondary goals, which seek to take advantage of lessons learned in the design, fabrication, and testing of the *Ka*-band array. The secondary goals seek to increase antenna isolation by means of a ground plane, simplify fabrication by eliminating vias and wire bonds, increase feed efficiency by using a lens feed, and use a wider interdigitated bias line to reduce voltage variations and suppress RF.

Full-duplex operation is implemented through the use of two isolated unit

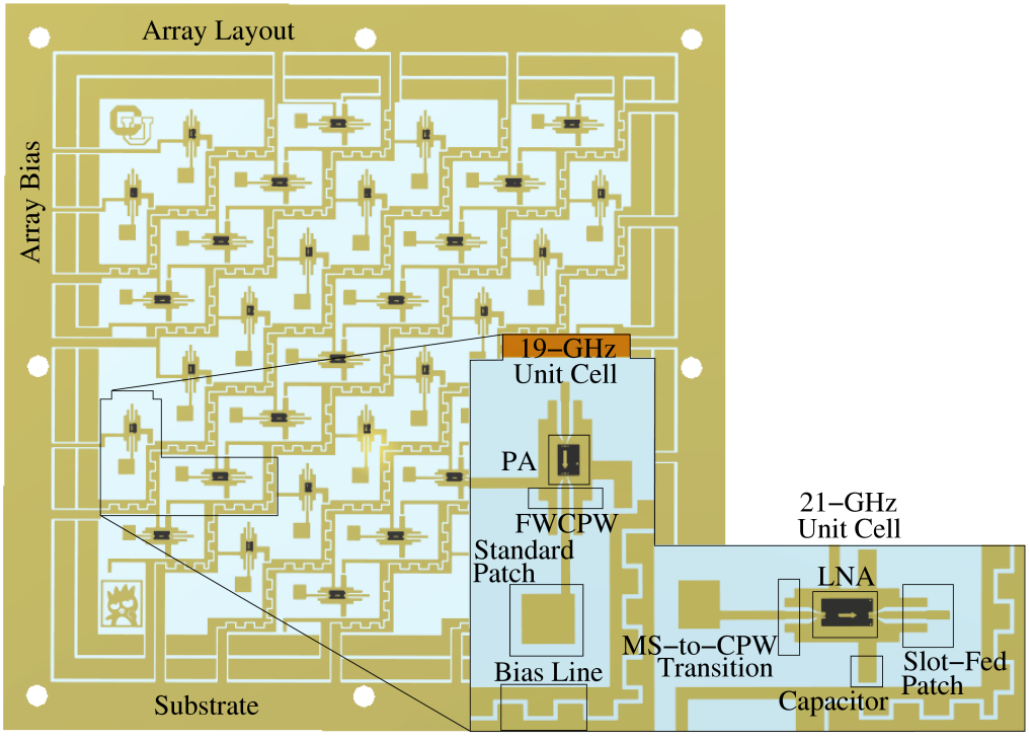

Figure 6.1: Picture of the K-band full-duplex transmit-receive active antenna array with important features labeled.

cells, one for the transmit channel, the other for the receive channel. Isolation between channels is provided by the use of band-pass components actualized as frequency-dependent transitions, couplers, and antennas. Additional isolation comes from the use of orthogonal polarizations between unit cells of different frequency on the common sides of the array. Orthogonal polarization is provided by rotating the unit cell of one channel 90° with respect to the other channel. Thus on the feed-side of the array the transmit unit cells are vertical and the receive unit cells are horizontal.

As with the *Ka*-band array, it is useful to view the design of the array as a hierarchy of levels from the individual circuit to the integrated active array. A composite drawing of the *K*-band array is shown in Figure 6.1. The figure illustrates how each individually-designed microwave component is integrated into a single unit cell and how each unit cell is arranged to form the array. It must be noted that although the information is presented in a logical flow from small to large the design is, in fact, an iterative process involving some or all of the levels at different stages in the design.

The lowest level of the hierarchy, the microwave components, requires the longest design time. During the simulation phase several components have been replaced to ensure interoperability and compliance with project requirements. In a given unit cell there exists the following microwave circuits:

- two antennas – a standard patch and a slot-fed patch
- two types of transmission lines – MSL and fCPW
- two transitions – fCPW-to-CPW and fCPW-to-CPW above a slot
- an interdigitated bias line
- a MMIC amplifier
- several capacitors – one on the bias line and the rest before the MMIC

The coming chapters discuss the method of substrate and device selection, followed by the design, fabrication, and characterization of the individual circuits and their integration into a unit cell.

6.1.1 Active and Passive Components

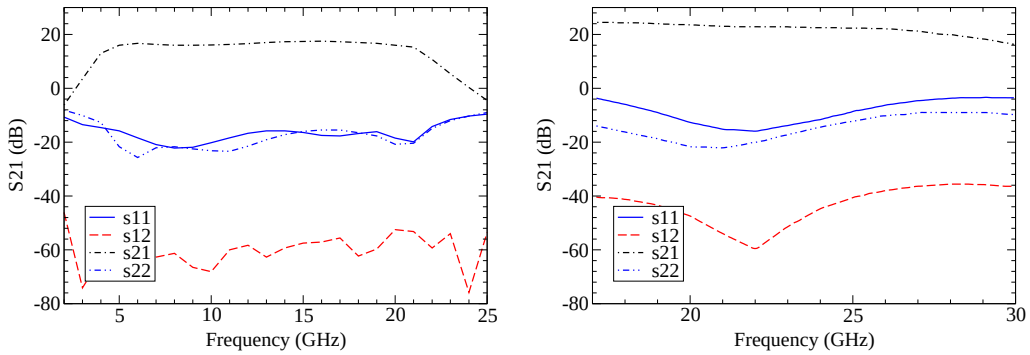

(a) (b)

Figure 6.2: Power amplifier (a) and low-noise amplifier (b) specifications. The power amplifier amplifies the outgoing 19-GHz channel. The low-noise amplifier amplifies the incoming 21-GHz channel.

Amplification is performed in transmission (19 GHz) by an *HP* HMMC-5620 single-bias power amplifier (PA) with a maximum small-signal gain of 17 dB from 6 to 20 GHz (Figure 6.2(a)). Amplification is performed in reception (21 GHz) by an *Alpha* AA022N1-00 single-bias low noise amplifier (LNA) with a maximum small-signal gain of 22 dB from 20 to 24 GHz and a noise figure of 2.5 dB (Figure 6.2(b)). To improve channel isolation and array stability, the amplifiers are chosen to provide reduced gain in the frequency range outside their respective channels. To reduce complexity of the bias lines, the amplifiers each require a single bias line and ground.

At full bias the PA draws 7.5 V 100 mA while providing 15 mW (12 dBm) of output power for an efficiency of 2%. The LNA requires 6 V 35 mA at

full bias while providing 6.3 mW (8 dBm) of output power for an efficiency of 3%. The PA and LNA generate 735 mW and 205 mW of thermal power respectively for a total 940 mW. An array with 18 PAs and 18 LNAs generates 17 W of thermal power.

Several decoupling chip capacitors are placed between the bias and the MMIC, as well as on the transmission line of every unit cell to insure stability. The capacitors are *ATC* Microcap chip capacitors measuring 457 μm square with an approximate height of 250 μm. The values of the capacitors are 47 and 100 pF, as per the recommendation in the device specification sheet.

6.1.2 Substrate

Table 6.1: Array substrate parameters shown in order of assembly.

Product	Material Description	ε_r	$\tan\delta$	h (μm)
Rogers TMM 10i	Metal	1.0	–	17.5
	Substrate	9.8	0.002	381
	Metal	1.0	–	17.5
Rohm Rohacell 31 HF	Foam	1.07	0.004	1000
Sheldahl Novaclad G2300	Metal	1.0	–	17.5
	Polyimide	3.3	0.011	50.8

The TR array is comprised of three layers of dielectric. The primary layer is *Rogers* TMM 10i, the middle layer is *Rohm* Rohacell 31 HF, and the last

layer is *Sheldahl* Novaclad G2300 (Table 6.1). The substrate which supports the majority of the microwave circuitry is Rogers TMM 10i with a thickness of 381 μm, a relative permittivity of $\epsilon_r = 9.806$, a loss tangent of $\tan\delta = 0.002$, and a metal thickness of 17.5 μm. To prevent loss in the form of surface waves, the substrate was chosen to be thin ($\lambda_d/13$) relative to the dielectric wavelength [59]. Substrate values are summarized in Table 6.1.

The primary requirements for the main substrate are high relative permittivity and stiffness. Given that the array has two separate interleaved unit cells, it is essential to minimize the unit-cell size to improve aperture efficiency. Microwave circuitry placed on a high-permittivity substrate shrinks in size proportional to $1/\sqrt{\epsilon_e}$ relative to a scaled substrate. The effective relative permittivities are given for microstrip lines [60],

$$\epsilon_e = \frac{\epsilon_r + 1}{2} \tag{6.1}$$

patch antennas [61]

$$\epsilon_e = \frac{\epsilon_r + 1}{2} + \frac{\epsilon_r - 1}{2}\left[1 + 12\frac{h}{W}\right]^{-1/2} \tag{6.2}$$

and CPW lines [46],

$$\epsilon_e = 1 + \frac{\epsilon_r - 1}{2} \frac{K(k^{'})}{K(k)} \frac{K(k_1)}{K(k_1^{'})} \tag{6.3}$$

$$k = \frac{w}{2s + w} \tag{6.4}$$

$$k_1 = \frac{\sinh\left(\pi w/4h\right)}{\sinh\left[\pi(2s + w)/4\pi\right]} \tag{6.5}$$

$$k^{'} = \sqrt{1 - k^2} \tag{6.6}$$

$$k_1^{'} = \sqrt{1 - k_1^2} \tag{6.7}$$

$$\frac{K(k)}{K(k^{'})} \approx \frac{1}{\pi} \ln\left(2\frac{1 + \sqrt{k}}{1 - \sqrt{k}}\right) \quad \text{for } \frac{1}{2} \leq k^2 \leq 1 \tag{6.8}$$

$$\frac{K(k)}{K(k^{'})} \approx \frac{\pi}{\ln\left(2\frac{1+\sqrt{k^{'}}}{1-\sqrt{k^{'}}}\right)} \quad \text{for } 0 \leq k^2 \leq \frac{1}{2} \tag{6.9}$$

Thus, on TMM 10i, the antenna size is reduced approximately by a factor of 3 relative to similar circuits on a scaled substrate with a relative permittivity of 1. Both the CPW and MSL benefit similarly.

Substrate stiffness and resistance to compression are requisite properties which provide endurance to the rigors of chemical and mechanical processing. Experience has shown that soft dielectrics will bow (often permanently) in the presence of heat after the etching process has removed metal from one of the sides. Additionally, soft dielectrics offer insufficient resistance to the foot of the wire bonder reducing the bond quality. Repeated attempts to wirebond to the same location on a soft substrate can lead substrate damage including dents and metallic delamination. The TMM substrates provide sufficient stiffness to survive the fabrication process.

The thermal conductivity of TMM substrate is around 0.8 W/mK (similar to water). This value is higher than most other commercially available substrates, but still far below the 170 W/mK of AlN. By the same analysis presented in Chapter 3.1.2 on page 29, the low thermal conductivity of the substrate makes edge cooling impossible. Given that the back of the substrate is covered with insulating foam, the only option for cooling is forced convection by a fan across the front of the array surface.

6.1.3 Element Design

Standard and slot-fed patches are the fundamental building blocks of the array. The slot-fed patch simultaneously increases aperture efficiency and provides a coupling path through the array. The standard patch on the high-permittivity substrate is small enough to be integrated into the complex front side circuitry while still providing reduced coupling relative to other antennas. The following sections present the design and simulation of the antennas and support circuitry developed for interoperability with the antennas.

Transmission Line

Coplanar waveguide (CPW) is utilized in many commercial microwave circuits where uniplanar fabrication is required. CPW conveniently provides a signal line and ground plane on the same side of the substrate, which eliminates the need for vias commonly used with microstrip transmission lines (MSL). To reduce cost and complexity in multilayer integrated circuits where

RF connectivity between layers is required, it is desirable to limit fabrication to uniplanar processing, thus ruling out other interconnects such as vias or embedded coaxial cable.

Mechanical and thermal requirements necessitate that the substrates for coplanar monolithic microwave integrated circuits (CMMIC) are metalized on one side. The resulting transmission line is referred to as conductor-backed CPW (CBCPW) [62]. In practice, the two CPW ground electrodes are limited in width in order to suppress leaky parallel-plate modes. These unwanted modes would otherwise be supported between the side grounds and the substrate ground. This type of transmission line is known as finite-width ground-backed coplanar waveguide (FW-GBCPW) [62].

The transmit-receive array makes use of a combination of FW-GBCPW (abbreviated as fCPW for the remainder of the work) and MSL joined by fCPW-to-MSL transitions. The MSL provides connectivity to the standard patch antennas and slot couplers, and the fCPW provides transitions to and from the MMICs. The benefit of using a hybrid fCPW-MSL design as opposed to a simpler all-MSL design is the reduction of fabrication complexity by the elimination of vias. The hybrid system trades simple circuitry and difficult serial fabrication for more complex circuitry and simple parallel fabrication. It is estimated that four vias per unit cell or 144 total for the array have been eliminated with no projected decrease in system performance.

The dimensions of the 50-Ω fCPW are constrained by:

- Matching the inner-fCPW-conductor width (w_{cpw}) to the MSL width

(w_{ms}). The limit being $(2s_{\mathrm{cpw}} + w_{\mathrm{cpw}}) \geq w_{\mathrm{ms}}$.

- Setting the ratio of the fCPW width to the substrate height ($(2s_{\mathrm{cpw}} + w_{\mathrm{cpw}})/h$) to a value which provides sufficient coupling to the shared ground plane without exciting the unwanted higher-order MSL mode [63].

- Choosing practical widths (w_{cpw}) and gaps (s_{cpw}) which can be fabricated and measured accurately and repeatably.

The final dimensions for the transmission lines are summarized in Table 6.2.

Table 6.2: Transmission-line specifications.

fCPW Dimensions		MSL Dimensions		Substrate Values	
w_{cpw}	$300\,\mu$m	w_{ms}	$360\,\mu$m	ϵ_r	9.806
s_{cpw}	$250\,\mu$m	λ_{ms}	6.1 mm	$\tan\delta$	0.002
b_{cpw}	$800\,\mu$m			h	$381\,\mu$m
λ_{cpw}	6.7 mm			t	$17.5\,\mu$m

Transition, Coupler, and Antennas

Probe-station measurements require that the input and output port (even in the case of a radiator) are on the same side of the substrate and that probed ports terminate in a CPW transmission line. This necessitates the use of multiple transitions to measure the various unit-cell components. The design of novel testing circuitry, as well as unit-cell components used in the final implementation of the array are presented below.

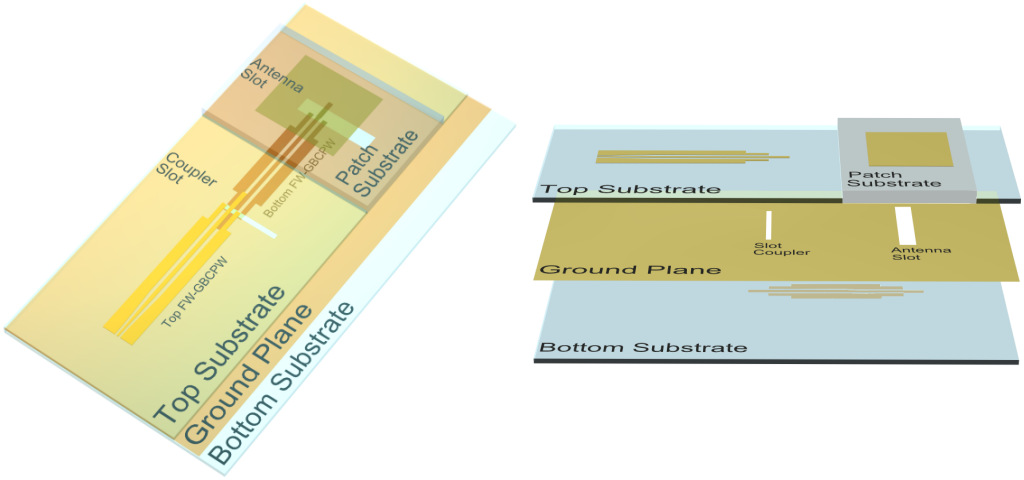

(a) (b)

Figure 6.3: *K*-band ground-backed CPW balanced coupler with the transition-fed patch antenna shown in perspective (a) and in the form of an assembly drawing (b). The circuits are uniplanar in design and do not require vias or airbridges. Signals are coupled electromagnetically through the slots in the shared ground plane.

Table 6.3: Dimensions of the slot coupler and antennas.

Coupler Dimensions		Slot Dimensions		Slot-Fed Patch Dimensions	
l_{sc}	3.57 mm	l_{sa}	4.67 mm	l_p	6.56 mm
w_{sc}	0.38 mm	w_{sa}	1.20 mm	w_p	5.99 mm
				h_p	1.00 mm

Uniplanar circuit elements recently developed for CMMICs on either finite-ground CPW (FGCPW) or fCPW are filters [64], lumped elements [65] and multipliers [66]. The balanced fCPW-to-fCPW transition presented in below is an extension to the recently developed fCPW-to-MSL [67] and

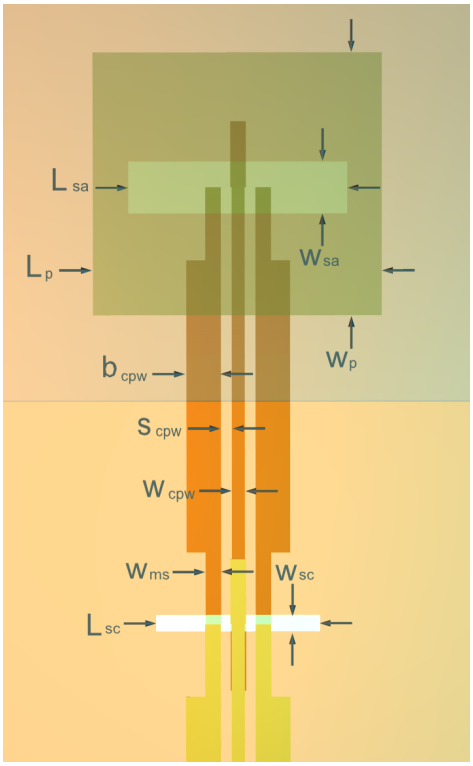

Figure 6.4: Balanced coupler and patch antenna with characteristic geometric parameters labeled.

FGCPW-to-FGCPW transitions [68].

The design of the coupler and antennas is performed by starting from zero-order physical-reasoning and optimizing the design using the commercial full-wave simulation tool *IE3D* [50]. The slot coupler is comprised of two fCPW-to-MSL transitions aligned on opposite sides of a slot in a shared substrate ground plane. The coupler transition can be seen in Figure 6.3 as the transition before the patch antenna. The transition from fCPW to MSL occurs in three coupled microstrip transmission lines. The transition

lengths are approximately $\lambda_{\mathrm{ms}}/4$ at the center frequency of operation ($f_0 = 19\,\mathrm{GHz}$), where λ_{ms} is the guided wavelength of the three-conductor (MSL) lines [67]. The slot in the substrate ground is centered between the interface of the three $\lambda_{\mathrm{ms}}/4$ coupled MSL sections and the single $\lambda_{\mathrm{ms}}/4$ MSL.

The two antennas in a unit cell are a standard microstrip-fed patch antenna and a slot-fed patch antenna. The standard microstrip-fed patch antenna uses an offset feed placed on the non-radiating edge [69]. The slot-fed patch combines the transition described above with a coupler optimized as a feed for a parasitic patch. This method differs from the one presented in [70], in that the transition is combined with the radiating slot to reduce space consumption.

To avoid the low radiation efficiency typical of microstrip antennas fabricated on thin, high-permittivity substrates, the patch antenna is placed on a low-permittivity dielectric above the slot. The dielectric is Rohacell 31 HF with a thickness of 1 mm, a relative permittivity of $\epsilon_r = 1.07$, and a loss tangent of $\tan\delta = 0.0036$ at the design frequency. Simulations place the front-to-back ratio of the slot-fed patch at 36 dB. The dimensions of the transmission lines, slot couplers, and antennas are summarized in Table 6.3.

Although the high front-to-back ratio for input-output isolation is the primary reason for using the slot-fed patch antenna, the increase in gain provided by the thick, low-permittivity substrate significantly improves the aperture efficiency of the array (Chapter 6.1.6 on page 104). The large slot-fed patch also has a larger bandwidth than the standard patch antenna which

prevents a frequency mismatch when cascading the various bandpass microwave components of the unit cell. This design achieves high isolation between feed and non-feed sides without the use of difficult-to-implement vias and coax transitions.

6.1.4 Element and Channel Coupling

Table 6.4: Simulated coupling between channels in the passive array.

Coupling Path	Side	Freq (GHz)	Coupling (dB)
$\mathbf{PA_{19}} \Rightarrow \mathrm{LNA}_{19}$	Non-Feed	19	**-50**
$\mathrm{PA}_{21} \Rightarrow \mathbf{LNA_{21}}$	Non-Feed	21	**-42**
$\mathrm{LNA}_{19} \Rightarrow \mathbf{PA_{19}}$	Feed	19	-29
$\mathbf{LNA_{21}} \Rightarrow \mathrm{PA}_{21}$	Feed	21	-21

Simulated channel coupling is shown in Table 6.4. Isolation between channels is provided by the use of band-pass components such as frequency-dependent transitions, couplers, and antennas. Additional isolation is furnished by the orthogonal polarization between the unit cells of opposite channels. The reduction of intrachannel coupling, the coupling from input to output antenna, enhances unit-cell stability. The reduction is achieved by the use of orthogonal polarizations for the input and output antennas, and by a ground plane, which separates the input and output antennas. Thus, the only antennas which are copolarized are antennas of the other channel on the opposite side of the ground plane.

6.1.5 Unit-Cell

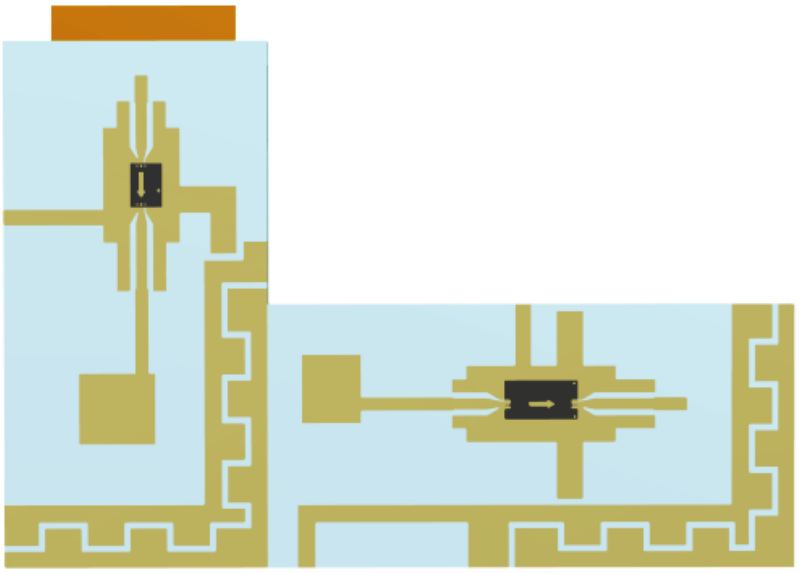

Figure 6.5: The 19-GHz transmit (*left*) and 21-GHz receive (*right*) unit cells as seen from the feed side.

Table 6.5: Antenna aperture-efficiency calculations.

	Transmit Channel 19 GHz		Receive Channel 21 GHz	
	Standard Patch	Slot-Fed Patch	Standard Patch	Slot-Fed Patch
λ	15.789 mm	15.789 mm	14.286 mm	14.286 mm
D_0	6.15 dB	9.06 dB	6.15 dB	9.06 dB
A_{eff}	81.8×10^{-6} m^2	159.8×10^{-6} m^2	66.9×10^{-6} m^2	130.8×10^{-6} m^2
A_{phys}	289×10^{-6} m^2	289×10^{-6} m^2	289×10^{-6} m^2	289×10^{-6} m^2
η_a	-5.48 dB	-2.57 dB	-6.35 dB	-3.44 dB

A single full-duplex transmit-receive unit cell is comprised of two indepen-

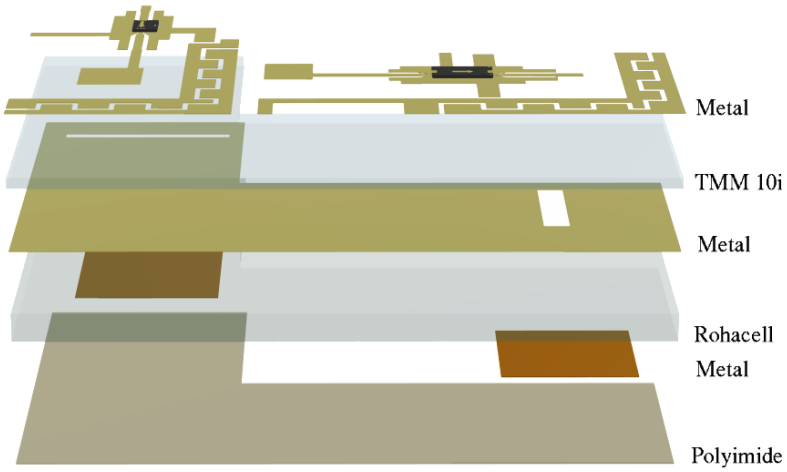

Figure 6.6: Assembly drawing of the transmit and receive unit cells. Substrates are shown partially transparent for clarity.

dent orthogonal unit cells, one for each channel (Figure 6.5). A single channel's unit cell contains a patch antenna, a coplanar waveguide section with amplifier, and a slot-fed patch antenna. A unit cell measures $8.5 \times 17\,\text{mm}$ ($0.538 \times 1.077\,\lambda_{19\,\text{GHz}}$ or $0.595 \times 1.190\,\lambda_{21\,\text{GHz}}$). By rotating the array 45° clockwise, it can be seen that the unit cells create a regular rectangular lattice $\sqrt{2} \times 8.5\,\text{mm}$ by $2\sqrt{2} \times 8.5\,\text{mm}$ in size. This rotated rectangular spacing is $12\,\text{mm} \times 24\,\text{mm}$ ($0.761 \times 1.522\lambda_{19\,\text{GHz}}$ or $(0.842 \times 1.628\lambda_{21\,\text{GHz}}$).

The full-duplex transmit-receive array is designed using uniplanar multilayer processing eliminating vias and air bridges. This is achieved by integrating microstrip line (MSL) and finite-width ground-backed coplanar waveguide (fCPW) within a single unit cell (Figure 6.6). The MSL provides the connection to the standard patch antenna on the feed side of the array; the

fCPW provides a transition to the MMIC, which eliminates the need for vias required with MSL. Transitions between MSL and fCPW occurs in a section of three coupled microstrip transmission lines of length $\lambda_{\text{ms}}/4$ at the unit-cell's frequency of operation [71].

This transition feeds the slot-fed patch antenna on rigid foam through a slot in the ground plane on the opposite side of the MMIC. The integrated slot-transition feed reduces space consumption and improves the front-to-back ratio (36 dB) of the slot-fed patch relative to a standard MSL feed. Additionally, the slot-fed patch antenna is polarized orthogonally to the microstrip-fed patch antenna eliminating the need for a 90° bend in the unit-cell line. The number of air bridges is minimized by keeping the transmission lines straight. Coupling simulations are performed with Zeland *IE3D* and predict the level of channel isolation between the PA and LNA to be -42 dB at 21 GHz. Results of the simulations are summarized in Table 6.4. The first row in the table indicates in bold the critical coupling that leads to a transmit signal adding noise to the receiver.

The aperture efficiencies of the unit cells are summarized in Table 6.5. The aperture efficiencies are calculated with Equation 2.1 on page 16 using the area of two unit cells as A_{phys}. It should be noted that the aperture efficiency of the array is most strongly influenced by the array's overall array factor rather than by the individual unit cell, but is included here to highlight the relative directivities of the antennas.

6.1.6 Array Layout

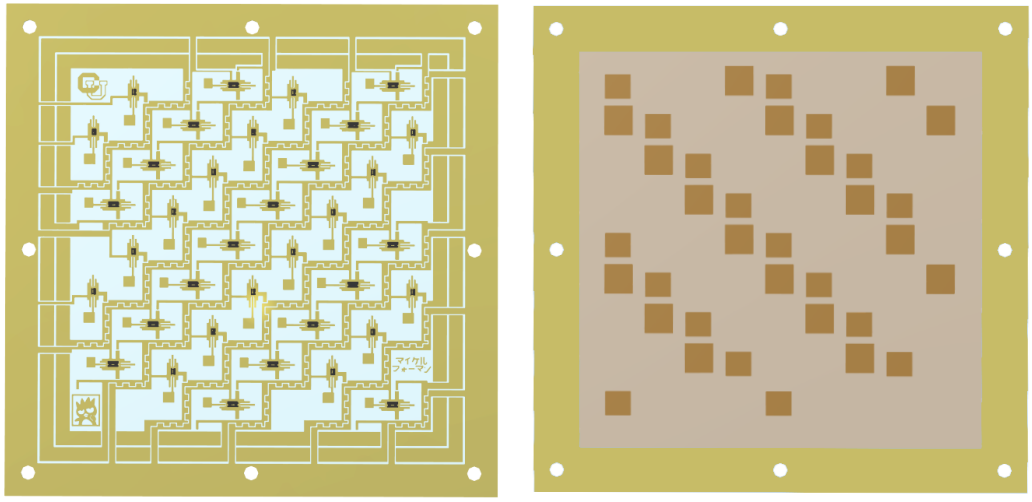

(a) (b)

Figure 6.7: The *K*-band full-duplex transmit-receive active-antenna array shown from the feed side (a) and non-feed side (b). Antennas on the feed side replace a corporate feed, while the non-feed side contains the main radiators.

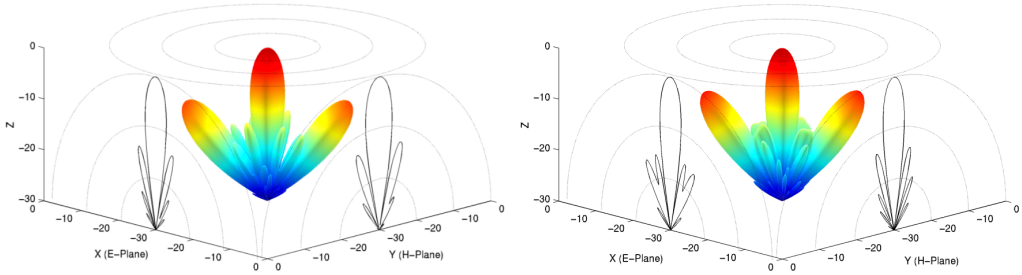

(a) (b)

Figure 6.8: Simulated array pattern at 19 GHz (a) and 21 GHz (b).

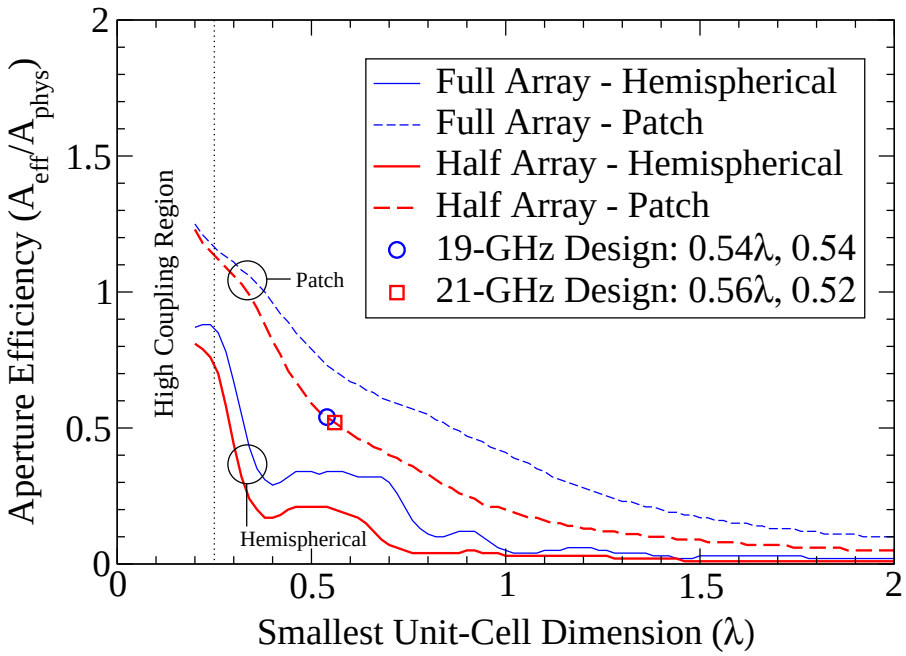

Figure 6.9: Aperture efficiency versus the smallest unit-cell dimension for the transmit-receive active-antenna array.

There are 18 transmitting and 18 receiving unit cells arranged in alternating diagonal rows (Figure 6.7). The distance between neighboring antennas on the non-feed side for a given frequency is $12 \times 24\,\text{mm}$ ($0.76 \times 1.52\,\lambda_{19\,\text{GHz}}$ or $0.84 \times 1.68\,\lambda_{21\,\text{GHz}}$). This spacing generates grating lobes at 39° and 35° at 19 GHz and 21 GHz in the diagonal plane corresponding to the largest row separation. Equivalently, a single transmitter in the far field generates three maxima on the focal plane with similar angular separation. In communi-

Table 6.6: Array aperture-efficiency calculations for different array topographies. The fabricated array is shown in bold.

Array Topography		Transmit Channel 19 GHz		Receive Channel 21 GHz	
Array	Antenna	Array Directivity D_0 (dB)	Aperture Efficiency η_a	Array Directivity D_0 (dB)	Aperture Efficiency η_a
Full Array	Patch	25.3	0.73	25.5	0.71
Half Array	**Patch**	**23.9**	**0.54**	**24.1**	**0.52**
Full Array	Hemi	21.9	0.34	22.3	0.34
Half Array	Hemi	19.8	0.21	20.1	0.20

cation applications, the aliasing of the main-beam can be used to increase received and transmitted power by employing multiple receivers or transmitters at the focal plane. Additional receivers may also be used to to improve angular diversity [32].

Aperture efficiency as a function of the smallest unit-cell dimension (a unit cell has a 2:1 length-to-width ratio) is shown in Figure 6.9. If the array were converted to a unidirectional array populated with a single unit cell of a given frequency, the aperture efficiency would be 0.73 at 19 GHz and 0.71 at 21 GHz. The aperture efficiency for the full-duplex array is 0.54 at 19 GHz and 0.52 at 21 GHz. Due to the high gain of the slot-fed patch antennas, the effect of the grating lobes on aperture efficiency is reduced relative to the simulation based on a 10×10 array of Hertzian dipoles (Figure 2.2 on page 18). The net change is a drop in aperture efficiency of 0.19 at 19 and 21 GHz. Simulated directivities and aperture efficiencies are summarized in

Table 6.6.

Bias Lines

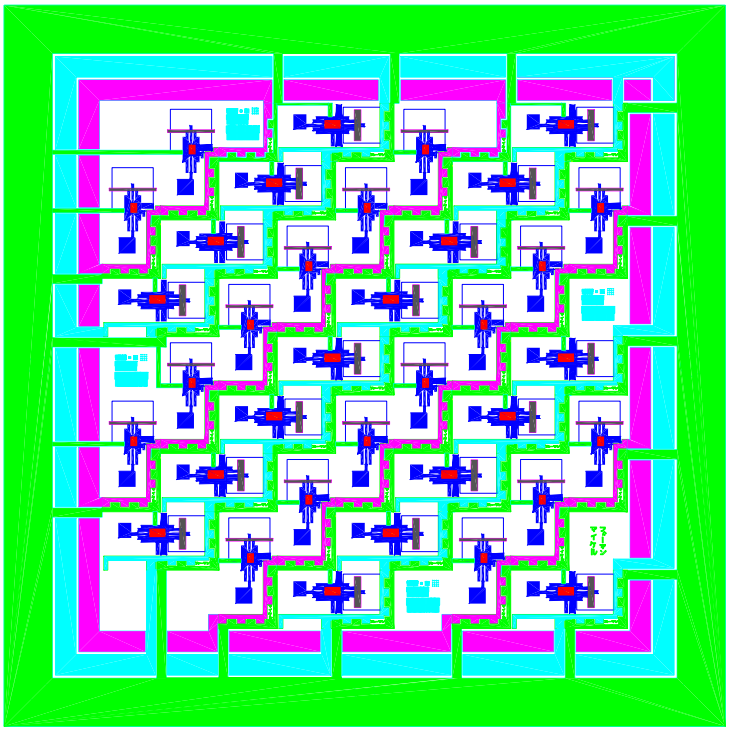

Figure 6.10: Schematic of the transmit-receive active-antenna array with different bias lines highlighted. The outer bias ring is the ground, the middle ring powers the LNAs, and the center ring powers the PAs.

Bias lines in the array are designed to prevent DC-voltage variations while simultaneously attenuating RF. Variations are minimized by encircling the array with wide, low-resistance bias lines and connecting each row from both the top and bottom. This minimizes the parallel-parallel voltage drops seen in the *Ka*-band array (Chapter 3.1.4 on page 37).

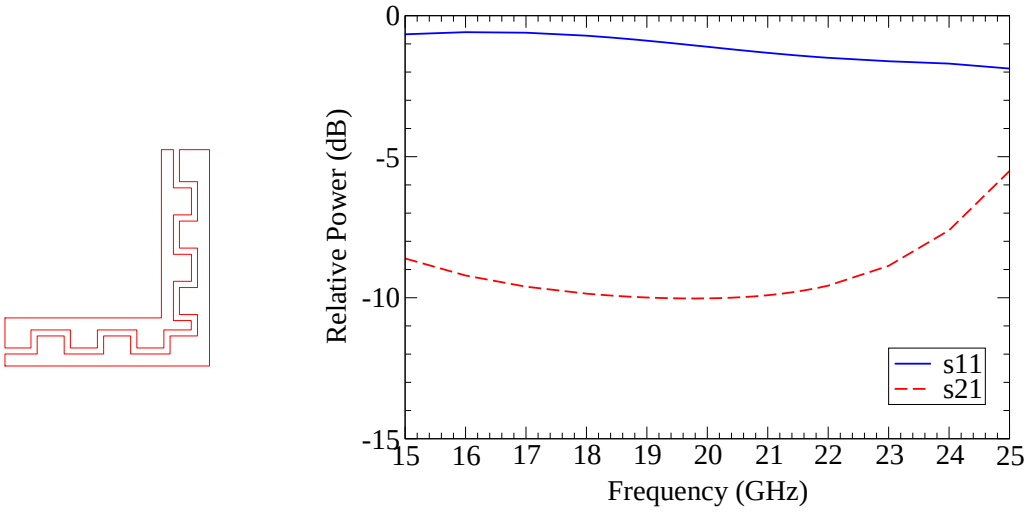

(a) (b)

Figure 6.11: Unit-cell bias-line segment (a) and its simulated frequency response (b).

Two bias lines and a shared ground line are required to supply voltage to the two devices. Figure 6.10 highlights the ground line, the PA bias line, and the LNA bias line. Identical unit cells are designed in such a way that when they are arrayed, a continuous bias line is automatically created. Additionally, the unit-cell bias lines for each channel are designed together, such that a 19-GHz unit cell holds the bias line for itself and the ground line for the adjacent 21-GHz unit cell. The bias lines crossing the array are designed as interdigitated filters (Figure 6.11(a)). The filters provide 10 dB of insertion loss over a unit-cell length at 20 GHz (Figure 6.11(b)).

Lens

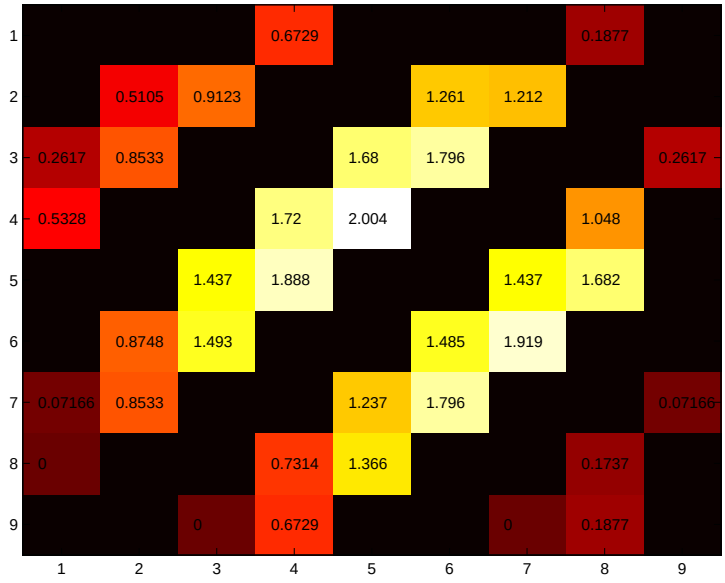

Figure 6.12: Matlab output for the iterative solution of the delay lines. The graph represents the surface of the array with the axes counting unit cell halves across the face. The delay lines are implemented by increasing the length of the MSL feeding the standard patch antenna. Numbers are delay-line lengths in millimeters.

The theory of constrained lenses, demonstrated for passive lens arrays [72, 73, 74], is applicable to active-antenna arrays. The first constrained lens antenna, known as the *Bootlace* aerial, was developed in 1957 by Gent [75]. This passive lens consisted of two planes of dipole antennas separated by a ground plane and connected electrically by transmission lines. The lengths of transmission line were chosen such that an incident spherical wave from a near-field feed of a predetermined distance would radiate as a collimated

beam on the opposite side. This lens demonstrated the solution of path-length equality conditions for a one degree-of-freedom lens [76]. It is possible to add additional degrees of freedom to the design of a lens to solve for additional focal points. Each degree of freedom yields an additional unique focal point.

It was McGrath in 1986 who first suggested the planar constrained lens using microstrip transmission lines [72]. As with the work done by Gent, it was shown that a one-degree-of-freedom lens can be created by two identical input and output antenna arrays joined by microstrip delay-line lengths. The equation which solve for the delay line lengths given a single focal point on the optical axis at a distance f behind a lens of diameter d is given by

$$L_n = \sqrt{f^2 + \left(\frac{d}{2}\right)^2} - \sqrt{f^2 + r_n^2} \tag{6.10}$$

where r_n is the radius from the center of the lens to element n [77].

In the full-duplex transmit-receive array, a one-degree-of-freedom true-time delay array lens [56] with a focal distance of 166.5 mm and a diagonal aperture length of 90 mm ($f/d = 1.85$) is implemented. Lensing is provided by the variation of the microstrip standard-patch feed-line lengths resulting in the change of antenna placement relative to the regular array spacing on the feed-side of the array. The change in position of the antenna due to delay-line variations requires the use of an iterative code to calculate the antenna element positions. The solutions found in Matlab [78] are shown in Figure 6.12 in millimeters of delay-line lengths for both unit-cell frequencies.

Because the lengths are frequency and substrate dependent, the code directly converts electrical length delay into millimeters for each frequency.

6.2 Fabrication

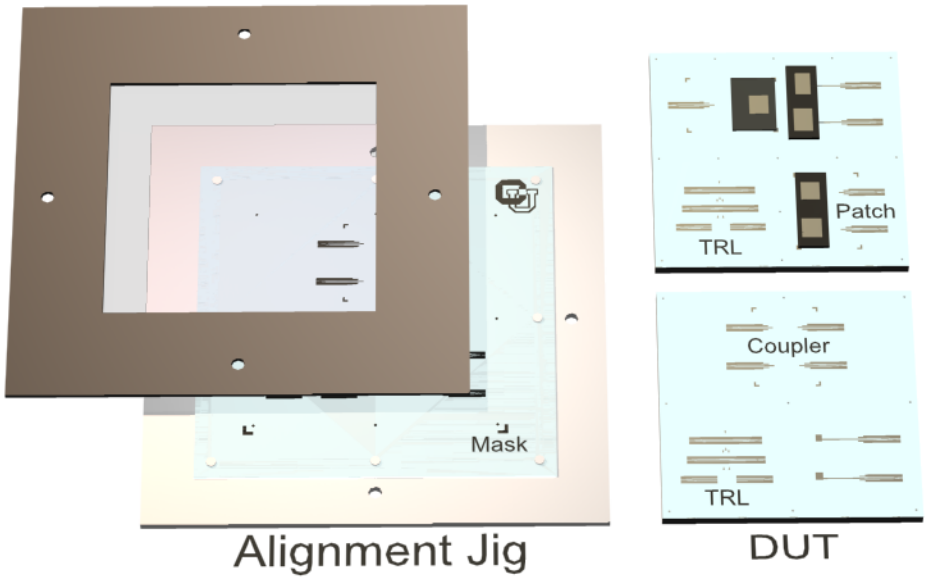

Figure 6.13: The alignment holder is shown on the left with a substrate blank and mask on the alignment pins. The assembled multilayer circuits are shown on the right with the coupler, patch antenna, and TRL calibration set labeled.

A new fabrication technique enhances repeatability and accuracy. The new process is based upon the process developed for the *Ka*-band antenna arrays. In the design no vias or coax are used, there are no 90-degree bends, fabrication is strictly uniplanar, and wire bonds have been eliminated, with the exception of the bonds required for the MMIC.

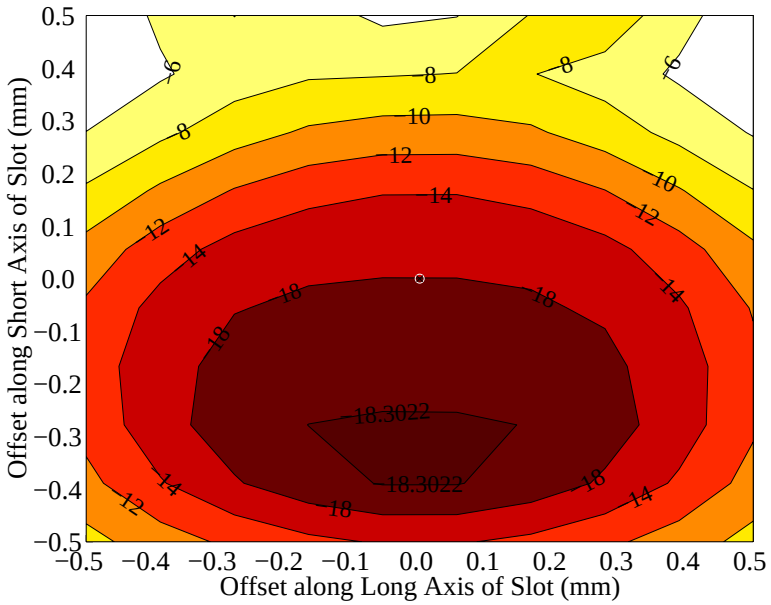

Figure 6.14: Sensitivity analysis with respect to transition-to-slot misalignment along both axes. The contour plots show values of s_{11} in dB at 19 GHz.

Fabrication is performed in multiple photolithographic steps on both faces of the *TMM 10i* for the circuits and slots and on *Novaclad G2300* for the slot-fed patch antennas. Some test circuits require a milling step to remove substrate after photolithography and etching. Unlike the single-layered fabrication process used with the *Ka*-band array, the multilayered design of the array necessitates a different approach. In order to achieve the alignment requirements with available equipment, a single alignment holder capable of carrying the substrate through all steps of fabrication has been designed (Figure 6.13). The holder is a 5-mm thick block of aluminum with eight raised pins on the top, nine pins on the bottom, and four threaded holes.

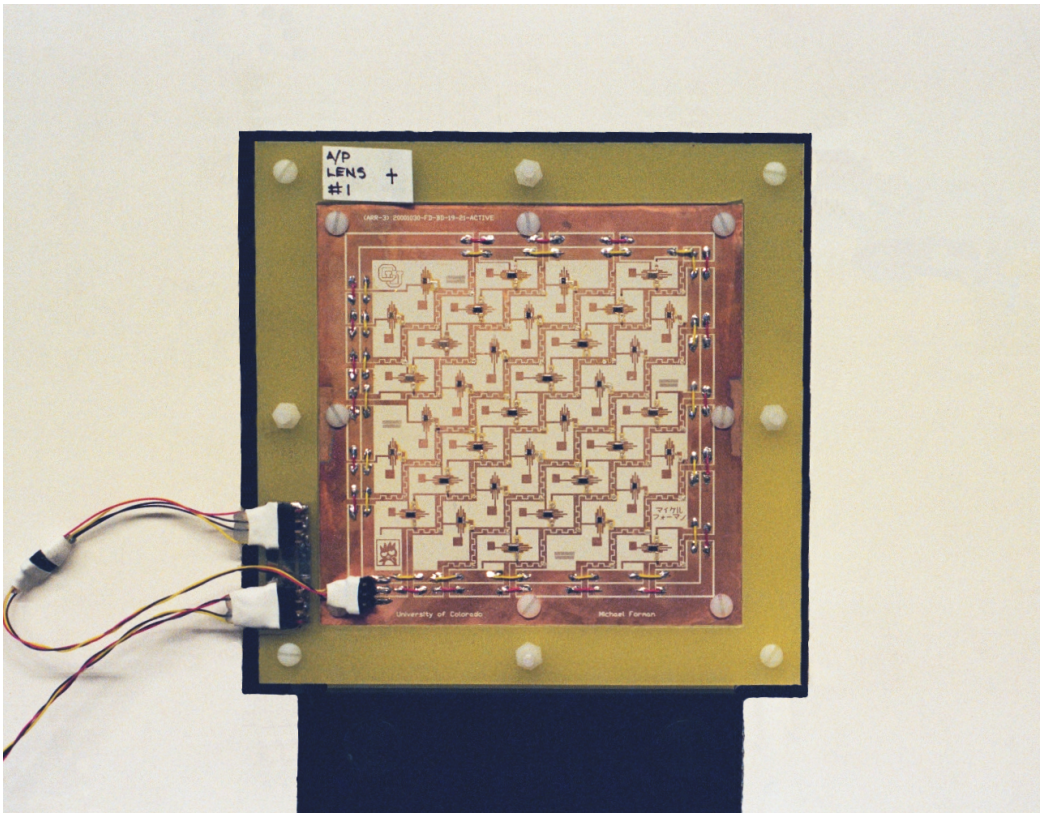

Figure 6.15: Picture of the fabricated full-duplex transmit-receive array.

Repeatably accurate photolithography between different substrates and substrate sides is possible by a combination of the holder, predrilled substrates, and precut masks. Predrilled squares of substrate, referred to as *blanks*, are milled out on an *LPKF* ProtoMat 93s milling machine such that they tightly mate with the eight pins on the holder. In a separate step a mylar mask is aligned to an FR4 frame with eight holes matching the alignment pins on the holder. After careful visual alignment, the eight holes in

the FR4 are used as a guide to drill holes in the mylar mask. By predrilling holes in both the substrate and mask, substrates can be aligned repeatably and quickly in the clean room.

After the application of photoresist, and completion of the pre-bake step, the substrate and mask are placed on the holder over the alignment pins. A square glass plate attached to an FR4 frame is screwed down on top of the holder by means of the threaded holes to provide a pressure fit. The nine pins on the bottom of the holder allow repeatable mating with a milling machine. It is possible to use the holder to machine a substrate, perform photolithography, and again machine the substrate with high repeatability.

The addition of a group of thin metallic lines to the array face provides a mechanism to monitor the progress of the chemical etching step. The 12.5, 25, and 50-μm lines are grouped into several small squares on the periphery of the array. Upon the disappearance of the 25 μm lines, the designed amount of overetch is reached signifying the completion of the etching stage.

The alignment and etching enhancements have improved photolithographic processing accuracy and repeatability. Accuracies between different substrates or substrate sides have been measured to be $\pm 50\,\mu$m. Alignment accuracies between photolithographic processing and mechanical milling have been measured at $\pm 75\,\mu$m. Simulations show that transition-to-slot alignment must be within $\pm 200\,\mu$m to ensure good insertion loss (Figure 6.14). The slot-to-patch alignment is more forgiving, allowing a simulated and experimentally verified tolerance of $\pm 600\,\mu$m.

The remaining fabrication steps, such as chip bonding and wirebonding, are identical to the steps described in Chapter 3.2. A photograph of the completed active-antenna array is shown in Figure 6.15.

Chapter 7

K-Band Transmit-Receive Array Measurement and Analysis

7.1 Amplifier-Array Measurement

The following work contains the full characterization of the K-band full-duplex transmit-receive active-amplifier array. Section 7.1.1 presents measurements of the intra-unit-cell elements such as fCPW-to-MSL transitions, couplers, and antennas. Small-signal gain results are presented for the lens feed in Section 7.1.2. Saturated power measurements are discussed in Section 7.1.3 followed by pattern measurements of the passive and active arrays in Section 7.1.5. Section 7.1.4 contains thermal measurements.

7.1.1 Elements of the Array

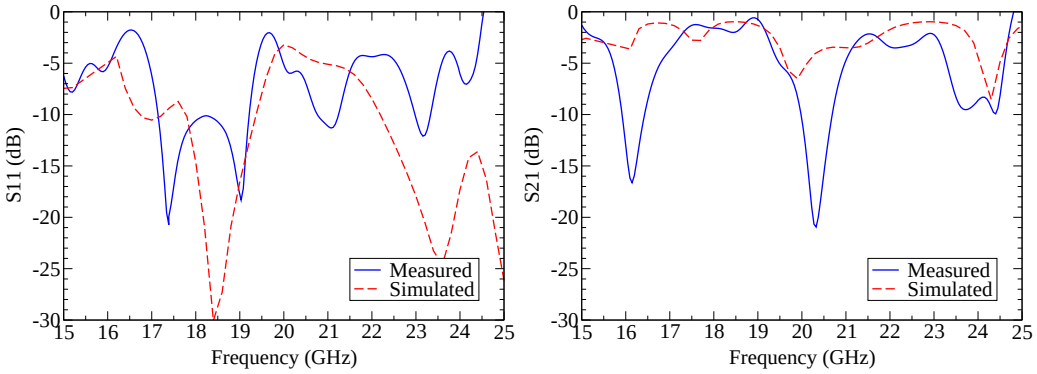

(a) (b)

Figure 7.1: Measured and simulated reflection (a) and transmission (b) coefficients of the slot coupler.

The elements of the array are fabricated individually on separate substrates and are measured using an HP 8510 network analyzer and a *Cascade Microtech* Analytical Probe Station 9000 with two *Cascade Microtech* ACP50 ground-signal-ground (GSG) CPW probes with 250 μm pitch. The measurements are calibrated with respect to a TRL calibration fabricated on the same substrate as the DUT.

Because the slot-coupler transition is used to feed the slot-fed patch antenna, it is the first circuit characterized. The measured performance of the transition is compared with the *IE3D* method-of-moment (MOM) simulation in Figure 7.1. The measured return loss of the coupler is less than 10 dB over a 12% bandwidth from 17.1 to 19.2 GHz with a 2 dB average in-

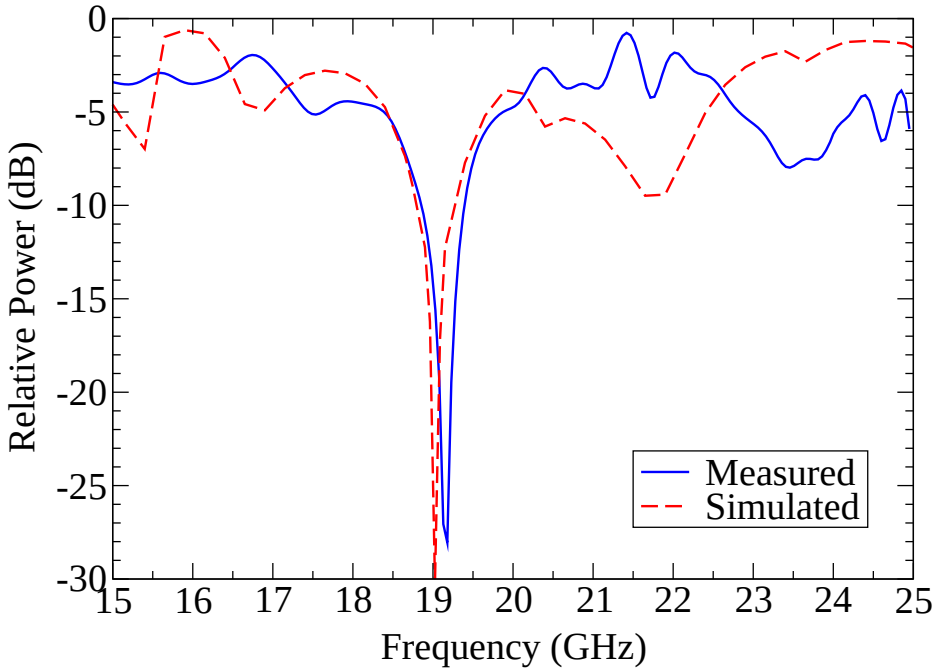

Figure 7.2: Measured and simulated reflection coefficient versus frequency of the slot-fed patch antenna.

sertion loss over the pass band. Because the DUT is measured on the surface with probes, two slot couplers are connected and measured in series. The measured coupler is shown and labeled in Figure 6.3 on page 97.

The performance of the transition-fed patch antennas is shown in Figure 7.2. The measured bandwidth of the patch antenna is 3.1% with a simulated efficiency of 80% and directivity of 9.2 dB. The front-to-back ratio is 26 dB. The measured and simulated center frequencies agree within 1%.

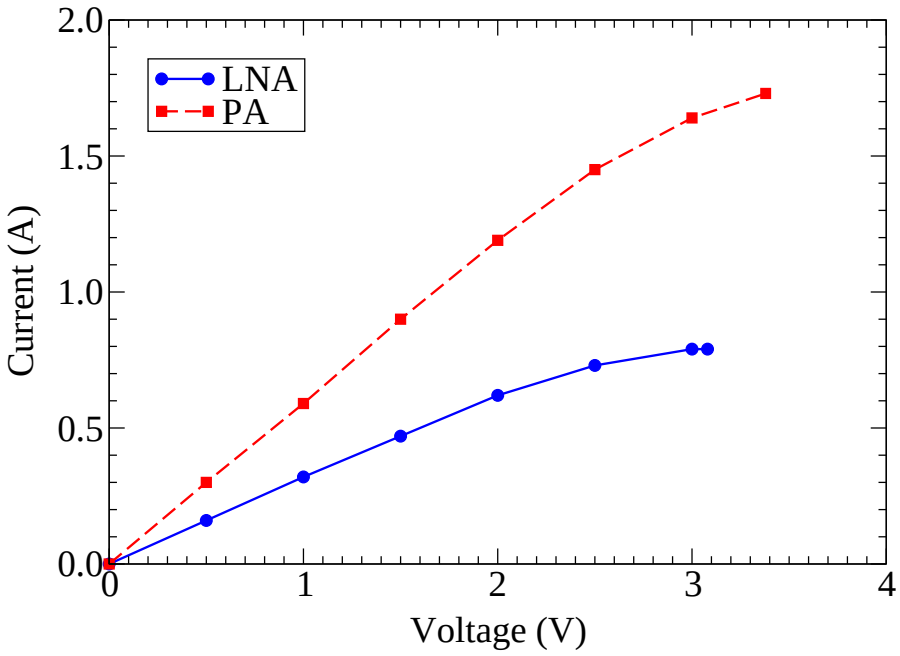

Figure 7.3: Bias characteristics for the LNA and PA.

Results for the 21 GHz circuits show similar agreement.

7.1.2 Small-Signal Gain

The array is placed 17 cm from a 5.3-dB 10.5×4-mm radiating waveguide aperture and 100 cm from a 20.8-dB standard pyramidal horn in the far field. Small-signal measurements are performed with an HP 8510C vector network analyzer and are normalized to a free-space calibration performed through an array-sized aperture.

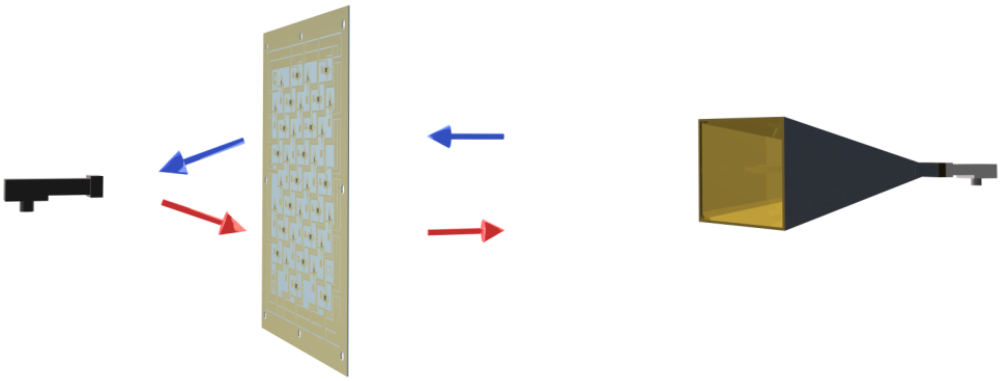

Figure 7.4: Measurement setup for the transmit-receive array showing the near-field waveguide aperture on the left and the standard pyramidal horn on the right.

Passive antenna measurements are shown in Figure 7.5. The transmit and receive channels have a gain of -12.9 dB at 18.9 GHz and -11.2 dB at 21.1 GHz respectively. Measured center frequencies are within a fraction of a percent from the simulated ones.

Active small-signal gain measurements are performed in half-duplex mode. Only a single channel is on at a given time. The transmit and receive half-duplex small-signal active measurements are shown in Figure 7.7 and Figure 7.6 respectively and summarized in Table 7.1. The transmit array channel provides -9.9 dB of gain at 18.9 GHz which is 3.0 dB above the passive array at 3.38 V and 1.73 A. The receive channel provides -2.9 dB of gain at 21.1 GHz with a 8.2 dB gain above the passive array at 3.08 V and 0.79 A. The active half-duplex measurements are shown in Figure 7.8 together with the passive array.

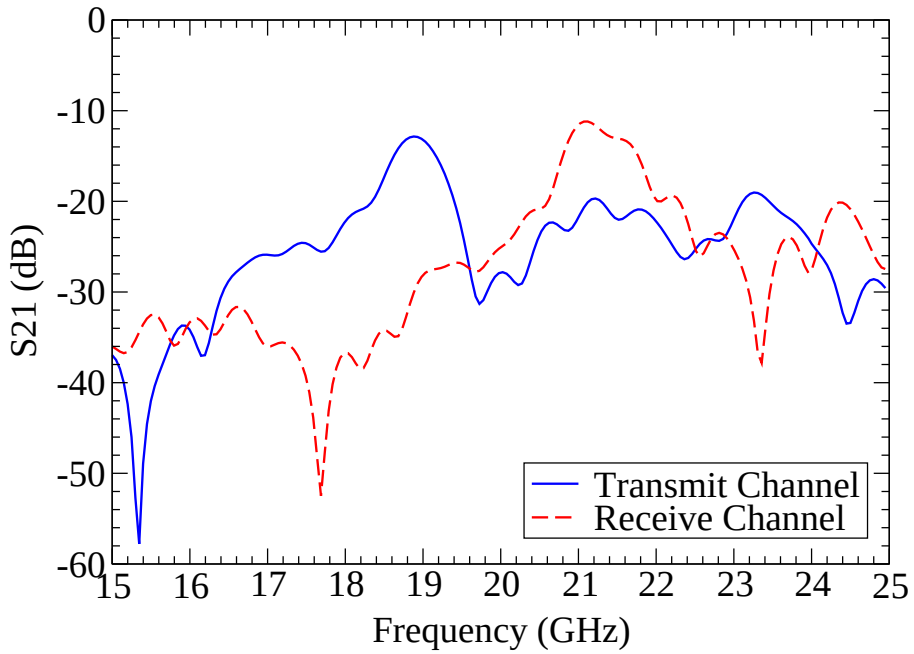

Figure 7.5: Measurement of the passive array showing transmission response through the array as a function of frequency.

Active small-signal full-duplex measurements are presented in Figure 7.9. Both channels are stable with little or no effect on the performance of the other channel. The transmit array channel provides -9.9 dB of gain at 18.9 GHz which is 3.0 dB above the passive array at 3.55 V and 1.73 A. The receive channel provides -3.7 dB of gain at 21.1 GHz with a 7.4 dB gain above the passive array at 4.00 V and 0.84 A. The presence or absence of bias to one channel has no effect on the gain of the opposing channel within the error

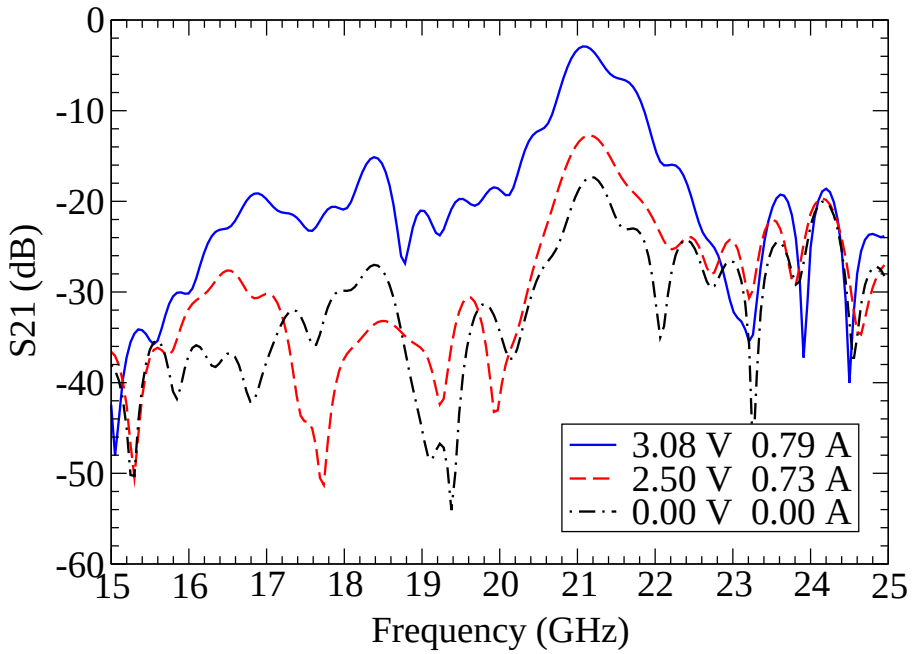

Figure 7.6: Measurement of the active array for the 21 GHz LNA channel showing transmission response through the array as a function of frequency.

of measurement. The difference in bias level between half- and full-duplex modes is attributed to gain suppression due to the increased temperature during full-duplex operation. A comparison between the half-duplex and full-duplex gain measurements is shown in Figure 7.10. The receive channel shows a change of 0.8 dB at 21 GHz, with out-of-band gain growing in places by 10 dB.

Note that the difference in gain between the transmit and receive channel

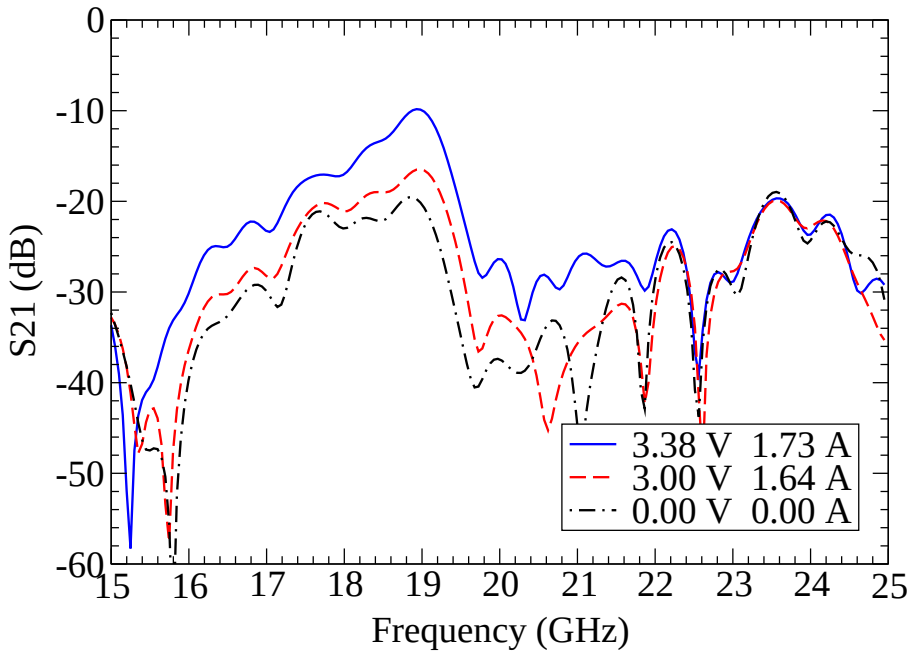

Figure 7.7: Measurement of the active array for the 19 GHz PA channel showing transmission response through the array as a function of frequency.

at the receive channel's frequency of operation is separated by 24 dB. This isolation is critical to prevent the transmit channel from amplifying noise at the LNA's operation frequency.

The maximum gain of the MMICs are limited by oscillations. The bias levels at which oscillations occur in one MMIC are unaffected by the bias level or state of the other MMIC. Evidence supports that the oscillations occur at the devices themselves and are most likely due to an impedance

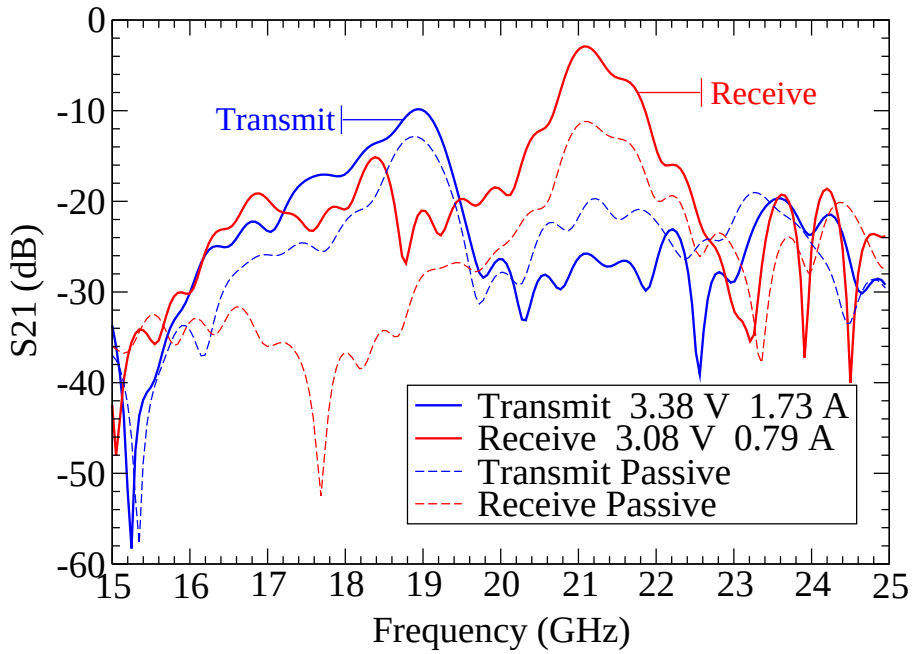

Figure 7.8: Measurement of the passive and active array showing transmission response through the array as a function of frequency.

mismatch presented to the amplifier by wirebond inductance or the wirebond-transmission interface.

7.1.3 Saturated Power

The saturated output power of the arrays is calculated by dividing the EIRP by the estimated gain of the array. A value of 18.75 dB for the array gain is obtained by direct measurement of the passive antenna. Figure 7.11 shows

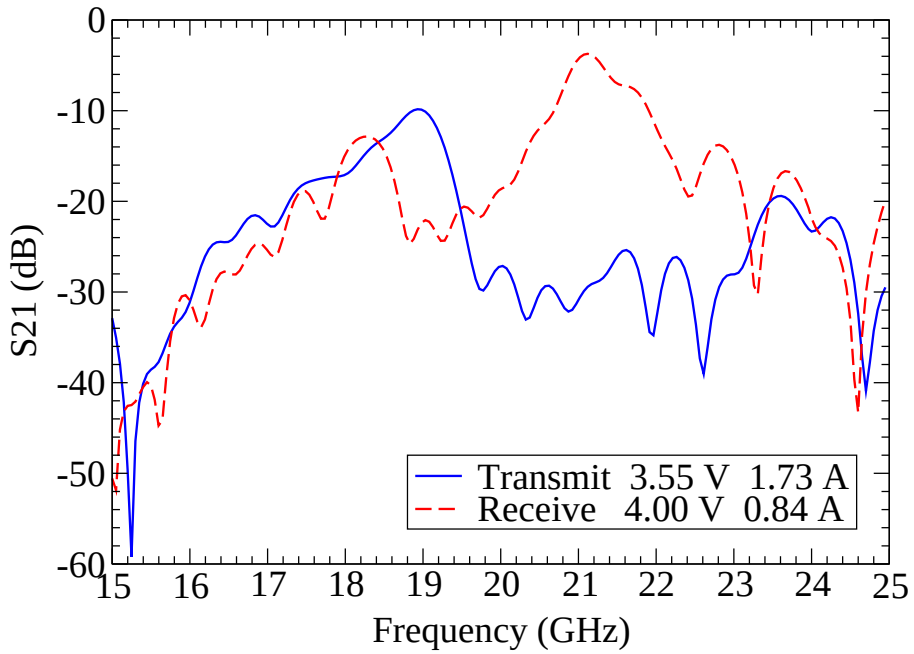

Figure 7.9: Measurement of the active array operating in full-duplex showing transmission response through the array as a function of frequency.

the power at the output of the array as a function of the power present at the face of the array. Limitations imposed by MMIC instability prevent the acquisition of the maximum operating power. Maximum power out is measured to be 6 mW.

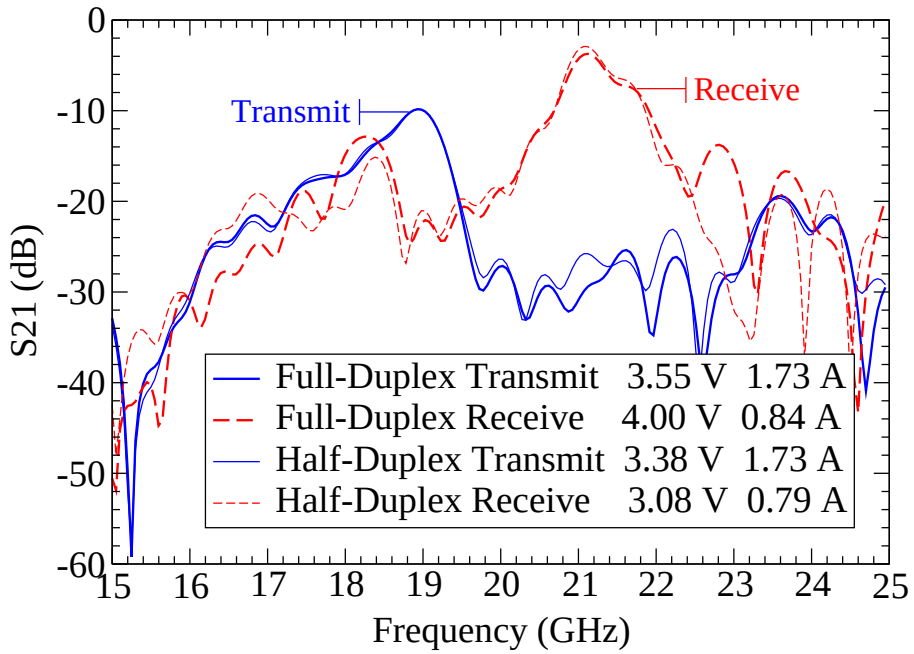

Figure 7.10: Comparison of the active array operating in half- and full-duplex mode showing transmission response through the array as a function of frequency.

7.1.4 Thermal

Figure 7.12 shows the maximum steady-state array temperature as a function of bias point for half-duplex and full-duplex operation. There is an approximately linear increase in steady-state temperature of 4°/W over the range of bias points. The thermal measurements are made with a *Raytek* Raynger PM40 infrared thermometer. The infrared thermometer requires a

Table 7.1: Transmit-receive array measurements.

Channel	Freq (GHz)	On/Off (dB)	Gain (dB)	G_a (dB)
Transmit	18.9	10.0	-9.9	3.0
Receive	21.1	15.0	-3.0	8.2

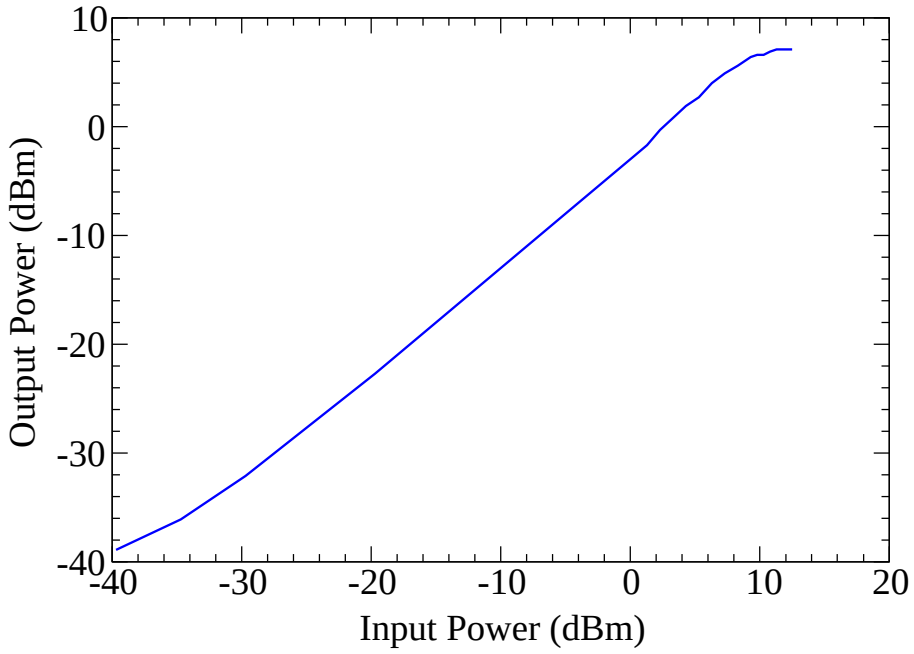

Figure 7.11: Output power at the face of the array versus input power at the face of the array.

value for the emissivity of the measured surface to provide accurate results. The emissivity setting on the IR thermometer is calibrated by measuring the array at a known temperature and setting the emissivity to give the proper

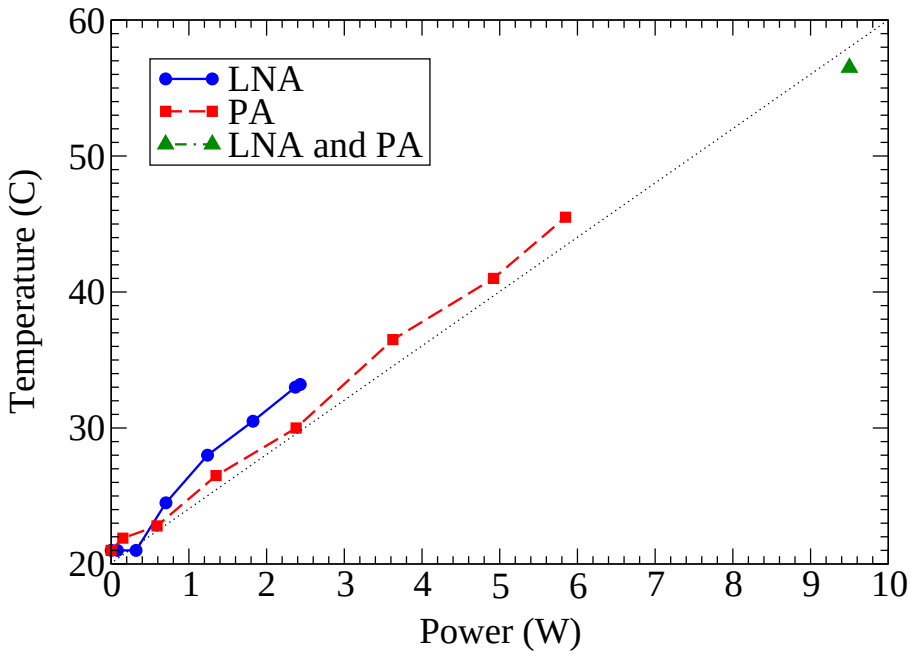

Figure 7.12: Maximum array temperature as a function of bias point.

temperature. Measurements are taken with a 1-m^3/min fan providing laminar forced-convective flow over the surface of the array from the underneath. The maximum temperature of 60°C is well below the maximum operating temperatures of 90°C for the LNA and 165°C for the PA.

7.1.5 Far-Field Patterns

Far-field patterns are taken at 19 GHz in transmission and at 21 GHz in reception. Figure 7.13 shows the measured passive patterns. Figure 7.14 shows the

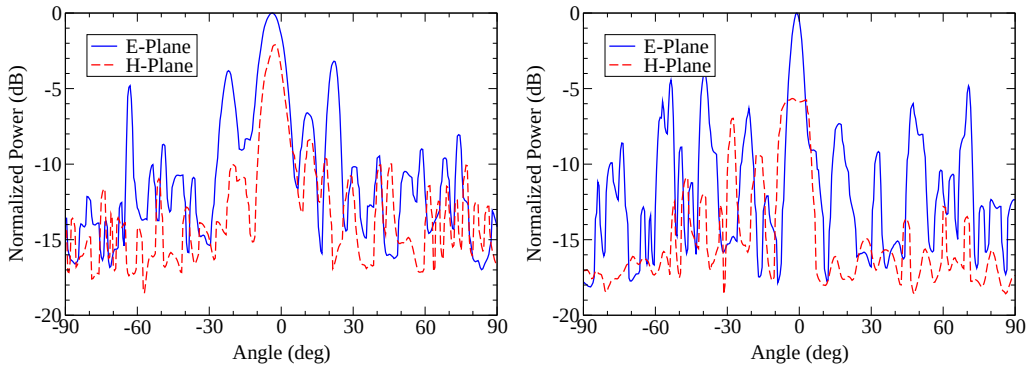

(a) (b)

Figure 7.13: Passive far-field E-plane and H-plane measurements at 19 GHz (a) and 21 GHz (b).

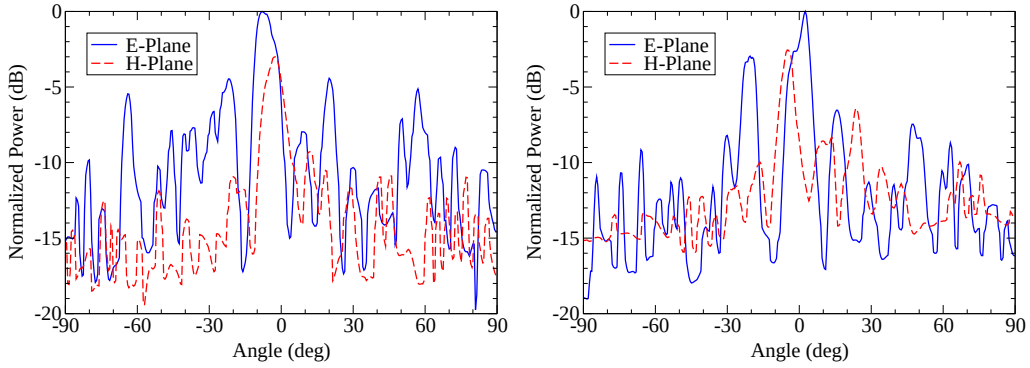

(a) (b)

Figure 7.14: Active far-field E-plane and H-plane measurements at 19 GHz for the PA at 19 GHz (a) and LNA at 21 GHz (b).

measured active patterns for the PA in transmission at 19 GHz and the LNA in reception at 21 GHz with the simulated patterns. The irregular patterns

are attributed to multi-path effects and cable discontinuities encountered in a new anechoic chamber.

7.2 Conclusions

The primary goal of demonstrating the first spatial power combiner to provide full-duplex transmit-receive functionality has been met. The secondary goals of preventing inter-channel coupling, and simplifying fabrication while improving repeatability have also been met.

Possible improvements in the near future would be to investigate the power amplifier oscillations. It may be possible to improve the output match by placing a inductive wire bond at the output of the MMIC from signal to ground. By tuning the distance between the wirebond and the MMIC stability, gain, and output power could be improved.

Chapter 8

Conclusions

8.1 Ka-Band Active-Antenna Amplifier Array

The fundamental goal of the first project presented in this thesis is to design, fabricate, and characterize a watt-level *Ka*-band spatial power combiner. The design not only requires experience in microwave engineering, but in thermodynamics, mechanical engineering, and optics as well. Fabrication tolerances further diversify the required knowledge base by necessitating the use of clean-room fabrication technology to create the arrays. Characterization is performed using a variety of measurement equipment including pyramidal horns, hard horns, gaussian feeds, and electro-optic systems at the University of Colorado, the University of Michigan, and the California Institute of Technology.

The maximum output power for the *Ka*-band arrays are 89 W EIRP and 316 mW of output power for Array A and 145 W EIRP and 513 mW of output power for Array B. Losses in the polarizers, variations in the bias point, and device stability limit the maximum output powers of the arrays. Given that there are 36 31-mW MMICs on the array, with 70% power combining efficiency and a 1.3 dB polarization loss, the maximum expected output power is 580 mW. The measured powers are close to their expected values, achieving the goal of watt-level power at 31 GHz with commercial MMICs. Several secondary goals, such as the reduction of the maximum steady-state operating temperature by the use of a substrate with high thermal conductivity, and the development of a chemical process to repeatably fabricate microwave circuitry have also been achieved.

The notable problems encountered over the course of design, fabrication, and testing have been bias variations, nonuniform illumination, and amplifier instability. Bias variations in the array are due to a voltage-divider network comprised of bias lines and MMICs. The only solution is to reduce the ohmic loss of the line by increasing its conductivity or cross-sectional area or raising the impedance of the MMIC. In the first case, bias line width is limited by real-estate constraints, and height by the thin metalization required by inexpensive uniplanar fabrication. Increasing MMIC impedance is possible with the addition of a resistive parallel load but only at the expense of efficiency and low temperature. Ultimately, the maximum size of an inexpensive active-antenna array is limited by constraints imposed by the bias line. Only

by moving to more complicated biasing structures can the area of an active antenna array be increased.

Nonuniform illumination reduces the output power of a spatial power combiner. The lower gain provided by the arrays when under test with the near-field hard horns is attributed to nonuniform illumination. The hard horns have a measured $\pm 10\,\mathrm{dB}$ variation in power and $\pm 90^{\circ}$ variation in phase. This is problematic given, that in actual use, a spatial power combiner will certainly be contained in a guiding structure. Future implementations should include practical methods for feeding and collecting power from the beginning.

Instabilities in high-gain active devices are to be expected when so many are packed into such a small area. Although the *Ka*-band active-antenna arrays utilized orthogonal polarization between input and output antennas to provide isolation, it is barely sufficient. As seen in the resonant mode measurements, slight changes in polarizer position or orientation can create feed-back paths which lead to oscillation or unstable behavior. An improvement employed by multilayer active arrays is the use of an isolating ground plane between input and output antennas. The faces are connected with slot couplers or coaxial cables and provide superior isolation. The ground plane also creates a method of heat removal which is not dependent on the substrate. This frees the engineer to select the best substrate for the application while benefiting from the high thermal conductivity and isolation provided by a ground plane.

8.2 K-Band Full-Duplex Transmit-Receive Array

The fundamental goal of the *K*-band transmit-receive array is to demonstrate stable full-duplex operation with high channel isolation. Secondary goals include the implementation of enhancements acquired from experience with the previous array, such as increased antenna isolation by means of a ground plane, simplified fabrication requirements by the elimination of vias and wire bonds, a more efficient feed designed into the array from the beginning, and a wider interdigitated bias line to prevent voltage variations and suppress RF.

The array transmits at 19 GHz and receives at 21 GHz, with a simulated isolation of 50 dB at 19 GHz and 42 dB at 21 GHz between channels. The measured gains of the active array are 3 dB and 8.2 dB above passive with an on-off ratio of 10 dB and 15 dB for transmit and receive modes respectively. A channel's stability is unaffected by the bias point or input power of the other channel. Small variations in gain are present in full-duplex mode versus half-duplex mode, but the changes are attributed to thermal variations in the substrate which affect MMIC gain. The goal of providing stable full-duplex operation has been met. A point of interest is that this is the first demonstration of a *full-duplex* transmit-receive active-antenna array.

The array is fabricated using a photolithographic process similar to the procedure used for the first array, but enhanced to provide superior accuracy

and repeatability. The new technique allows for the creation of accurately-aligned complex multilayer microwave circuitry. The complex microwave circuitry provides antennas which radiate unidirectionally, transitions which couple through slots to patches across three accurately aligned layers, and complicated transmission lines which eliminate all vias and airbridges. In short, the secondary goals have all been met.

Although all goals are met, no project would be complete without the presentation of its difficulties. The K-band full-duplex transmit-receive array suffers from low feed-efficiency, low aperture efficiency, and device oscillations. The integration of a planar lens into the active array is an attempt to include a practical method of feeding the array from the beginning. A waveguide aperture is used as feed at the focal point, but due to low directivity and a large focal distance, the spill-over loss is high. In future projects the feed should be designed to match the diameter and focal distance of the lens.

The aperture efficiency of the array is enhanced by the use of high-gain patch antennas on a low-permittivity substrate. It is believed that the 54% aperture efficiency can be further improved upon. The simplest way to increase the aperture efficiency is to reduce the size of the unit cell. An increase in aperture efficiency from 54% to 65% can be achieved by shrinking the unit cell by 10%. The current unit cell is fabricated with bias lines and safety zones around the antennas that are larger than necessary to ensure stability. Larger reductions in size are possible by redesigning the circuits for higher

permittivity substrates and smaller MMICs.

The amplifiers provide 8.2 dB and 3.0 dB of gain over the passive array for the low-noise and power amplifier respectively. The maximum gain over passive is limited by the bias point, above which oscillations occur. The origin of the oscillations is attributed to an impedance mismatch at the bond-wire-transmission-line interface at the output of each amplifier. It may be possible to reduce the oscillations with the use of MMICs with narrow-band gain only in the frequency range of the channel.

Bibliography

[1] Robert A. York, "Quasi-optical power combining," in *Active and Quasi-optical arrays for solid-state power combining*, Robert A. York and Zoya B. Popović, Eds., chapter 1. John Wiley, New York, 1997. 3, 13, 17, 80

[2] S. M. Sze, *Physics of Semiconductor Devices*, chapter 10, John Wiley, New York, 1981. 2

[3] J. C. Rautio, "An investigation of microstrip conductor loss," *IEEE Microwave Magazine*, pp. 60–67, Dec. 2000. 4

[4] J. Harvey, E. R. Brown, D. B. Rutledge, and R. A. York, "High-power transmitters," *Microwave Journal*, pp. 48–59, dec 2000. 4

[5] K. A. Lee, "A 32-GHz phased array transmit feed for spacecraft telecommunications," *TDA Progress Report 42-11*, vol. July–Sept, pp. 310–324, June 1992. 6

[6] M. F. Durkin, "35-GHz active aperature," *IEEE MTT-S International Microwave Symposium Digest*, pp. 425–427, 1981. 7

[7] D. McPherson, "Active phased arrays for millimeter wave communications applications," *Milcom 95 Conf. Record*, pp. 1061–1065, Nov. 1995. 7

[8] J. J. Sowers, D. J. Pritchard, A. E. White, W. Kong, O. S. A. Tang, D. R. Tanner, and K. Jablinskey, "A 36-w V-band solid state source," *IEEE Transactions on Microwave Theory and Techniques*, June 1999. 7

[9] J. T. Delisle, M. A. Gouker, and S. M. Duffy, "45-GHz MMIC power combining using a circuit-spatially combined array," *IEEE Microwave and Guided Wave Letters*, vol. 7, pp. 15–17, Jan. 1997. 7

[10] D. Staiman, M. E. Breese, and W. T. Patton, "New technique for combining solid-state sources," *IEEE Journal of Solid-State Circuits*, vol. SC-3, pp. 238–243, Sept. 1968. 7

[11] T. K. Wu, *Frequency Selective Surface and Grid Array*, chapter 1, John Wiley, New York, 1995. 7

[12] M. Kim, J. J. Rosenberg, R. P. Smith, R. M. Weikle II, J. B. Hacker, M. P. De Lisio, and D. B. Rutledge, "A grid amplifier," *IEEE Microwave and Guided Wave Letters*, vol. 1, no. 10, pp. 322–324, Nov. 1991. 8, 11

[13] M. Kim, E. A. Sovero, J. B. Hacker, M. P. De Lisio, J. C. Chiao, S. J. Li,

D. R. Gagnon, J. J. Rosenburg, and D. B. Rutledge, "A 100-element HBT grid amplifier," *IEEE Transactions on Microwave Theory and Techniques*, vol. 41, pp. 1762–1771, Oct. 1993. 11

[14] N. Sheth, T. Ivanov, A. Balasubramaniyan, and A. Mortazawi, "A nine HEMT spatial amplifier," *IEEE Transactions on Microwave Theory and Techniques*, pp. 1239–1242, June 1994. 11

[15] H. S. Tsai, E. A. Sovero, W. J. Wu, J. A. Higgins, and R. A. York, "37 GHz monolithic HBT quasi-optical amplifier array with multiple-slot antennas," *IEEE MTT-S International Microwave Symposium Digest*, June 1995. 11

[16] J. Hubert, J. Schoenberg, and Z. Popović, "High-power hybrid quasi-optical Ka-band amplifier design," *IEEE MTT-S International Microwave Symposium Digest*, pp. 585–588, May 1995. 11

[17] M. A. Forman, T. S. Marshall, and Z. Popović, "Two Ka-band quasi-optical amplifier arrays," *IEEE Transactions on Microwave Theory and Techniques*, June 1999. 11

[18] Thomas B. Mader, *Quasi-Optical Class-E Power Amplifiers*, Ph.D. thesis, Univ. of Colorado, Boulder, CO, 1995. 11

[19] Eric Bryerton, *High-Efficiency Class-E Amplifier Arrays*, Ph.D. thesis, Univ. of Colorado, Boulder, CO, 1999. 11

[20] Jon S. H. Schoenberg, *Quasi-Optical Constrained Lens Amplifiers*, Ph.D. thesis, Univ. of Colorado, Boulder, CO, 1995. 11

[21] Jon S. H. Schoenberg, Scott C. Bundy, and Zoya Popović, "Two-level power combining using a lens amplifier," *IEEE Transactions on Microwave Theory and Techniques*, vol. 42, no. 12, pp. 2480–2485, Dec. 1994. 11, 80

[22] H. S. Tsai, M. J. Rodwell, and R. A. York, "Planar amplifier array with improved bandwidth using folded-slots," *IEEE Microwave and Guided Wave Letters*, vol. 4, pp. 112–114, Apr. 1994. 11

[23] Milica Marković, *Quasi-Optical Modulators and Broadband High-Efficiency Amplifiers*, Ph.D. thesis, Univ. of Colorado, Boulder, CO, 1997. 11

[24] S. T. Chew and T. Itoh, "A 2×2 beam-switching active antenna array," *IEEE MTT-S International Microwave Symposium Digest*, pp. 925–928, June 1995. 11

[25] R. Flynt, L. Fan, J. Navarro, and K. Chang, "Low cost and compact active integrated antenna transceiver for system applications," *IEEE MTT-S International Microwave Symposium Digest*, pp. 953–956, Jun. 1995. 11

[26] R. Cahill, E. A. Parker, and C. Antonopoulos, "Design of multilayer frequency-selective surface for diplexing two closely spaced channels," *Microwave and Optical Technology Letters*, vol. 8, no. 6, pp. 293–296, April 20 1995. 11

[27] Stein Hollung, Wayne Shiroma, Milica Marković, and Zoya Popović, "A quasi-optical isolator," *IEEE Microwave and Guided Wave Letters*, vol. 6, no. 5, pp. 205–206, May 1996. 11

[28] M. J. Cryan, P. S. Hall, S. H. Tsang, and J. Sha, "Integrated active antenna with full duplex operation," *IEEE Transactions on Microwave Theory and Techniques*, vol. 45, no. 10, pp. 1742–1748, oct 1997. 11

[29] P. Lefleur, D. J. Roscoe, and M. Cuhaci, "A 20-GHz active integrated multilayer microstrip patch array for portable communication terminals," *IEEE Transactions on Antennas and Propagation*, vol. 2, pp. 1260–1263, July 1997. 11

[30] Wayne A. Shiroma, Eric W. Bryerton, Stein Hollung, and Zoya B. Popović, "A quasi-optical receiver with angle diversity," in *IEEE MTT-S International Microwave Symposium Digest*, San Francisco, CA, June 1996, pp. 1131–1134. 11, 80

[31] S. Ortiz, T. Ivanov, and A. Mortazawi, "A transmit-receive spatial amplifier array," *IEEE MTT-S International Microwave Symposium Digest*, vol. 2, pp. 679–682, Jun. 1997. 11, 81

[32] Stein Hollung, Amanda E. Cox, and Zoya Basta Popović, "A quasi-optical bi-directional lens amplifier," *IEEE Transactions on Microwave Theory and Techniques*, vol. 47, pp. 2352–2357, Dec. 1997. 11, 81, 106

[33] J. Vian and Z. Popović, "A transmit/receive active antenna with fast low-power optical switching," *IEEE Transactions on Microwave Theory and Techniques*, vol. 2, pp. 847–852, June 2000. 11, 81

[34] Zoya Popović and Amir Mortazawi, "Quasi-optical transmit/receive front ends," *IEEE Transactions on Microwave Theory and Techniques*, vol. 46, no. 11, pp. 1964–1975, Nov. 1998. 13, 81

[35] J. Hubert, L. Mirth, S. Ortiz, and A. Mortazawi, "A 4-watt Ka-band quasi-optical amplifier," *IEEE MTT-S International Microwave Symposium Digest*, June 1999. 14

[36] Lee Mirth and John Hubert, *Personal Communication*, Lockheed Martin, Electronics and Missiles, Orlando, Florida. 14

[37] C. M. Liu, E. A. Sovero, W. J. Ho, J. A. Higgins, M. P. De Lisio, and D. B. Rutledge, "Monolithic 40-GHz 670-mW HBT grid amplifier," *IEEE MTT-S International Microwave Symposium Digest*, pp. 1123–1126, June 1996. 14

[38] M. P. De Lisio, S. W. Duncan, D-W Tu, S. Weinreb, C-M Liu, and D. B. Rutledge, "A 44–60 GHz monolithic pHEMT grid amplifier," *IEEE MTT-S International Microwave Symposium Digest*, vol. 2, pp. 1127–1130, June 1996. 14

[39] E. A. Sovero, J. B. Hacker, J. A. Higgins, D. S. Deakin, and A. L. Sailer, "A Ka-band monolithic quasi-optic amplifier," *IEEE MTT-S International Microwave Symposium Digest*, pp. 1453–1456, June 1998. 15

[40] Mark Gouker, "Toward standard figures-of-merit for spatial and quasi-optical power-combined arrays," *IEEE Transactions on Microwave Theory and Techniques*, vol. 43, no. 7, pp. 1614–1617, July 1995. 15

[41] Constantine A. Balanis, *Antenna Theory: Analysis and Design*, chapter 1, Harper & Row, New York, 1982. 16, 19

[42] R. E. Collin, *Antennas and Radiowave Propagation*, chapter 1, McGraw-Hill, New York, 1985. 17

[43] Wayne A. Shiroma, *Cascaded Active and Passive Grids for Quasi-Optical Front Ends*, Ph.D. thesis, Univ. of Colorado, Boulder, CO, 1996. 20

[44] Todd Marshall, *Design and Characterization of Low-Cost Ka-Band Amplifier Antenna Arrays*, Ph.D. thesis, Univ. of Colorado, Boulder, CO, 2000. 24, 29, 30, 31, 66

[45] Lee Mirth and John Hubert, *Personal Communication*, Lockheed Martin, Electronics and Missiles, Orlando, Florida. 30, 31

[46] E. F. Kuester and D. C. Chang, *Theory of Waveguides and Transmission Lines*, pp. 193–194, Course Notes, Boulder, CO, 1998. 33, 93

[47] Paul Watson, *Personal Communication*, University of Colorado, Boulder, Colorado USA. 34

[48] University of Colorado, Boulder, CO USA, *WireZeus Linux version 24.Feb,1996.* 36

[49] Hewlitt Packard, USA, *Momentum.* 36

[50] Zeland Software Inc., 39120 Argonaut WY STE 499, Fremont, CA 94538 USA, *IE3D Version 7.01.* 36, 98

[51] AutoDesk, Inc., USA, *AutoCAD R14*. 48

[52] Maha A. Ali, Sean Ortiz, Toni Ivanov, and Amir Mortazawi, "Analysis and measurement of hard horn feeds for the excitation of quasi-optical amplifiers," *IEEE MTT-S International Microwave Symposium Digest*, pp. 1469–1472, June 1998. 67

[53] D. Kraus, *Radio Astronomy*, chapter 1, McGraw-Hill, 1966. 70

[54] Mark A. Gouker, "Spatial power combining," in *Active and Quasi-optical arrays for solid-state power combining*, Robert A. York and Zoya B. Popovic, Eds., chapter 2. John Wiley, New York, 1997. 70

[55] K. Yang, G. David, W. Wang, T. Marshall, M. Forman, L. W. Pearson, Z. Popović, L. P. B. Katehi, and J.F. Whitaker, "Electro-optic field mapping of quasi-optic power-combining arrays," *?*, p. ?, ? 1999. 76

[56] D. T. McGrath, "Planar three-dimensional constrained lenses," *IEEE Transactions on Antennas and Propagation*, vol. 34, no. 1, pp. 46–50, Jan. 1986. 80, 110

[57] Zoya Popović, *Personal Communication*, University of Colorado, Boulder, CO USA. 83

[58] Stein Hollung, *Quasi-Optical Transmit/Receive Lens Amplifier Arrays*, Ph.D. thesis, Univ. of Colorado, Boulder, CO, 1998. 84

[59] A. Vandelay, M. Von Nostrand, and K. Varnsen, "Signed-field analysis of surface mode losses," *IEEE Microwave and Guided Wave Letters*, 1989. 92

[60] D. M. Pozar, *Microwave Engineering*, chapter 12.3, p. 681, Addison-Wesley Publishing Comp., Inc., New York, 1990. 92

[61] R. E. Munson, "Conformal microstrip antennas and microstrip phased arrays," *IEEE Transactions on Antennas and Propagation*, vol. AP-22, pp. 74–78, Jan. 1974. 92

[62] Y. C. Shih and T. Itoh, "Analysis of conductor-backed coplanar waveguide," *Electronics Letters*, vol. 18, pp. 538–540, June 1982. 95

[63] Ching-Cheng Tien, Ching-Kuang C. Tzuang, S. T. Peng, and Chung-Chi Chang, "Transmission characteristics of finite-width conductor-backed coplanar waveguide," *IEEE Transactions on Microwave Theory and Techniques*, pp. 1616–1623, Sept. 1993. 96

[64] K. J. Herrick, T. Schwarz, and L. P. B. Katehi, "W-band micromachined finite ground coplanar (FGC) line circuit elements," *IEEE Transactions on Microwave Theory and Techniques*, vol. 1, pp. 269, 1997. 97

[65] Fred Brauchler, Steve Robertson, Jack East, and Linda P. B. Katehi, "W-band finite ground coplanar (FGC) line circuit elements," *IEEE Transactions on Microwave Theory and Techniques*, vol. 3, 1996. 97

[66] J. Papapolymerou, F. Brauchler, J. East, and L. P. B. Katehi, "W-band

finite ground coplanar monolithic multipliers," *IEEE Transactions on Microwave Theory and Techniques*, vol. 75, no. 5, pp. 614, 1999. 97

[67] Gildas P. Gauthier, Linda P. Katehi, and Gabriel M. Rebiez, "W-band finite ground coplanar waveguide (FGCPW) to microstrip line transition," *IEEE Transactions on Microwave Theory and Techniques*, vol. 1, pp. 107, 1998. 97, 99

[68] Jean-Pierre Raskin, Gildas Gauthier, Linda P. Katehi, and Gabriel M. Rebeiz, "W-band single-layer vertical transitions," *IEEE Transactions on Microwave Theory and Techniques*, vol. 48, no. 1, pp. 161–164, 2000. 98

[69] W. L. Stutzman and G. A. Thiele, *Antenna Theory and Design*, pp. 210–218, John Wiley & Sons, Inc., New York, NY, 1998. 99

[70] Gildas P. Gauthier, Jean-Pierre Raskin, Linda P. B. Katehi, and Gabriel M. Rebeiz, "A 94-GHz aperature-coupled micromachined microstrip antenna," *IEEE Transactions on Antennas and Propagation*, vol. 47, no. 12, Dec. 1999. 99

[71] M. Forman and Z. Popović, "A K-band ground-backed cpw balanced coupler and integrated antenna feed," *European Microwave Conference*, vol. 1, pp. 216–219, Oct. 2000. 103

[72] D. T. McGrath, "Planar three-dimensional constrained lenses," *IEEE Trans. Ant. and Prop.*, vol. 34, pp. 46–50, Jan. 1986. 109, 110

[73] D. T. McGrath, "Slot-coupled microstrip constrained lens," *Proceedings of the Antenna Applications Symposium*, Sept. 1987. 109

[74] D. T. McGrath, P. M. Proudfood, and M. A. Mehalic, "The microstrip constrained lens," *Microwave Journal*, pp. 24–37, Jan. 1995. 109

[75] H. Gent, "The bootlace aerial," *Royal RAdar Establishment Journal*, pp. 47–57, Oct. 1957. 109

[76] W. Rotman and R. Turner, "Wide angle microwave lens for line source applications," *IEEE Trans. Ant. and Prop.*, vol. AP-11, pp. 623–632, Nov. 1963. 110

[77] D. C. O'Shea, *Elements of modern optical design*, chapter 7, John Wiley & Sons, Inc., New York, 1985. 110

[78] The MathWorks, Inc., USA, *Matlab Version 5.3.0.14912a (R11)*. 110

Appendix A

Linguistic Analysis

The following data are derived from analyses of theses authored by past doctoral candidates in the group. While it is possible that these data may somehow be useful as a reference, it is intended for enjoyment only. As a student of languages in the presence of such a large quantity of raw material, analysis of the text proved impossible to resist.

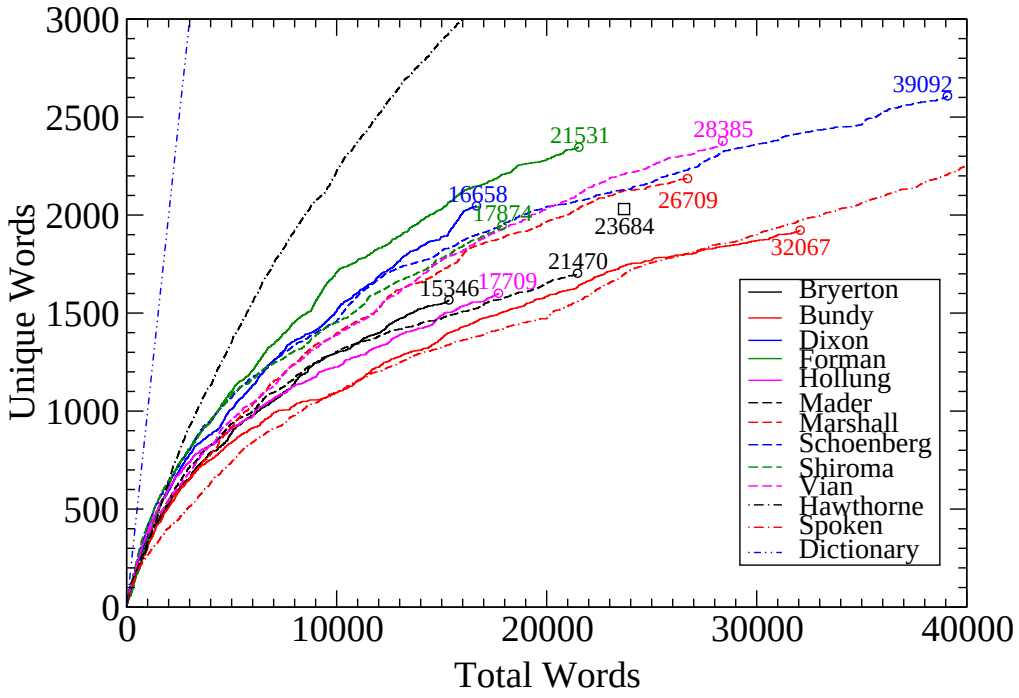

Figure A.1: Unique words as a function of total words for several theses written by members of the group over the past few years. The average thesis length is 23684 words. In addition to the theses, Nathaniel Hawthorne's *Scarlet Letter*, a transcription of a spoken conversation, and an English dictionary (/usr/dict/words) is included for comparison.

Table A.1: The frequency of letter appearance in a text normalized to the frequency of the letter "e". The first column is the letter order for the *Cambridge Encyclopedia* totaling 1.5 million words.

CE	Bryerton		Forman		Hollung		Marshall		Schoenberg		Vian	
e	e	1.000	e	1.000	e	1.000	e	1.000	e	1.000	e	1.000
a	i	0.701	a	0.707	a	0.674	t	0.750	t	0.785	t	0.755
t	t	0.700	t	0.681	t	0.645	a	0.717	a	0.740	i	0.607
i	a	0.650	i	0.623	i	0.625	i	0.643	i	0.727	a	0.607
n	s	0.547	n	0.573	n	0.523	n	0.552	n	0.622	n	0.556
o	o	0.541	r	0.521	r	0.512	r	0.534	r	0.576	s	0.556
r	n	0.538	o	0.484	s	0.502	o	0.505	o	0.536	o	0.535
s	r	0.508	s	0.482	o	0.457	s	0.503	s	0.522	r	0.481
l	h	0.365	l	0.310	l	0.322	h	0.355	l	0.376	h	0.368
h	c	0.343	h	0.300	d	0.309	l	0.319	h	0.349	l	0.304
d	l	0.310	c	0.285	h	0.280	c	0.301	d	0.342	c	0.288
c	d	0.305	d	0.280	c	0.254	d	0.294	c	0.323	d	0.286
m	f	0.271	m	0.223	f	0.207	m	0.223	p	0.275	f	0.206
u	m	0.239	u	0.211	m	0.205	u	0.214	f	0.247	m	0.201
f	u	0.231	f	0.208	u	0.195	f	0.209	m	0.225	p	0.187
p	p	0.228	p	0.203	p	0.183	p	0.200	u	0.220	u	0.186
g	w	0.146	g	0.136	g	0.122	b	0.134	g	0.160	g	0.139
b	g	0.140	b	0.121	b	0.102	g	0.126	w	0.120	w	0.118
y	b	0.112	y	0.110	w	0.100	y	0.106	b	0.111	b	0.093
w	v	0.094	w	0.098	y	0.093	w	0.100	y	0.108	y	0.086
v	y	0.092	v	0.088	v	0.087	v	0.074	v	0.076	v	0.078
k	k	0.027	k	0.025	z	0.022	z	0.022	q	0.027	k	0.020
x	q	0.024	z	0.020	q	0.022	k	0.020	z	0.017	x	0.015
j	z	0.022	x	0.018	x	0.015	x	0.020	x	0.015	q	0.014
z	x	0.017	q	0.014	k	0.012	q	0.019	k	0.014	z	0.014
q	j	0.004	j	0.004	j	0.001	j	0.003	j	0.002	j	0.008

Table A.2: The top-20 highest-occurring words in various theses.

Bryerton	Forman	Hollung	Marshall	Schoenberg	Vian
the	the	the	the	the	the
of	of	a	of	of	of
to	and	of	is	and	to
and	a	and	to	a	and
a	in	in	and	in	in
is	to	to	in	is	a
in	is	is	a	to	is
power	array	for	array	for	for
for	for	array	are	at	are
this	with	are	with	array	lens
at	are	as	by	amplifier	with
class	by	be	for	with	that
be	power	with	be	lens	as
efficiency	as	lens	power	are	optical
amplifier	on	feed	that	power	array
output	antenna	power	on	as	be
e	at	can	as	by	figure
are	an	optical	figure	an	by
with	unit	quasi	bias	be	on
as	active	at	which	element	switch

Table A.3: The top-20 highest-occurring technical words in various theses.

Bryerton	Forman	Hollung	Marshall	Schoenberg	Vian
power	array	array	array	array	lens
class	power	lens	power	amplifier	optical
efficiency	antenna	feed	bias	lens	array
amplifier	unit	power	antenna	power	switch
output	active	optical	field	element	power
element	bias	quasi	amplifier	noise	antenna
array	slot	amplifier	mmic	output	signal
frequency	gain	loss	output	input	unit
high	substrate	antenna	qo	gain	loss
combining	output	gain	substrate	ratio	microwave
measured	cell	measured	feed	frequency	signals
harmonic	measurements	design	design	feed	noise
maximum	line	element	gain	quasi	arrays
input	field	wave	slot	grid	system
amplifiers	band	output	horn	plane	pin
mode	feed	arrays	unit	db	spdt
feed	arrays	elements	antennas	optical	design
oscillator	antennas	transmit	cpw	antenna	adaptive
spatial	transmit	input	arrays	slot	bias
ghz	efficiency	high	rf	elements	diode

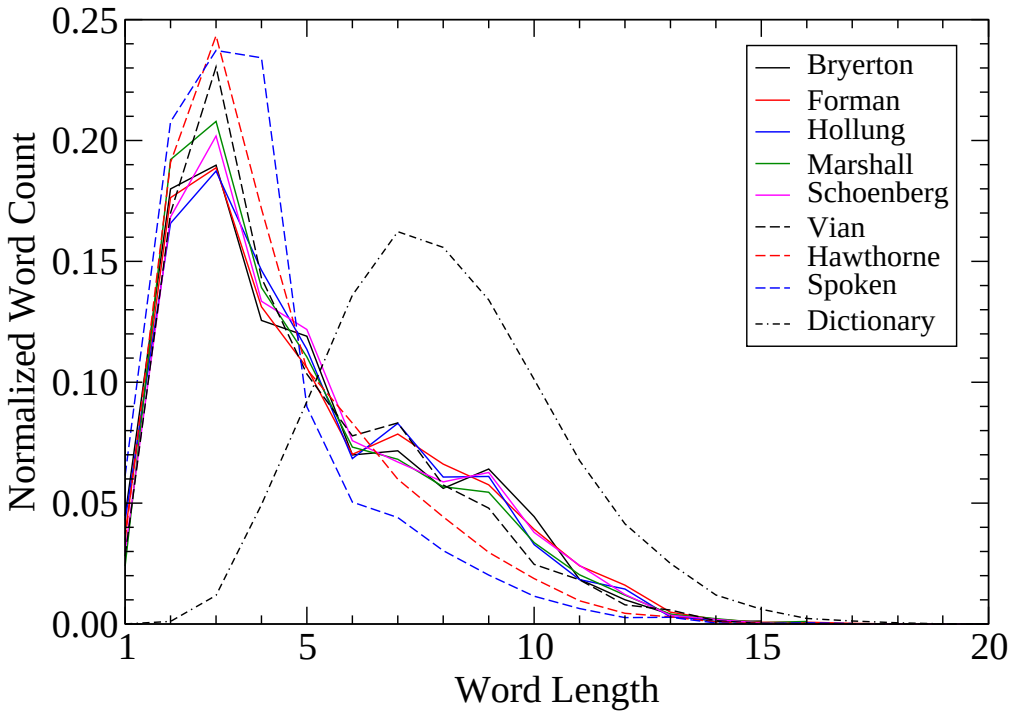

Figure A.2: Histogram of word lengths in a body of work normalized to the maximum number of words. Note the distribution of word lengths in an English dictionary.

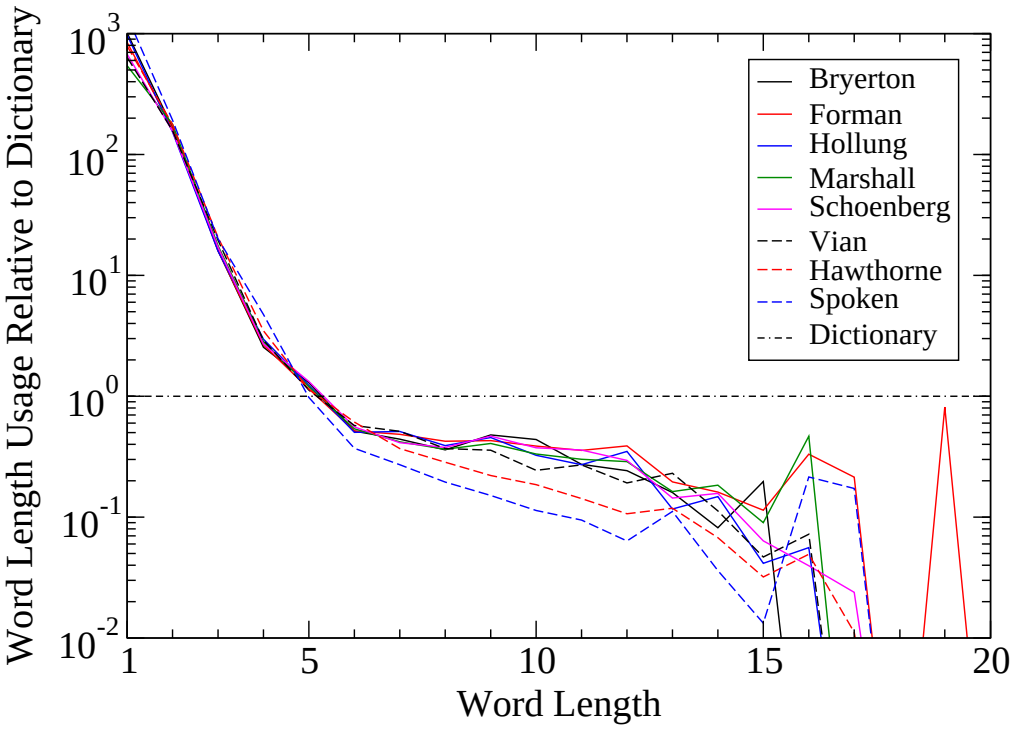

Figure A.3: Usage of word lengths relative to that length's appearance in the dictionary. This graph illustrates how words of shorter length are used at a greater frequency than their relative abundance in the dictionary.